



UNIVERSITAT
POLITÈCNICA
DE VALÈNCIA



ESCUELA TÉCNICA
SUPERIOR INGENIEROS
INDUSTRIALES VALENCIA

TRABAJO FIN DE MASTER EN INGENIERÍA BIOMÉDICA

**DESIGN AND DEVELOPMENT OF A
METHODOLOGY FOR THE CREATION OF
PERSONALIZED ANATOMICAL AND
ELECTROPHYSIOLOGICAL MODELS OF THE
HUMAN ATRIA AND TORSO**

AUTHOR: PABLO MARTINEZ ULLOA

SUPERVISOR: FRANCISCO JAVIER SAIZ RODRIGUEZ

SUPERVISOR: LAURA MARTINEZ MATEU

Academic year: 2018-19

RESUMEN

Las enfermedades cardiovasculares son la primera causa de muerte en el mundo en los países desarrollados. Entre ellas, las arritmias supraventriculares tales como la taquicardia o fibrilación auriculares son muy frecuentes, y contribuyen sustancialmente a la morbimortalidad cardiaca. Para entender con más detalle estas patologías sin tener que recurrir a métodos invasivos, las simulaciones computacionales electrofisiológicas de modelos cardiacos se han convertido en una importante herramienta en los últimos años. El desarrollo de modelos 3D cardiacos personalizados permite estudiar la actividad eléctrica cardiaca de manera específica para la optimización de la prevención, diagnóstico y tratamiento del paciente.

El objetivo principal de este trabajo es el diseño de una metodología para la creación de modelos 3D multi-escala de aurícula y torso humanos personalizados para cada paciente. Por tanto, se desarrollaron modelos de aurículas y de torso completo, y de solamente aurículas, y se realizaron simulaciones electrofisiológicas para estudiar sus diferentes comportamientos.

El primer paso fue la segmentación anatómica de las aurículas y los principales órganos del torso para obtener los modelos de superficie, a partir de imágenes de tomografía axial computarizada proporcionadas por el Hospital Politécnico y Universitario La Fe. Se efectuó un suavizado y acondicionamiento para los modelos de superficie, y se definió e implementó un grosor homogéneo en los modelos auriculares. Los órganos del torso segmentados, además de las aurículas, fueron: hígado, riñones, pulmones, huesos, vasos sanguíneos principales, superficie del torso (piel), y ventrículos. Debido a la alta heterogeneidad de las aurículas, un algoritmo se desarrolló para dividir de manera semiautomática las 45 regiones auriculares que poseen diferentes propiedades histológicas, funcionales o electrofisiológicas. A partir de los modelos de superficie, se generó una malla hexaédrica volumétrica de elementos finitos. Posteriormente, la dirección de fibras se definió basándose en estudios histológicos previos.

Finalmente, se realizaron diferentes simulaciones electrofisiológicas con los modelos obtenidos tanto en condiciones de ritmo sinusal, para validación, como de arritmias supraventriculares, con el objetivo de analizar los distintos patrones de propagación en patología cardíaca respecto de condiciones de control, así como la variabilidad entre pacientes. Para ambos, la validación en control y el análisis de los patrones arrítmicos, se utilizaron los mapas de propagación de potenciales de acción en las aurículas, y los electrocardiogramas (ECG) y mapas de potencial en la superficie del torso (BSPM).

Palabras Clave: Modelos personalizados, modelos computacionales, arritmias auriculares, imágenes médicas, tomografía computarizada, segmentación, modelo de torso, corazón humano, heterogeneidad electrofisiológica

RESUM

Les malalties cardiovasculars són la primera causa de mort en el món als països desenvolupats. Entre aquestes, les arítmies supraventriculars com per exemple la taquicàrdia o fibril·lació auriculars són molt freqüents, i contribueixen substancialment a la morbimortalidad cardíaca. Per tal d'entendre amb més detall aquestes patologies sense haver de recórrer a mètodes invasius, les simulacions computacionals electrofisiològiques de models cardíacs s'han convertit en una important eina en els últims anys. El desenvolupament de models 3D cardíacs personalitzats permet estudiar l'activitat elèctrica cardíaca de manera específica per a l'optimització de la prevenció, diagnòstic i tractament del pacient.

L'objectiu principal d'aquest treball és el disseny d'una metodologia per a la creació de models 3D multi-escala d'aurícula i tors humans personalitzats per a cada pacient. Per tant, van desenvolupar-se models d'aurícules i de tors complet, i de solament aurícules, i es van realitzar simulacions electrofisiològiques per tal d'estudiar els seus diferents comportaments.

El primer pas va ser la segmentació anatòmica de les aurícules i els principals òrgans del tors, per tal d'obtenir els models de superfície a partir d'imatges de tomografia axial computeritzada proporcionades per l'Hospital Politècnic i Universitari la Fe. Després va efectuar-se un suavitzat i condicionament dels models de superfície, i es va definir i implementar un grossor homogeni en els models auriculars. Els òrgans del tors segmentats, a més de les aurícules, van ser: fetge, renyons, pulmons, ossos, vasos sanguinis principals, superfície del tors (pell), i ventricles. A causa de l'alta heterogeneïtat de les aurícules, un algoritme va ser desenvolupat per a dividir de manera semiautomàtica les regions auriculars que posseïxen diferents propietats histològiques, funcionals o electrofisiològiques. A partir dels models de superfície, es generà una malla hexaèdrica volumètrica d'elements finits. Posteriorment, va definir-se la direcció de fibres basant-se en estudis histològics previs.

Finalment, es van realitzar diferents simulacions electrofisiològiques amb els models obtinguts tant en condicions de ritme sinusal, per a la validació, com de arrítmies supraventriculars, amb l'objectiu d'analitzar els distints patrons de propagació en patologia cardíaca respecte de condicions de control, així com la variabilitat entre pacients. Per a ambdós, la validació en control i l'anàlisi dels patrons arrítmics, es van emprar els mapes de propagació de potencials d'acció en les aurícules, i els electrocardiogrames (ECG) i mapes de potencial en la superfície del tors (BSPM).

Paraules clau: Models personalitzats, models computacionals, arítmies auriculars, imatges mèdiques, tomografia computeritzada, segmentació, model de tors, cor humà, heterogeneïtat electrofisiològica

ABSTRACT

Cardiovascular diseases are the leading cause of death in the world in developed countries. Among them, supraventricular arrhythmias such as atrial tachycardia or are frequent and contribute substantially to cardiac morbidity and mortality. To understand these pathologies in more detail without using invasive methods, the electrophysiological computational simulations of cardiac models have become an important tool in recent years. The development of personalized 3D cardiac models allows to study the cardiac electrical activity in a specific way for the optimization of the prevention, diagnosis and treatment of the patient.

The main objective of this work is the design of a methodology for the creation of 3D multi-scale models of human atrium and torso for each patient. Therefore, models of atria and complete torso, as well as only atrial models, were developed, and electrophysiological simulations were performed to study their different behaviors.

The first step was the anatomical segmentation of the atria and the main organs of the torso to obtain the surface models, from computerized axial tomography images provided by the Hospital Politécnico y Universitario La Fe. A smoothing and conditioning was done for the surface models, and a homogeneous thickness was defined and implemented in the auricular models. The organs of the segmented torso, in addition to the atria, were: liver, kidneys, lungs, bones, main blood vessels, surface of the torso (skin), and ventricles. Due to the high heterogeneity of the atria, an algorithm was developed to semi-automatically divide a total of 45 atrial regions that have different histological, functional or electrophysiological properties. From the surface models, a hexahedral finite element mesh was generated. Subsequently, fiber direction was defined based on previous histological studies.

Finally, different electrophysiological simulations were performed with the models obtained both in conditions of sinus rhythm, for validation, as well as supraventricular arrhythmias with the aim of analyzing the differences in the propagation patterns for cardiac pathology with respect to control conditions, and the variability among patients. For both, the validation in control and the analysis of the arrhythmic patterns, action potentials propagation maps in the atria, and electrocardiograms (ECG) and body surface potential maps (BSPM) on the torso were used.

Keywords: Personalized models, computational models, atrial arrhythmias, medical imaging, computerized tomography, segmentation, torso model, human heart, electrophysiological heterogeneity

DOCUMENTS INCLUDED IN THE TFM

- **Memory**
- **Budget**



UNIVERSITAT
POLITÈCNICA
DE VALÈNCIA



ESCUELA TÉCNICA
SUPERIOR INGENIEROS
INDUSTRIALES VALENCIA

MEMORY

INDEX

Chapter 1. Introduction.....	1
1.1. Atria and torso anatomy	1
1.1.1. Structure of the heart	1
1.1.2. Atrial anatomy.....	2
1.1.3. Torso anatomy	5
1.2. Electrophysiology of the atria and torso	6
1.2.1. Atrial electrophysiology	6
1.2.1.1. The heart conduction system.....	6
1.2.1.2. The action potential (AP)	7
1.2.2. Torso.....	9
1.3. Atrial pathologies	11
1.3.1. Atrial tachycardias.....	11
1.3.1.1. Focal atria tachycardia	11
1.3.2. Atrial Fibrillation (AF)	13
1.3.2.1. Chronic Atrial Fibrillation (cAF)	15
1.4. Computerized Tomography (CT)	16
1.5. Modelling the human Heart Electrical Activity	17
1.5.1. Atrial cellular models.....	18
1.5.2. 3D models.....	18
1.5.3. Numerical and computational methods for solving simulations	19
Chapter 2. Justification, motivation, and objectives.....	21
Chapter 3. Methodology	23
3.1. Acquisition of CT images	23
3.1.1. Patient overview	23
3.1.2. Characteristics of the CT images	24
3.2. Segmentation of the atria and torso from CT images.....	25
3.2.1. Segmentation of the atria	26
3.2.2. Segmentation of the torso	27
3.3. Conditioning of the surface models	29
3.3.1. Automatic and manual smoothing.....	29

3.3.2. Cutting off vessel extremities and opening of the valves in the atria models	30
3.3.3. Joining atria and adding thickness to the surface model.....	31
3.4. Division of the atria surface models in different anatomical regions.....	32
3.4.1. Labelling RA-LA.....	33
3.4.2. Semi-automatic region division algorithm	33
3.4.3. Final modifications	35
3.5. Meshing of the atria and torso models.....	36
3.5.1. Meshing the atria	36
3.5.2 Meshing the torso	37
3.6. Preparation of the volume model for simulations.....	38
3.6.1. Mapping RA-LA and ORGANID properties into the volume model.....	38
3.6.2. BB regions separation and insulating.....	38
3.6.3. Material, ionic model and fiber orientation.....	40
3.7. Electrophysiological simulations	41
3.7.1. Ionic models	41
3.7.2. Atrial simulations.....	44
3.7.2.1. Generation of Elvira files	44
3.7.2.2. Simulation process	44
3.7.3. Torso simulations	46
3.8. Summary of the methods.....	47
Chapter 4. Results	49
4.1. Surface Geometries.....	49
4.1.1. RA-LA and ORGANID labelled surface models	49
4.1.2. Torso model	50
4.2. Volume Geometries	51
4.2.1. Atrial models	51
4.2.1.1. Mesh quality analysis	51
4.2.1.2. Final atrial volume models	54
4.2.2. Torso model	60
4.2.2.1. Mesh quality.....	60
4.2.2.2. Torso volume model	61
4.3. Control Simulations	62

4.3.1. Atrial simulations.....	62
4.3.2. Torso simulations	65
4.4. Arrhythmia simulations	66
4.4.1. Atrial simulations.....	66
4.3.2. Torso simulations	70
Chapter 5. Discussion	73
5.1. Creation of personalized atria and torso models.....	73
5.2. Electrophysiological simulations	75
5.3. Limitations.....	75
Chapter 6. Conclusion	77
Chapter 7. Future work	79
Chapter 8. Anexs	81
8.1 Matlab codes.....	81
Chapter 9. References.....	103

FIGURE INDEX

Figure 1. Anatomy of the heart and blood flux throughout the cardiac valves and cavities	1
Figure 2. Anatomical atrial regions and principal fiber direction.....	3
Figure 3. Position of the atria with respect to the other torso structures in the transverse plane.	5
Figure 4. Coronal view of the interior of the human torso showing the main organs	5
Figure 5. Heart's electrical conduction system, showing the APs of the different cardiac cells ..	7
Figure 6. Ionic exchange through the cell membrane of cardiomyocytes.....	7
Figure 7. Phases of the cardiac AP and types of channels involved	8
Figure 8. Heterogenous APs based on the type of atrial cell	9
Figure 9. Position of the 12 leads and typical ECG signal for each (left). Representation of the standard and augmented leads (right).....	10
Figure 10. Anterior view of a BSMP corresponding to a patient during VF.	11
Figure 11. FAT (top) at 100 bpm and sinus rhythm (bottom) ECG signals for lead II in a single patient.....	12
Figure 12. Representation of macroreentrant atrial tachycardia of the right atrium seen in clinical practice]	13
Figure 13. Signals of a patient with a right MRAT with a tachycardia cycle length of 420 ms. ..	13
Figure 14. A: Transmission of the electrical impulses in AF [1]. B: ECG in control conditions (top), and AF (bottom) [67].....	14
Figure 15. APs in control and cAF remodeling, recorded at a stimulation frequency of 0.5 Hz by Bosch et al.	16
Figure 16. Representation of the cardiac multiscale modelling.	17
Figure 17. APs of the main five ionic atria models	18
Figure 18. Pipeline of the methodology applied in this work	23
Figure 19. Seg3D interface, showing the CT scan of patient 3023001.....	26
Figure 20. Segmentation seeds for the 5 principal heart structures for patient 3023001	27
Figure 21. Coronal view of the CT scan for patient 1403865 with the brightness and contrast adjusted for visualizing the bones.....	28
Figure 22. Segmented regions of the main organs of the torso for patient 1403865 in coronal view.	28

Figure 23. Surfaces before (left column) and after (right column) smoothing (1000 iteration) performed in Paraview: right atrium (top) and left atrium (bottom) geometries from patient 3196630.....	29
Figure 24. Blender interface in Sculpt mode showing the available brush tools.....	30
Figure 25. Orifices made in Paraview for patient 3196630 models.....	30
Figure 26. Removal of extra edges in the valves in Blender.	31
Figure 27. Removal of faces where the FO is established (left) and union of both atria by the FO for patient 3023001 model.	31
Figure 28. 3 atria layers (epicardium and 2 endocardium) for patient 3196630 before closing the surface model.....	32
Figure 29. Process of joining epicardium and endocardium.....	32
Figure 30. Definition of regions surrounding an orifice	34
Figure 31. Second mechanism of atrial region division for RPV, UVC, and RAA for model 3014094	35
Figure 32. Process of deletion of PM in the epicardium for model 3014094.	35
Figure 33. Remeshed surface models of the torso and atria given as input for the volumetric meshing of the torso model.....	37
Figure 34. BB before (left) in the surface model and after (middle and right) BB region separation in the volume model for patient 3023001.	39
Figure 35. Insulation of the cells that should have not been connecting the CS and the LWLA for model 3023001.	39
Figure 36. Insulation of the cells that should have not been connecting the walls of LA and RA for model 3023001.....	39
Figure 37. Method for fiber direction calculation.....	41
Figure 38. Fiber direction definition for model 1403865 for the left inferior PV (LIPV) (top), RAA (middle), and BB (bottom).	41
Figure 39. Schematic representation of the CRN ionic model	42
Figure 40. Action potential (AP) plots for each atrial region of the CRN control model	43
Figure 41. APs for the remodeled ionic models for each atrial region.	44
Figure 42. Protocol of stimulation S1-S2. Regions defined for model 1403865.	46
Figure 43. Pipeline of the methodology applied in this work including the software used at each step (green)	48
Figure 44. Surface meshes divided into RA (blue) and LA (red).....	50
Figure 45. Surface meshes divided in the 45 ORGANID regions.....	50

Figure 46. Smoothened surfaces of the organs in the torso model segmented from patient with ID 1403865	51
Figure 47. Histogram of the mesh size for the 4 volumetric atrial meshes (x axis: size of the element; y axis: number of elements).	53
Figure 48. Analysis of the Scaled Jacobian of the atrial volumetric meshes.....	53
Figure 49. Ionic model property in the 3D atrial models	54
Figure 50. Material property for the 3D atrial models.....	55
Figure 51. Fiber direction in the 3D atrial models.....	56
Figure 52. Histogram of the element size for the volumetric torso model	61
Figure 53. Analysis of the Scaled Jacobian of the torso volume model.	61
Figure 54. Final torso volume model.....	62
Figure 55. Activation sequence for the atrial model from patient 1403865.	63
Figure 56. Activation sequence for the atrial model from patient 3014094.	63
Figure 57. Activation sequence for the atrial model from patient 3023001.	64
Figure 58. Activation sequence for the atrial model from patient 3196630.	64
Figure 59. Location of the 12 leads in our torso model, showing the ECG signals obtained at each lead for the control simulation of patient 1403865.....	65
Figure 60. BSPM for the control simulation of patient 1403865 at different time instants in the front (top) and back (bottom) coronal view	66
Figure 61. Activation sequence showing the induced the induced macroreentrant activity for model with patient ID 1403865	67
Figure 62. Activation sequence showing the induced the induced macroreentrant activity for model with patient ID 3014094	68
Figure 63. Activation sequence showing the induced the induced macroreentrant activity for model with patient ID 3023001	68
Figure 64. Activation sequence showing the induced the induced macroreentrant activity for model with patient ID 3196630	68
Figure 65. Potential extracted at node 634057 where the ectopic focus is applied in the PV during the simulation with the S2 protocol for simulation with 6 ectopic foci given at a BCL of 130 for model with patient ID 1403865.	69
Figure 66. Potential extracted at node 764405 where the ectopic focus is applied in the PV during the simulation with the S2 protocol for simulation with 6 ectopic foci given at a BCL of 130 for model with patient ID 3014094.	69
Figure 67. Potential extracted at node 630342 where the ectopic focus is applied in the PV during the simulation with the S2 protocol for simulation with 6 ectopic foci given at a BCL of 130 for model with patient ID 3023001.	70

Figure 68. Potential extracted at node 1466884 where the ectopic focus is applied in the PV during the simulation with the S2 protocol for simulation with 6 ectopic foci given at a BCL of 130 for model with patient ID 3196630..... 70

Figure 69. ECG signals of the 6 precordial leads during the macroreentry simulation for patient 1403865..... 71

Figure 70. BSPM for the macroreentry simulation for patient 1403865 at different time instants in the front (top) and back (bottom) coronal view 72

TABLE INDEX

Table 1. Dimensions of the principal anatomical structures in the heart.....	4
Table 2. Anatomical dimensions of the organs inside the thoracic cage.....	6
Table 3. Experimental variation of the ionic currents involved in the cAF electrical remodeling.	15
Table 4. Dimensions of RA, LA, and the PV structures for the 4 case studies presented	24
Table 5. Main characteristics of the CT scans for each of the case studies	25
Table 6. Relative conductances with respect to the g_{max} in the original CRN model for the different anatomical regions.....	43
Table 7. Remodeling coefficients applied to the modified CRN models for each region.	43
Table 8. Conductivity and anisotropy values for the electrophysiological simulations performed in control for each atrial region.	45
Table 9. Model and experimental tissue conductivities for the torso model.....	47
Table 10. Nº of cells and points for each of the surface atrial meshes.....	49
Table 11. Nº of cells (hexahedral elements) and points (nodes) for the volumetric meshes of the 4 atria segmented.	52
Table 12. Meshing statistics provided by MeshGems for the 4 atrial volumetric meshes	52
Table 13. Detailed fiber direction for each anatomical region for the model with patient ID 3014094, compared to the fiber orientation presented by Ferrer.....	60

Acronyms

3D	3 dimension
AF	Atrial fibrillation
AP	Action potential
APD	Action potential duration
AVN	Atrioventricular node
AVR	Atrioventricular ring
BB	Bachmann's bundle
BCL	Basic cycle length
Bpm	Beats per minute
BSPM	Body surface potential map
CS	Coronary sinus
CSc	Coronary sinus connections
CT	Computed tomography
CTS	Crista terminalis
ECG	Electrocardiogram
FAT	Focal atrial tachycardia
FO	Fossa Ovalis
IB	Intercaval bundle
ICV	Inferior cava vein
IST	Isthmus
LA	Left atrium
LAA	Left atrial appendix
LAS	Left atrial septum
LFO	Limb of Fossa Ovalis
LIPV	Left inferior pulmonary vein
LPV	Left pulmonary veins
LPW	Left posterior wall
LSPV	Left superior pulmonary vein
LSW	Left superior wall
MRAT	Macroreentrant atrial tachycardia
MV	Mitral valve
PM	Pectinate muscles
PV	Pulmonary veins
RA	Right Atrium
RAA	Right atrial appendix
RAS	Right atrial septum
RIPV	Right inferior pulmonary vein
RLW	Right lateral wall
RPV	Right pulmonary veins
RSPV	Right superior pulmonary vein
SAN	Sinoatrial node
SCV	Superior cava vein
TV	Tricuspid valve

CHAPTER 1. INTRODUCTION

1.1. ATRIA AND TORSO ANATOMY

1.1.1. Structure of the heart

The heart is the central and fundamental organ of the cardiovascular system. Its main function is to pump blood through the whole body to provide the organism with oxygen and the nutrients needed. It is formed primarily of muscular tissue called myocardium, and of connective tissue. The wall of the heart is composed of three layers: epicardium, myocardium, and endocardium. Epicardium is the most external layer, myocardium the intermediate, and endocardium the inner structure. The myocardium is made up of muscular tissue and is in charge of contracting in a potent and rhythmic manner performing the pumping function. The heart consists of 4 chambers: left atrium (LA), right atrium (RA), left ventricle (LV), and right ventricle (RV). The atria and ventricles are connected by the atrioventricular valves: the mitral valve (MV) connects the LA to the LV, and the tricuspid valve (TV) connects the RA to the RV. The left and right sides of the heart are separated by the interatrial septum in the atrial region, and by the interventricular septum in the ventricular region. There are other two valves that have the responsibility of controlling the departure of blood from the heart: the pulmonary valve, located at the exit of the RV, pumps deoxygenated blood to the lungs, and the aortic valve, located at the exit of the LV, pumps oxygenated blood through the aorta to the rest of the body. The heart can be considered two independent pulsatile pumps: the left heart in charge of the pulmonary circulation, collecting deoxygenated blood and pumping it to the lungs, and the right heart in charge of the systematic circulation, collecting oxygenated blood and spreading it along the body. The circulatory blood flux along the main cardiac structures can be observed in detail in Figure 1. [1], [2]

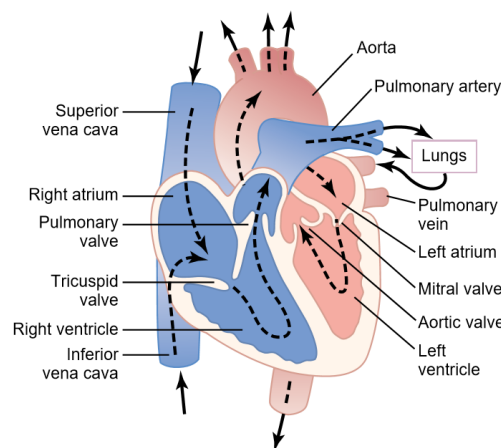


Figure 1. Anatomy of the heart and blood flux throughout the cardiac valves and cavities [1]

In the torso, the heart is located inside the thoracic cavity, behind the sternum and in between the lungs. It is coated by a sac called the pericardium that protects the heart against friction and external damage. [1], [2]

1.1.2. Atrial anatomy

The atria are two cavities located in the upper side of the heart, above the two ventricle chambers. They have an irregularly rounded shape, more globular in the right atrium and more ovoid in the left atrium. Both atria consist of the same basic anatomical structures: the atrial body, an appendage, a venous component, and the atrioventricular valve, along with the septum and adjacent walls between the cavities [3], [4]. Atria and ventricles are separated by the interatrial wall, which consists of a connective tissue that isolates the chambers allowing electrical connection only along the tricuspid and mitral valves.

In Figure 2, we can differentiate the different atrial anatomical regions and their fiber direction. There is a total of 23 regions: 11 in the right atrium (RA), 8 in the left atrium (LA), and 4 connecting both atria. The regions located in the RA are: sinoatrial node (SAN), crista terminalis (CTS), right atrial septum (RAS), intercaval bundle (IB), isthmus (IST), right atrial appendix (RAA), right lateral wall (RLW), pectinate muscle (PM), superior cava vein (SCV), inferior cava vein (ICV), and tricuspid valve (TV). In the left atrium we can find: left atrial septum (LAS), mitral valve (MV), left posterior wall (LPW), left superior wall (LSW), coronary sinus (CS), left atrial appendix (LAA), and the right and left pulmonary veins (RPV and LPV). The structures responsible of joining both atria are the Bachmann's Bundle (BB), splitting into right and left Bachmann's Bundle (RBB and LBB), the fossa ovalis (FO) and the limbus of the fossa ovalis (LFO). [3], [4], [5]

The SAN is the natural pacemaker of the heart containing autorhythmic cells. Following a path down the SAN along the IB is the CTS, which is an important muscle that separates the PM from the smooth walls of the venous area in the inner surface. The PM expand perpendicularly from the CTS in direction to the MV and RAA, creating a complex network of highly conductive muscles. The RAA is characteristic due to its big and triangular shape. The SCV and ICV are venous regions that load the blood into the RA. The CS channels the cardiac venous blood into the RA and attaches to the LA through muscular connections. The LAA is smaller and usually has a tubular shape. It connects in its posterior area with the RPV and LPV, receiving oxygenated blood from the lungs. [3], [4]

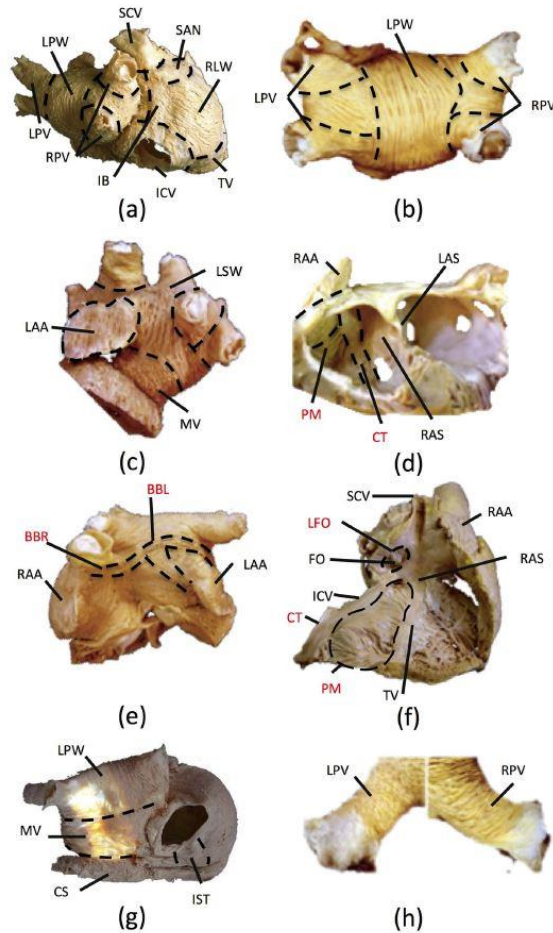


Figure 2. Anatomical atrial regions and principal fiber direction. [5], [6]

The thickness of the auricular walls is lower than of the ventricular walls, as the atria pump blood to the ventricles, while the ventricles pump blood out of the heart to the rest of the body. Several studies have reported that the human atrial wall has a thickness between 1 and 3 mm [7]–[9]. In the RA, the PM and CTS make the atrial wall thicker breaking uniformity. Regarding the LA, the wall is thinner in the posterior and inferior areas compared to the superior regions. Some studies support that the wall of the LA is greater than of the RA [10], while others support the opposite [3].

In Table 1, we can observe the dimensions of the principal regions and anatomical structures. This data was previously collected in two thesis carried out within our research group [11][12]. As observed, there exist a high variability in the anatomy and size of different individuals, making every atria particular and unique.

RA			LA		
Region	Size (cm)	Reference	Region	Size (cm)	Reference
SAN	0.60 x 0.40	[13]	LAA	5.70	[14]
Wall CTS	0.70-1.60	[15]	Wall width	0.20	[3]
	0.30-0.60	[16]		0.30-0.50	[17]
				0.05-0.35	[18]
Length CTS	5.10-6.00	[19]	Diameter PV	0.70-1.60	[15]
Wall width	0.05-0.35	[17]	External diameter MV	2.00-3.80	[15]
	0.80-0.12	[20]		2.60-3.20	[21]
				2.50-3.30	[17]
Between anterior and posterior wall	2.80-5.20	[15]	Length PV	0.80-1.50	[22]
Between septum and lateral wall	2.90-5.30	[15]	Interatrial unions		
Between lower and upper faces	3.60-4.20	[23]	Region	Size (cm)	Reference
Diameter CS	0.95-1.10	[15]	FO	0.18-4.40	[25]
	0.60-0.75	[24]		cm^2	
External diameter TV	2.00-4.00	[15]	BB	0.40	[26]
	3.20-3.70	[21]		0.90	
	3.20-4.00	[17]		1.10	

Table 1. Dimensions of the principal anatomical structures in the heart

Regarding the position of the atria on the torso, the RA is adjacent to the right lung on the anterolateral edge, with the aortic trunk on the anteromedial face, and with the LA on the left posterior side. The LA forms the left posterior side and the lower part of the heart and is surrounded by the left bronchial tube and the trunk of the pulmonary arteries, and the esophagus on the posterior side. [3], [4] In Figure 3, the position of the RA and LA with respect to other organs in the torso can be observed. [27]

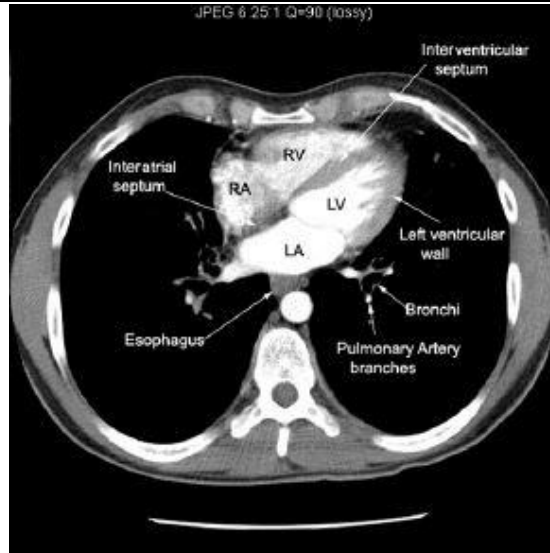


Figure 3. Position of the atria with respect to the other torso structures in the transverse plane. [27]

1.1.3. Torso anatomy

All the vital organs apart from the brain are located in the human torso. The rib cage is a semi-rigid structure in charge of facilitating the breathing movements and protecting the thoracic viscera. It is longitudinally restricted by the sternum on the upper and anterior faces, by the backbone on his posterior side, and transversally by twelve pair of ribs that surround the torso. The vertebral column holds the body occupying the longitudinal axis of the whole skeleton, while the ribs and viscera are suspended on its ventral face. [28] The heart is placed in the center of the thoracic cavity, as it can be observed in Figure 4, where 2 representations of the main structures on the human torso are shown. [29], [30]

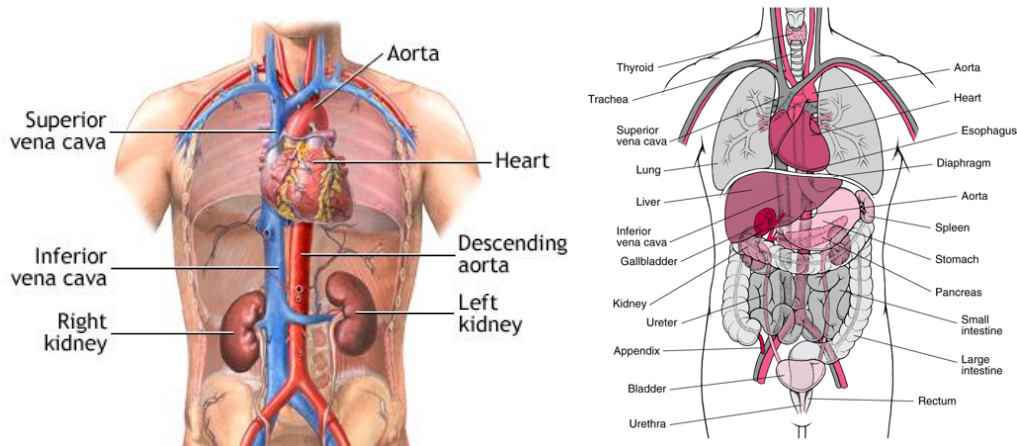


Figure 4. Coronal view of the interior of the human torso showing the main organs [29], [30]

In Table 2, the anatomical dimensions of the thoracic cage and the organs located inside it are shown. This data has been previously collected in a doctoral thesis developed in our research group [28]. As observed, there are wide ranges of values for the dimensions of the different regions and organs in the torso, existing a high variability between patients.

Region	Size (cm)	Reference
Abdomen circumference	7070-110.40	[31]
Average torso breadth	26.35-28.61	[32]
Average torso depth	13.27-16.27	
Diaphragm height	20.46-26.12	
Liver diameter	9.40-21.30	[33]
Lung height	25.00	[34]
Lung's bases transverse diameter	10.00 (right) – 7.00 (left)	
Lungs posteroanterior diameter	16.00	
Shoulder breadth	39.90 – 50.50	[31]
Shoulder depth	17.70 – 25.30	
Spine length	56.94	[35]
Sternum angle	158.97 – 173.73	[36]
Sternum length	29.36 – 36.54	
Rib angle	49.15 – 62.75	[32]
Waist depth	17.70 – 26.90	[31]

Table 2. Anatomical dimensions of the organs inside the thoracic cage

1.2. ELECTROPHYSIOLOGY OF THE ATRIA AND TORSO

1.2.1. Atrial electrophysiology

1.2.1.1. The heart conduction system

Since the heart starts its own beat, it can be considered an autonomous organ. There are different regions that contain autorhythmic cells able to act as a pacemaker and induce excitation, which are the SAN in the RA, the atrioventricular node (AVN) between the atria and ventricles, and the Purkinje fibers, in the ventricles. [1] The most important one is the SAN, which is the natural pacemaker of the heart in normal conditions, due to the short period of spontaneous electrical activity initiation of its myocytes. The SAN controls the heart rate (HR), which in physiological conditions is approximately 70-80 beats per minute (bpm). APs are generated in the SAN, and electrical activity propagates from one myocyte to the next one, activating the atrial tissue and spreading a waveform throughout the atria. First, the AP pulses propagate in the RA, and then pass into the LA, through the preferential conduction bundles, BB, LFO, and the CSc. Then, the electrical activity is extended towards the ventricles along the AVN. In physiological conditions, AVN cells do not excite spontaneously due to its slower excitation rate (40-60 bpm) and are activated by the propagation coming from the atria initiated by the SAN. In pathological conditions where the propagation from the atria does not reach the AVN or is extremely slow, the AVN autorhythmic cells excite and behave as the pacemaker to propagate the electrical activity towards the ventricles. [2], [37]

In Figure 5, APs corresponding to the specialized pacemaker and conduction cells are shown, representing the heart's electrical conduction system. The shape and duration of the APs can be compared for the different type of cardiac cells. The superposition of these signals measured at the body surface results in an electrocardiogram (ECG), which can be observed in the lower part of Figure 5 for normal conditions. [38]

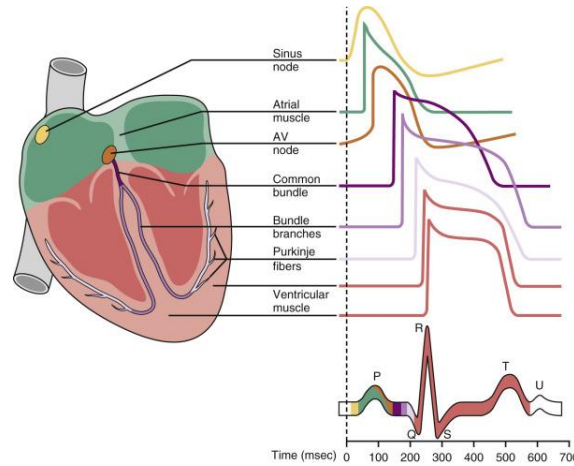


Figure 5. Heart's electrical conduction system, showing the APs of the different cardiac cells [38]

1.2.1.2. The action potential (AP)

The cardiac cells responsible of exciting and propagating electrical activity are the myocytes. Their morphology is cylindrical, with a diameter between 10-20 μm and a length around 50-150 μm [37]. When a stimulus is intense enough, cells are forced to depolarize leaving their resting state. The cell membrane, which is semipermeable, separates the intracellular and extracellular spaces and permits the exchange of ions changing the gradients in concentrations and potential between both spaces. It is made up of a lipid bilayer and proteins that build the pumps, ion channels, and exchangers present in the membrane, and that allow the movement of ions creating an ionic flux. In Figure 6, the protein channels in the membrane in charge of ion exchange are shown. Ion channels can be classified depending on the type of stimulus they respond to, as follows: voltage-gated channels, ligand-gated channels, and mechanically-gated channels. [1]

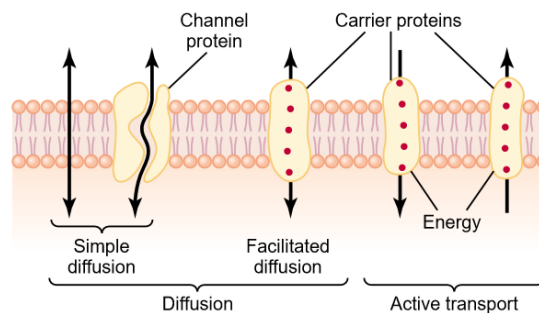


Figure 6. Ionic exchange through the cell membrane of cardiomyocytes. [1]

The difference between the ionic concentration at the two sides of the lipid bilayer yields an electrical potential called transmembrane potential (V_m). [1], [39]. In the so-called dynamic equilibrium, the potential in the intracellular space is lower than in the extracellular space, so the resting transmembrane potential is -80 mV [40]. V_m is described by Equation 1, which is the following:

$$V_m = \phi_i - \phi_e \quad (1)$$

If a stimulus raises this potential above a certain threshold potential, approximately around -60 mV, the cell depolarizes raising the V_m to a value close to zero generating an AP. If the stimulus does not reach the threshold, the V_m returns to its resting value. [37]

An atrial AP consists of 5 phases, characterized by different ion movements, as shown in Figure 7. The different phases are presented in detail below. [1], [39], [41]

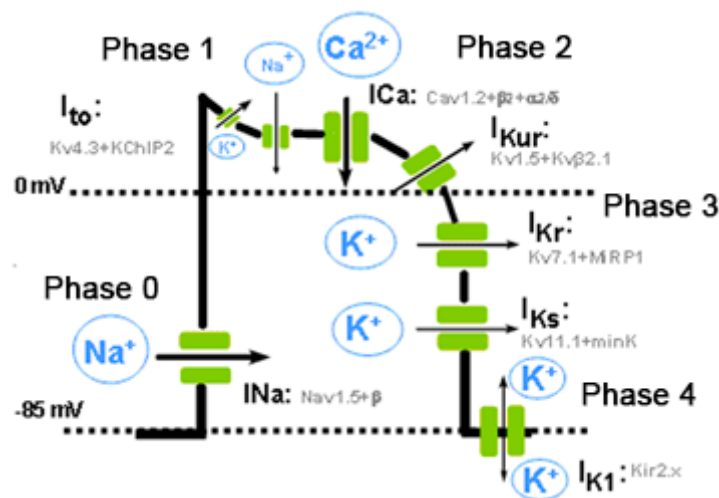


Figure 7. Phases of the cardiac AP and types of channels involved [42]

- Phase 0. Depolarization: It is caused by the voltage-gated channels that induce a massive influx of Na^+ generating the fast-inward Na^+ current (I_{Na}). Depolarization of the cardiac cells is produced when these channels rapidly activate permitting the movement of Na^+ across the membrane into the cell for 1 to 2 ms, then the Na^+ channels immediately close going back into an inactive state.
- Phase 1. Initial fast repolarization: Due to the inactivation of Na^+ channels and the appearance of the movement of K^+ outwards the cell caused by the activation of transient outward K^+ currents (I_{to}).
- Phase 2. Plateau: It is produced by the balance between the inward Ca^{2+} current and a small portion of Na^+ channels that remain active and the outward rapid and slowed delayed rectifier currents (I_{Kr} and I_{Ks}). This equilibrium is maintained due to the slower activation of Ca^{2+} channels. This phase is characteristic of the cardiac muscle that allows a longer contraction of the myocytes compared to other types of muscle cells.
- Phase 3. Repolarization. The inactivation of I_{Na} and I_{Ca} accelerates the repolarization. In addition, there is a dominance of the inward rectifier K^+ current (I_{K1}) that brings the potential back to the resting conditions.

- Phase 4. Resting potential. Dynamic equilibrium is restored and the cell remains at its resting potential, polarized due to the activity of the NaK pump and the IK1 channels, which are slightly activated.

There exists a time interval during the AP when a new stimulus cannot excite the cell, which is called refractory period. During the absolute refractory period is not possible for the cell to respond to a stimulus. However, during the relative refractory period a stimulus of adequate amplitude duration could cause the opening of the Na⁺ channels and induce a new AP. In the atria, the refractory period is approximately 0.15 s [1].

As seen in Figure 5, AP shape and duration varies depending of the type of cell in the conduction system of the heart. The same occurs for the different regions of the atria. There exist an atrial heterogeneity with the APs of the cells differing among regions. In Figure 8, we can observe the APs for different atrial wild type cells [43].

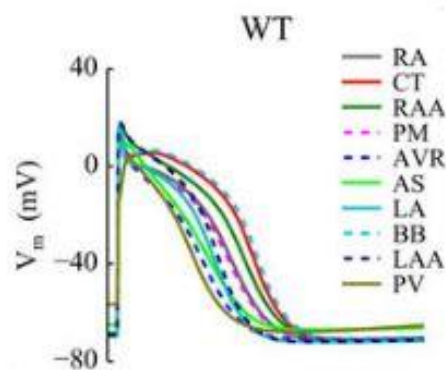


Figure 8. Heterogenous APs based on the type of atrial cell [43]

1.2.2. Torso

The heart's electrical activity propagates throughout the body and can be measured in a simple manner from the body surface. This resulting external signal is called electrocardiogram (ECG) and can be used for diagnosis of the electrical activity of the heart. The ECG is a superposition of all the APs generated in the cardiac muscle distorted by the rest of body structures. Information about the position of the heart, about the cardiac rhythm and its origin, and about the propagation of the electrical impulse can be deduced from this signal.

The phases of the ECG are in accordance with the activation instants of the different cardiac regions, as observed in Figure 5. The depolarization of the cells in the SAN and its propagation throughout the atria causes the P-wave, and subsequently the depolarization of the ventricular cells induces the appearance of the QRS complex in the ECG. Lastly, the T-wave appears as a consequence of the ventricular repolarization, while atrial repolarization is masked by the QRS complex and cannot be observed in the ECG. The U-wave appears rarely, and it is caused by the late activation of some regions of the ventricular myocardium. [1], [39],[42]

There are two types of ECG recordings: unipolar and bipolar. A unipolar ECG uses one active electrode and a reference one, while bipolar uses two active electrodes. A positive potential is obtained by an active electrode when depolarization is directed towards it. When depolarization goes in the opposite direction a negative potential is achieved. [1], [39]

Nowadays, the standard ECG is composed of 12 leads: 3 standard limb leads, 3 augmented limb leads and six precordial leads (see Figure 9). In the left image of Figure 9 [39], the position of the 12 leads and an example of the signal achieved in each of them in physiological conditions are shown.

The 3 standard limb leads are bipolar and were first used by Einthoven at the beginning of the 20th century [44]. They are located at the right and left arms, and left leg forming a triangle as shown in the right image of Figure 9 [39], they record differences in potential between two limbs, and they give information about the electrical activity of the heart in the frontal plane. Lead 1 is calculated as the difference in the potential recorded between the right arm and the left arm, lead 2 between the right arm and the left leg, and lead 3 between the left arm and the left leg. At any given instant the sum of the potentials in lead 1 and 3 equals the potential in lead 2, as Einthoven's law states [1], [39].

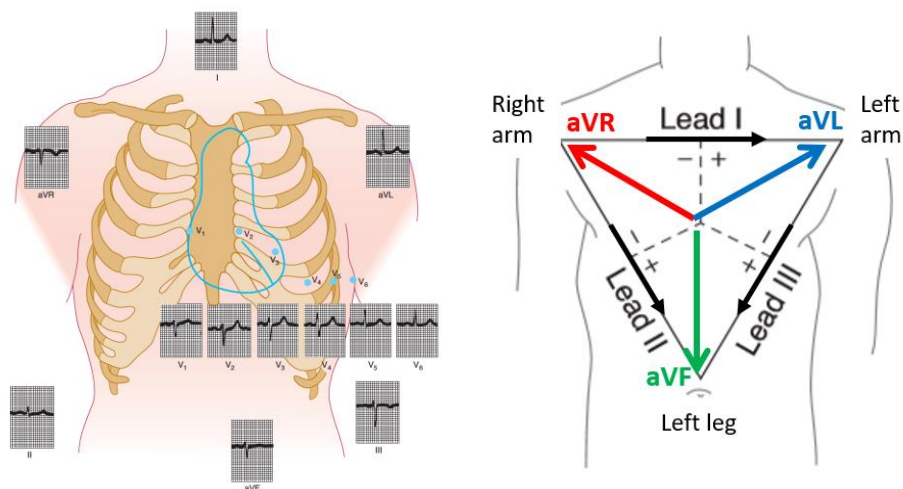


Figure 9. Position of the 12 leads and typical ECG signal for each (left). Representation of the standard and augmented leads (right). Modified from [39]

There are also 3 augmented limb leads, but in this case they are unipolar and record the potential between one limb and the combination of the other two. The active electrodes are located in the right arm (aVR), left arm (aVL) and left leg (aVF), as shown in the left image of Figure 9. Similarly to the standard leads, they record the electrical activity of the heart in the frontal plane, but they produce signals of higher amplitudes [1], [39].

For obtaining information about the activity of the heart in the transverse plane, the six unipolar precordial leads are used. A higher spatial resolution is achieved due to the proximity of the electrodes to the heart, with each electrode recording the activity of a distinct region of the heart. The electrodes are connected to the positive terminal of the electrocardiograph, and the central terminal Wilson is used as a reference connected to the negative terminal. In the right image of Figure 9, the position of the six precordial leads is shown together with an example of the signal retrieved. [1], [39]

Nowadays, a new technique called body surface potential map (BSPM) has been developed to study the electrical potentials on the torso surface. For obtaining an accurate isopotential map with the BSPM technique is needed a large number of leads, being 32 appropriate. [45] Signals from the leads on the torso surface are processed giving as a result a BSPM, like the observed in

Figure 10 corresponding to a patient with ventricular fibrillation (VF). This technique presents different advantages compared with the traditional ECG. For instance, the great amount of electrodes used in the registration considerably increases the spatial resolution, and therefore might allow to detect events that would be unseen in a traditional ECG [46], [47].

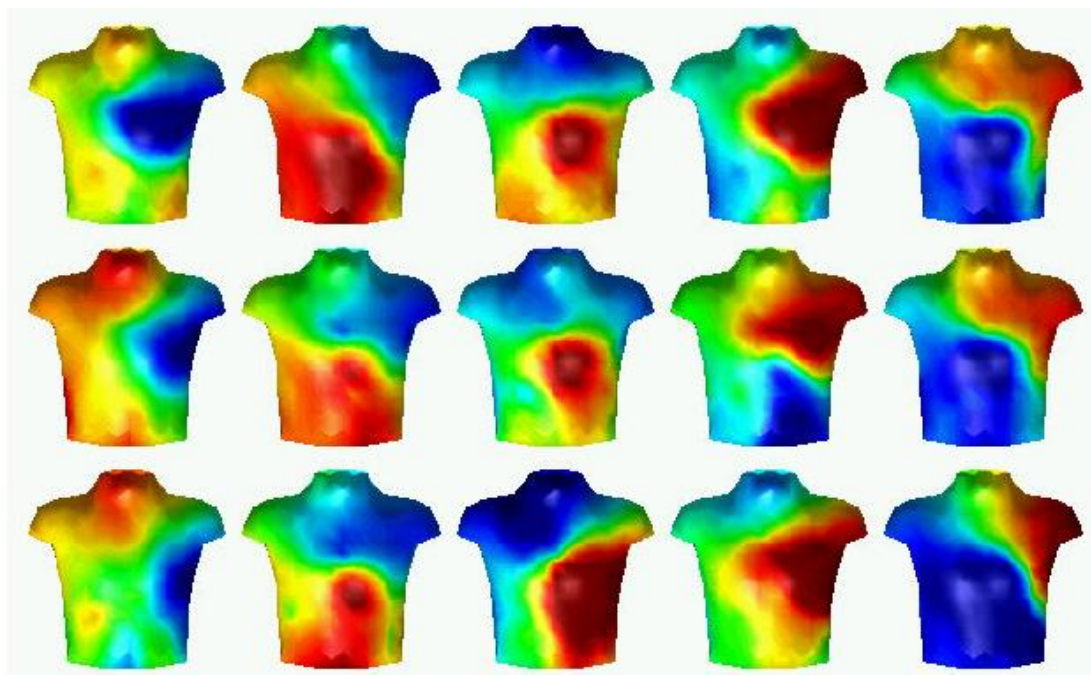


Figure 10. Anterior view of a BSMP corresponding to a patient during VF. Sequence is shown in 40 ms intervals. Yellow and red are positive potentials from lower to higher, and green to blue negative in the same manner. [48]

1.3. ATRIAL PATHOLOGIES

1.3.1. Atrial tachycardias

An atrial tachycardia is characterized by a fast abnormal heart rhythm where the electrical impulse appears in a region different from the SAN. The electrical activation originated in the atria in tachycardias is normally faster than 100 bpm and is usually maintained regular. Atrial tachycardias are a rare form of supraventricular tachycardias. There exists some confusion in the scientific community with assigning certain appropriate terms to specific arrhythmias. [49] The mechanisms causing atrial arrhythmias are triggered activity, reentry, and abnormal automaticity. Depending on where the electrical impulse is created and in its propagation along the atria, atrial tachycardias can be classified in focal and macroreentrant tachycardias. [50]

1.3.1.1. Focal atria tachycardia

Focal atrial tachycardias (FAT) are quite uncommon and they are mostly observed in young patients and normal hearts, but they could appear at any given age. [50] They are defined as a regular rapid atrial rhythm with a characteristic P-wave morphology and originated by an

automatic or triggered mechanism. They can have one or multiple foci that induce the pathological activity. The P-wave varies its shape compared to normal conditions, which will depend on the position of the foci in the atria. The changes in the P-wave morphology could change for each beat in the case of multifocal FATS. They can exhibit variations in the pacing of the autorhythmic foci in slight rate variations with the heart rate ranging between 100 and 250 bpm [51]. Alternating P-waves with a stable baseline on the ECG are an indication of focal tachycardia with quiet periods between the foci, although this is not always true. If there exist areas that block conduction, the activation pattern turns into asymmetric and may look like a macro-reentrant atrial tachycardia (MRAT). The origin of these tachycardias seems to be in different atrial regions including the following: CTS, TV, MV, PV, FO, CS and RAA, and LAA. [52] The difference in P-wave morphology can be noted in Figure 11, where a FAT is compared to a sinus rhythm. The atrial mechanism of FAT provokes a blocked P-wave. [52]

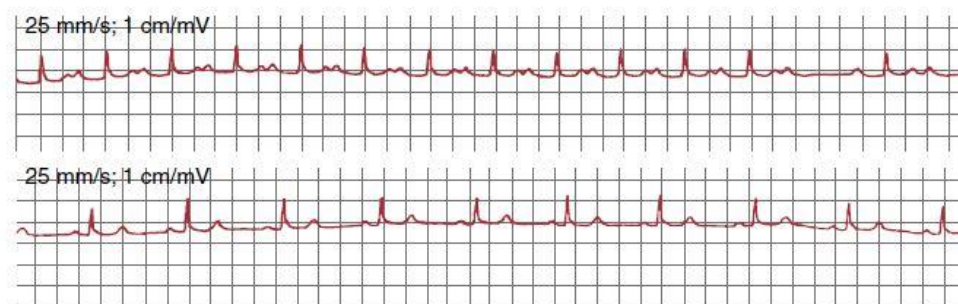


Figure 11. FAT (top) at 100 bpm and sinus rhythm (bottom) ECG signals for lead II in a single patient [52]

1.3.1.2. Macro-reentrant atrial tachycardia

Macro-reentrant atrial tachycardias (MRAT) are characterized by a large circuit, an area of slow conduction, and a zone of unidirectional block [53]. These characteristics are normally determined by anatomical structures that spontaneously create this arrhythmic behavior. They are more frequent in patients with a history of cardiac complications, pulmonary hypertension, prior ablation procedures or heart surgery or any condition affecting the atria. They could be paroxysmal, but they are normally persistent. It occurs in a continuous, uninterrupted way because of the propagation rotating around an obstruction caused by anatomical regions, scars, or areas of functional block. [52] They can be categorized independently by its ECG characteristics, although it could resemble the behavior of an atrial flutter. [52], [53] Macroreentries can be identified in the ECG by covering the entire cycle and by the appearance of the exact same return cycles in two atrial points 2 cm distant. In Figure 12, the different patterns of MRAT in the RA are shown [52]. In Figure 13, an example of a MRAT signal recorded at several leads is shown [53].

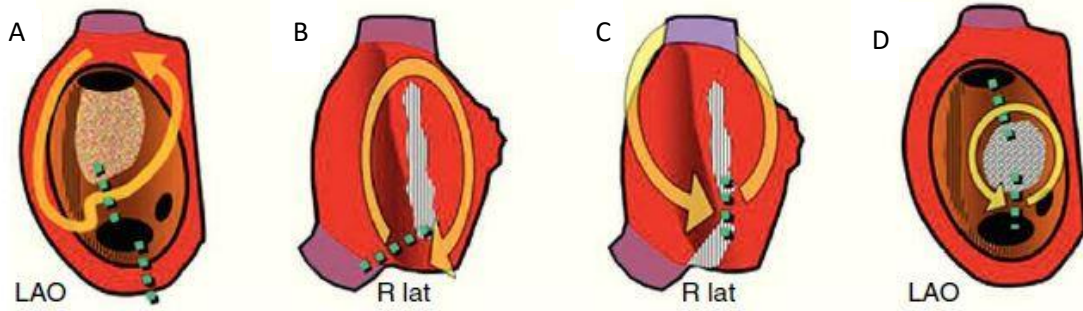


Figure 12. Representation of macroreentrant atrial tachycardia of the right atrium seen in clinical practice. A: MRAT with a nonsurgical low-voltage unexcitable area. B: Scar MRAT without the SVC. C: MRAT with an isthmus between two scars including the SVC. D: MRAT revolving around a septal patch. LAP = left anterior oblique; R lat = right lateral [52]

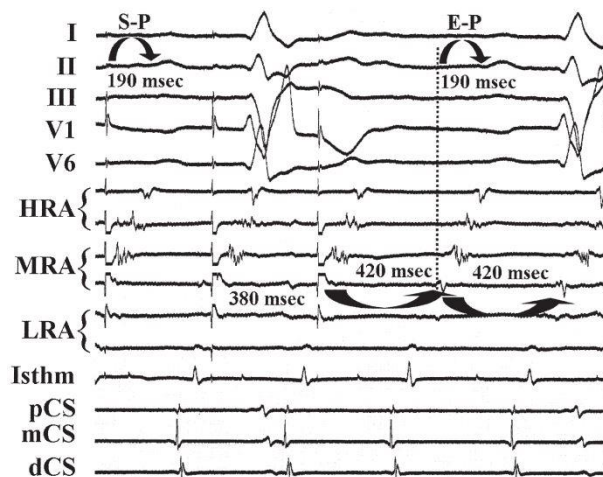


Figure 13. Signals of a patient with a right MRAT with a tachycardia cycle length of 420 ms. HRA = high right atrium; MRA = mid right atrium; LRA = low right atrium; pCS = procimal coronary sinus; mCS = mid coronary sinus; dCS = distal coronary sinus [53]

1.3.2. Atrial Fibrillation (AF)

Atrial fibrillation (AF) is the most common atrial arrhythmia and affects approximately 2 % of the world's population. In the EU, there is close to 10 million cases, and this value is expected to increase in the following 15 years to a number of in between 14 and 17 million patients. [54]

AF is a type of supraventricular tachyarrhythmia which consists on a rapid uncoordinated electrical activity resulting in a chaotic and de-synchronous behavior that leads to a defective mechanical contraction of the atria. [55] The mechanisms that sustain this fibrillatory activity are reentrant mechanisms, structural or functional remodeling, and rapid ectopic activity. [56]–[58]. Under AF, disorganized electrical waves like the ones observed in Figure 14A, cause both atria to contract irregularly at rates above 300 bpm, normally between 400 and 600 bpm. [59], [60] This behavior provokes the atria to contract in a deficient way, not being able to pump blood correctly, what induces also a reduction in the efficiency of ventricular pumping. Nonetheless, AF is not deadly, and patients can leave with it for months or years, unlike with ventricular

fibrillation. However, AF increases the risks of suffering other diseases like a heart infarction or a stroke. [1], [39], [61]

Along history, different theories have been presented for explaining the electrical mechanisms causing this chaotic activity, which are still not well understood today. Firstly, Moe et al 1962 proposed that there exist multiple reentrant waves that block the normal propagation wavefront in the atrial tissue, and constantly create new disorganized patterns. This is one of the most supported hypothesis, and it has been experimentally proved [62]. In 2003, Jalife suggested the mother rotor theory, which insists in that AF is not a chaotic mechanism, instead it is an organized process with uninterrupted periodic activity of discrete reentrant sites. AF is induced by multiple ectopic beats usually originated around the PV that cause the propagation wavefront to fragment and generate rotors. These rotors could become stable in one specific area or could differ its position inducing a chaotic behavior. [56] The rotors have been proved experimentally in studies in animal hearts by means of optical mapping done by Jalife [63], [64], and also in human hearts as reported by Narayan [65].

AF can be recognized by several characteristics in the ECG. First of all, the P-waves are not discernible because the chaotic waves propagating along the atria can have opposite polarity thus canceling each other. Diagnosis can also be done from the analysis of the irregular RR intervals, since activation happens at a fast and variable rate. QRS complexes do not variate and are shown normal except there is a ventricular conduction problem. The heart rate increases and is approximately between 125 and 150 bpm. [1], [39], [66] In Figure 14B, the ECG from a patient in control conditions (top) is compared to the ECG from an individual during AF (bottom).

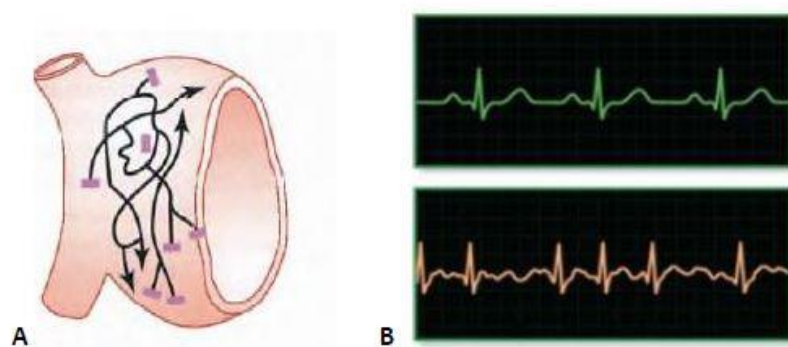


Figure 14. A: Transmission of the electrical impulses in AF [1]. B: ECG in control conditions (top), and AF (bottom) [67]. Figure extracted from [68]

Based on its duration, presentation, and progression, AF is traditionally classified in 5 categories: first-diagnosed AF, paroxysmal which consist on different episodes that could last up to 7 days, persistent which last longer than 7 days but less than a year, long-standing persistent which is longer than a year, and permanent which is always present and there is no hope of recovering to sinus rhythm. [60] Chronic AF (cAF) is a term commonly used [69]–[73], which has several definitions. It normally stands for long-standing forms of AF [74], so in this work it will be used for referring to these types of AF.

1.3.2.1. Chronic Atrial Fibrillation (cAF)

Experimental studies suggest that electrical and structural remodeling appears in both RA and LA under cAF conditions. During cAF, a blockage of several ionic channels is produced, inducing the shortening of the AP duration (APD), inducing shortening of the AP duration (APD) by approximately 62%, as shown in Figure 15 [75]. In Table 3, a summary of the changes in the ionic currents experienced under cAF conditions in both the RA and LA is presented.

	cAF in RA	cAF in LA	Reference
ICaL	-70 %		[71]
	-63%		[76]
	-60/-65%		[70]
	-44%		[77]
IKAch	-47/-50%		[78]
	-54%		[79]
	+45%		[71]
IK1	+100%		[78]
	+0%	+106%	[76]
	+100%	+100%	[80]
	+73%		[79]
	+100%		[71]
IKur	+75%		[70]
	-44%	-53%	[81]
	-60%	-45%	[69]
IKs	-55%		[82]
	+166%	+85%	[69]
Ito	-70%		[71]
	-66%	-61%	[81]
	-44%	-78%	[69]
	-60/-65%		[70]
	-44%		[82]

Table 3. Experimental variation of the ionic currents involved in the cAF electrical remodeling.

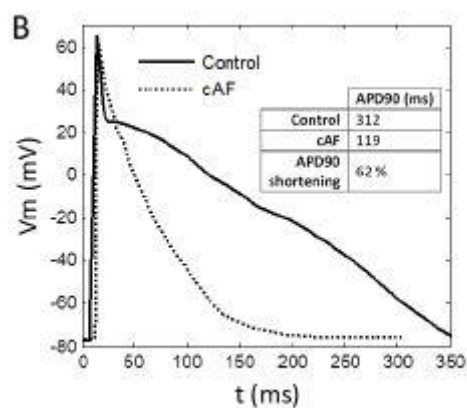


Figure 15. APs in control and cAF remodeling, recorded at a stimulation frequency of 0.5 Hz by Bosch et al. [75]

1.4. COMPUTERIZED TOMOGRAPHY (CT)

A computed or computerized tomography (CT) scan allows to see the interior of the human body by combining a series of X-ray images taken from different angles producing with computer processing cross-sectional slices of the structures inside the scanned object. Since they are combination of multiple X-rays, they provide way more detailed information. Practically all the body organs can be observed in a CT scan, and they are used for diagnosing many diseases and planning surgery or radiation treatments. The data produced indicates the ability of the tissue to absorb the X-ray beam, for example bones contain much Calcium, which has a high atomic number, absorbing most of the X-rays and making them clearly visible. X-rays work worse with soft tissues like the brain or muscle. [83]

A cardiac CT focuses on the heart and surrounding vessels, and typically a specialized contrast dye is injected into the bloodstream for improving the visibility of the area. It allows to see with detail the anatomy of the heart and to diagnose certain cardiac conditions. There exist different types of CT scans targeting the cardiovascular system, which are: total body CT scan, coronary CT angiography (CTA), and calcium-score screening heart scan. The total body scan allows to observe the full torso and analyze the heart, the lungs, and the abdomen areas. This technique is applied in early detection of heart disease. The amount of radiation is larger since it scans the whole torso. The coronary CT angiography (CTA) focuses on the heart and its vicinities and uses an iodine-containing contrast dye which is injected into the blood vessels improving dramatically the quality of the images. For increasing the effectivity of the procedure, medications that slow the heart rate could also be taken. The iodine dye is later processed and removed from the body by the kidneys. The calcium-score screening heart scan is used for detecting coronary calcification and preventing atherosclerosis before the symptoms even appear. It has been proved that coronary calcium affects the cardiovascular system and is a powerful predictor of heart diseases. This screening gives out a calcium score that will indicate the risk of developing a coronary artery disease. [84], [85]

The CT scan exposes patients with a brief dose of ionizing radiation that could damage DNA and cause cancer. This radiation is obviously higher than for a regular X-ray, as the CT scans performs multiple X-rays all around the patient in 360°. Usually the amount of radiation applied can be

considered a low dose and it hasn't been proved to cause any long term harm. For example, the average effective radiation dose for a CT angiogram is 16 millisievert (mSv), and for a cardiac CT for calcium scoring is 4 mSv. [86] It is not known what would be the necessary dose that increases the chances of getting cancer.

1.5. MODELLING THE HUMAN HEART ELECTRICAL ACTIVITY

Computational modelling is used for simulating the activity of complex systems in order to increase the understanding and comprehend the influence of the different factors affecting it. There are computational models that simulate the behavior of cardiac cells, which can be used in 2D and 3D models of the tissue, organ and even body, allowing to reproduce the electrical activity of the heart. They allow us to gain more knowledge about cardiac electrophysiology and arrhythmias, and they can also be used to help the clinicians in the decision-making process, for example for deciding the location where ablation should be performed. The cellular models are composed by a set of mathematical equations that intend to replicate the ionic movements across the membrane and thus the electrical activity generated. These mathematical models need to be developed based on experimental observations for emulating reality as good as possible. [87]

The modelling of the electrical activity of the heart is done in a multiscale manner, going from the cellular level to the body torso. At the cellular level, the models replicate the constant ionic flux of currents that induce the electrical activity of isolated cells. Advancing into the tissue or organ level, the models simulate the electrical interactions between these cells, which gives the spreading of APs through the tissue and generate the electrical propagation. In these models, each node in the mesh is a cell that is simulated with the cellular ionic model. The electrical activity simulated in the heart can be translated into the body model, where ECG signals can be recorded on the torso surface or electrograms inside the atrial cavities. The propagation patterns obtained in the torso can be used to help clinicians better understand the effect of cardiac diseases.

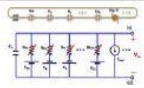
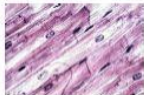
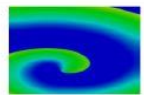
Scale	Biology	Model
Cellular		
Tissue		
Organ		
Body		

Figure 16. Representation of the cardiac multiscale modelling. [75]

The first cellular model simulating the behavior of the cell regarding the movements of ions across its membrane was developed by Hodgkin and Huxley in 1952. A squid's axon was studied for replicating the ionic mechanisms in charge of the initiation and propagation of the APs, and a mathematical model was created based on the experiments performed. [88] Following this Hodgkin and Huxley's work, in 1960 Nobel developed the first model of a cardiac action potential (AP). [89] It was not until techniques like voltage clamp and patch clamp were discovered that more cellular cardiac models were developed. These techniques allowed to measure experimentally and independently the current going through certain channels in isolated cells, helping to adjust the models. Many models have been developed since then, with a focus in the ventricle, although lately many atrial models have also been formulated.

1.5.1. Atrial cellular models

The first atrial cellular models had to wait until 1998, when Courtemanche et al. [90] and Nygren et al. [91] developed atrial models that were based on ventricular ones. At the moment, there are mainly 5 different ionic models that replicate the electrophysiology of the human atria [90]–[94]. These models present different ionic formulations, giving different AP morphologies, as shown in Figure 17.

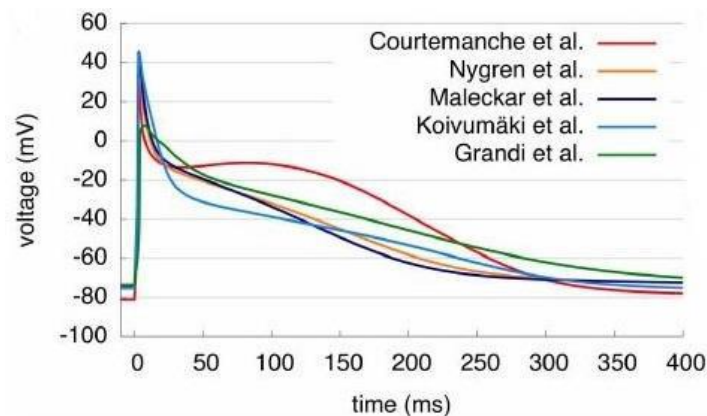


Figure 17. APs of the main five ionic atria models [95]

Depending on the requirements and objective of the work, it might be convenient to choose a different model. In this work, we use the model developed by Courtemanche, Rafael J. Ramirez and Stanley Nattel, [90] hereinafter called CRN model, and that will be explained in detail in section 3.7.1.

1.5.2. 3D models

Segmentation of organs from medical images allows to build geometrical 3D meshes that can be used for simulating at the organ and torso level. These meshes are commonly formed by tetrahedrons or hexahedrons [41]. In the case of cardiac 3D models, each node will represent a cell and will be assigned the cellular electrical model, so differential equations can be solved along the mesh in order to obtain the electrical propagation in the heart tissue. Patient specific heart and torso models can be created from medical images like CT, and they take it a step further in the personalization of the diagnosis and treatment of the patient.

In 2000, Harrild and Henriquez et al. [96] built one of the first anatomically detailed 3D human atrial models. This model included both atria, their major muscle bundles, and anisotropic structures with defined fiber orientation. The unicellular model proposed by Nygren et al [91] was coupled to simulate the propagation of pulses along the atria. In silico investigations at the macroscopic level could now be performed to study the behavior of the atria in normal and pathological conditions.

1.5.3. Numerical and computational methods for solving simulations

When performing simulations at the tissue or organ level, the propagation of the electrical activity of cardiac tissue needs to be established in terms of flux of currents between a cell and its neighbors, not just in based on the action of the ionic currents relative to V_m . In cardiac modelling, ordinary differential equations (ODE) are used for solving the electrical behavior of single cells, and partial differential equations (PDE) solve the propagation of the stimuli along the tissue. Hence, a reaction-diffusion equation is applied, with the reactive part representing the ionic currents in the cells, and the diffusive part referring to the propagation to neighboring cells.

The bidomain model represents the mathematical formulation of the electrical activity of cardiac tissue that is formed by two continuous domains, the intracellular and extracellular. [97] The numeric resolution of equations in both domains has a high computational cost, so the formulation can be simplified, and it can be represented by the monodomain formalism. The monodomain equations are simplified based on two hypotheses. The first one consists in that the variations of the extracellular potential are sufficiently small, so the variations of the transmembrane potential are the same as the intracellular potential. The second one is that since the extracellular potential is so small, its effect on the transmembrane current is negligible, which allows to uncouple the bidomain equations. It can be considered that the conductivity tensors have the same anisotropic variation, arriving to the following formulation of the monodomain model:

$$\nabla \cdot (D \nabla V_m) = C_m \frac{dV_m}{dt} + I_{ion} \quad (2)$$

with

$$D = \lambda / ((1 + \lambda) \cdot D_i) \quad (3)$$

where V_m is the transmembrane potential, D the conductivity tensor, λ an scale factor, D_i the conductivity tensor in the intracellular space, C_m the membrane capacitance, and I_{ion} the sum of the ionic currents in the cellular model.

There is also a need to discretize in space and time the domains in which the simulation is solved. [98] For the task of spatially discretizing the model, a finite element method (FEM) was used. This method is based on an approximation of the exact solution, where the domain is divided in subdomains called elements, and the PDE are solved at the nodes contained in the elements. The global solution is obtained by assembling the solution of all the elements. The temporal discretization can be solved with an explicit method.

CHAPTER 2. JUSTIFICATION, MOTIVATION, AND OBJECTIVES

Cardiovascular diseases are the principal cause of mortality worldwide. In Spain, the cause around 30% of the total number of deaths. [99] Cardiac arrhythmias are among the most significant manifestations of cardiovascular diseases. They affect a high number of people every year and their incidence keeps increasing. As a consequence of deterioration of the health conditions, patients need medical attention more often, supposing higher cost in the healthcare system. Despite the problematic associated with cardiac arrhythmias, details of the mechanisms causing them are not well known, and treatment are not completely efficient. The factors that take a role in the generation of these abnormal rhythms need to be studied in depth, in order to understand better these pathologies and improve prevention and therapy. There exists a high variability between cases. Every person has a different heart anatomy and electrophysiology, that needs to be analyzed and taken into account when diagnosing or treating a cardiac disease, existing a demand in personalized medicine. Experimental and clinical methods have demonstrated mechanisms involved in cardiac arrhythmias, but they present many limitations, as many times it is hard to determine what it is happening in the heart with conventional techniques, which might have a poor efficacy [100], or even novel techniques provide contradictory outcomes [101], [102].

Computational simulations allow to study the heart's electrical activity in a more controlled way. They faithfully reproduced the events observed in the clinical practice and help to understand the underlying mechanisms [103], [104]. They also permit the study of several factors, which might affect the propagation patterns or the efficacy of a treatment, through experiments impossible to carry out in the clinical practice with patients. In addition, 3D models can be developed based on CT scans as patient- [105] or population-specific models [106], reproducing the anatomy of the real patient's heart and torso or of a population of patients with same characteristics. Besides the anatomical properties, atrial heterogeneity can also be added to the models to better reproduce the electrophysiology and obtain simulations of the electrical activity under normal and arrhythmic propagations conditions as realistic as possible.

The general objective of this work is to design a semi-automatic methodology for the creation of highly anatomically and electrophysiologically detailed 3D personalized models of the human atria and torso, in order to be used as a tool for the study of atrial arrhythmias, as well as their diagnosis and treatment. The main objective has been split in the following specific objectives:

- Segmentation of CT images (atria and full torso, including the principal organs) to obtain anatomical surfaces that reproduce the exact anatomy of the patient.
- Design of a semi-automatic algorithm for separating the atria in different regions, taking as input points in the 3D mesh selected by the user.

- Development of the 3D atrial models including the heterogeneous anatomical and electrophysiological properties: different ionic model, conductivity, anisotropy and fiber direction for each atrial region.
- Development of a 3D torso model that incorporates all the organs and their electrical properties.
- Validation of the 3D atrial and torso models in control conditions.
- Generation of atrial arrhythmic activity.
- Analysis of the propagation patterns in control and arrhythmic conditions through the atrial propagation maps, ECG signals and BSPM.

CHAPTER 3. METHODOLOGY

In this chapter, the methodology designed for the creation of highly detailed personalized atria and torso models is presented, as well as the electrophysiological computer simulations performed with the obtained models. In Figure 18, the workflow of the methodology implemented can be observed.

The first step for developing the models was the acquisition of CT images from the patients under study. For this issue, a collaboration with the Hospital Politécnico y Universitario La Fe was established, and they provided CT scans from different patients with heart pathologies. In order to obtain the anatomical structures of the atria and the different organs in the human torso, CT images were segmented. As a result, we obtained patient specific surface models of these regions. After that a conditioning of the surface models was performed and, in case of the atria, an algorithm for distinguishing semi-automatically regions with different histological, functional or electrophysiological properties was developed. Then, the atria and torso models were meshed. Finally, fibers orientation and different materials and ionic model regions, as well as organs conductivities, were defined for the atrial and torso models, respectively, in preparation for the electrophysiological simulations.

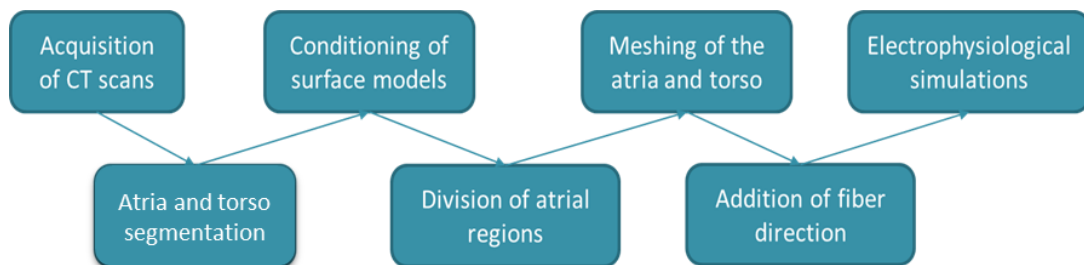


Figure 18. Pipeline of the methodology applied in this work

3.1. ACQUISITION OF CT IMAGES

3.1.1. Patient overview

Patient 3023001 is a 56-year-old smoker man with arterial hypertension, self-limited palpitations since he was 35 years old, and with occurrence of common flutter shown in ECGs. The left atrium appears to be dilated and the septal area shows fibrosis. He wasn't on any medication.

Patient 3014094 is a 36-year-old man, with a bit of fibrosis in the septal zone and in the posterior area of the right superior pulmonary vein (RSPV), and a small area of low voltage also in the septal zone. There is not any cavitary thrombus or relevant alterations.

Patient 3196630 is a male of 67 years with left ventricular dysfunction. Fibrosis is displayed in the posterior RSPV, and a dilated left atrium was detected. There is not any cavitary thrombus or relevant alterations.

Patient 1403865 is a male of 60 years with arterial hypertension and persistent AF. He is an ex-smoker, allergic to ciprofloxacin, without diabetes mellitus or pain. He was first diagnosed with paroxysmal AF in 2007, which then turned to a persistent phase with electrical cardioversions. He also presented symptomatic episodes due to exertional dyspnea. Ablation was performed in 2016 with early recurrence that required cardioversion on several occasions. Both atria were shown to be slightly dilated.

Cardiac structure	3023001	3014094	3196630	1403865
RUPV	17x9 mm	24x25 mm	19x24 mm	19x12 mm
RIPV	21x18 mm	17x21 mm	17x20 mm	22x16 mm
LUPV	23x17 mm	19x11 mm	13x22 mm	17x14 mm
LIPV	9x4 mm	22x17 mm	13x18 mm	16x9 mm
RA	-	21 cm^2	22 cm^2	-
LA	-	31 cm^2	40 cm^2	38 mm diameter

Table 4. Dimensions of RA, LA, and the PV structures for the 4 case studies presented

3.1.2. Characteristics of the CT images

As mentioned before, CT images from four different patients with auricular diseases provided by the Hospital Politécnico y Universitario La Fe were used for the segmentation. Three of the four case studies consisted of heart specific CT scans, from which 3D atrial models were built, whereas the remaining case study consisted of a whole torso CT scan, from which a whole torso model (including the atria) was generated.

Following the Organic Law 15/1999, Law of Data Protection, the treatment of personal information is forbidden, and patient identity must be kept under anonymity. Due to this confidentiality, the patients that were dealt within this work are labelled with an ID assigned by the hospital. The patients' IDs for the 3 cases of atrial models are ID 3023001, ID 3014094, and ID 3196630, while the one for the complete torso is ID 1403865.

In Table 5, the main characteristics of the TAC images used for the generation of 3D models described in this work are shown.

Patient ID	3023001	3014094	3196630	1403865
Manufacturer's Model Name	Philips iCT 256	Philips iCT 256	Philips iCT 256	Philips iCT 256
Study Description	Heart CT Coronarography with Iodine Contrast Agent			
Body Part Examined	Heart	Heart	Heart	Chest
Acquisition Date	18/06/2018	20/07/2018	19/07/2018	21/03/2019
Nº of slices axial plane	634	474	336	319
Nº of slices sagittal and coronal plane	512	512	512	768
Slice thickness	0.8	0.8	0.625	3
Spacing Between Slices	0.4	-	-	-

Table 5. Main characteristics of the CT scans for each of the case studies

3.2. SEGMENTATION OF THE ATRIA AND TORSO FROM CT IMAGES

The first step in the process of creation of the 3D models is the segmentation of the anatomical structures from CT images. For this task, the software Seg3D, the volume segmentation and processing tool developed by the NIH Center for Integrative Biomedical Computing at the University of Utah Scientific Computing and Imaging (SCI) Institute [107], was used. This is an Open Source free tool, with which users can visualize and label medical image volumes, apply imaging processing algorithms and perform manual segmentation on the desired anatomical regions. The program possesses different functions, tools, and filters to achieve the goal of segmenting manually or semi-manually medical data. In Figure 19, the Seg3D interface is shown, with different tools (left panel) and the created masks (right panel). In the following sections (3.2.1 and 3.2.2), the process of segmentation of the atria and of the different organs in the torso will be explained in detail.



Figure 19. Seg3D interface, showing the CT scan of patient 3023001.

3.2.1. Segmentation of the atria

After opening the Seg3D software, we first imported the CT scans. Among the different visualization options, we primarily used the Only One Viewer choice, with the axial cut outlook. Brightness and contrast needed to be adjusted in order to visualize and distinguish the different regions of the heart. The objective structures were the RA and LA, but the aorta artery and the RV and LV were also segmented for defining the boundary regions.

The procedure followed for segmentation consisted of the definition of a seed in the target area (see Figure 20). Then a segmentation filter, which was able to find the regions in the data volume similar to the given original seed, was applied. Afterwards a manual adjustment of this semi-automatic segmentation was performed cut by cut, and finally a smoothing filter was applied. For defining the seed, a new mask layer was created, and the Paint Brush tool was used to paint the target area along an approximately equally-distanced number of slices. The Segmentation Level Set tool expanded the given mask layer to the surrounding pixels that match the statistics of the original seeded area. The following parameters can be adjusted when using this filter [108]:

- Iterations: sets the number of times that the filter propagates the seed before terminating.
- Threshold Range: is the strictest parameter as it controls the intensity values that are going to be included in the propagation of the segmented region. High values will accept a higher range of intensity values, expanding with more ease. This range is associated to the standard deviation of the original seed volume.
- Curvature Weight: control the propagation edge in terms of curvature.
- Propagation Weight: parameter that controls how aggressive each iteration will be in determining surrounding pixels that may fit the criteria of the filter.

- **Edge Weight:** this parameter controls how much effect the edges in the data volume affect the propagation pathway, although, this parameter will not be used and will be kept 0.

There exists a tradeoff between the number of iterations and the Propagation Weight, and the number of cuts and distance between them of the painted seeded area. An adjustment of these parameters needs to be performed to obtain the best possible semi-automatic segmentation of the desired structure. For example, for the segmentation of the right atrium for patient 3023001, the following parameters were used: Iterations: 234, Threshold range: 2.00, Curvature Weight: 3.60, and Propagation Weight: 4.00.

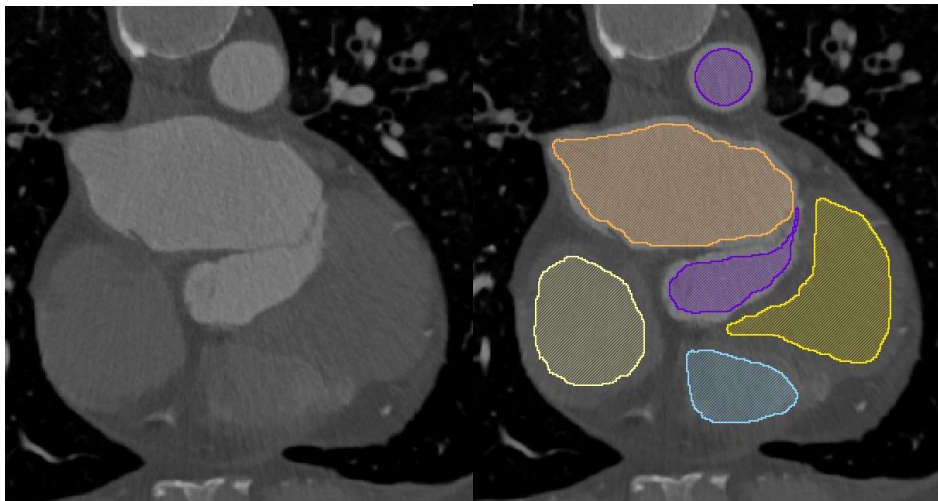


Figure 20. Segmentation seeds for the 5 principal heart structures for patient 3023001: LV in dark yellow, RV in blue, LA in orange, RA in light yellow, and aorta in purple.

After segmenting both atria and ventricles, some manual adjustments and automatic filters (Dilate/Erode) were applied for a first smoothing of the segmentation. Finally, the Boolean REMOVE filter was used for avoiding collision of the different segmented surfaces, prior their exportation as an isosurface with .vtk format for further visualization and processing.

This process was done with the CT scans of patients 3023001, 3014094, and 3196630.

3.2.2. Segmentation of the torso

The same procedure was followed for the segmentation of each organ in the torso corresponding to patient 1403865. The organs segmented apart from the atria were liver, kidneys, lungs, bones, main blood vessels, surface of the torso (skin), and ventricles. For the segmentation of the atria and ventricles, a crop had to be done to zoom in the area for facilitating the task. It is notable to mention that the segmented atria model from the torso CT had worse resolution than the ones segmented from the heart specific CT scans.

For the different organs, brightness and contrast were adjusted to discriminate the target region in a better way. For example, for segmenting bones, a brightness of 62, and a contrast of 77 were applied, as depicted in Figure 21.

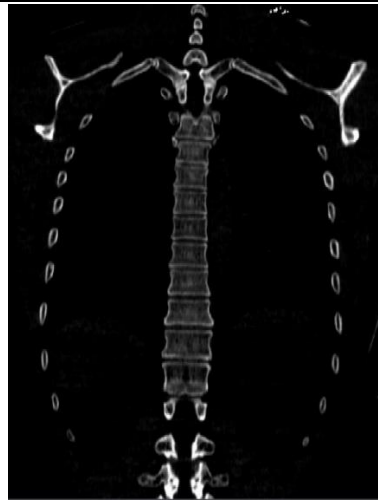


Figure 21. Coronal view of the CT scan for patient 1403865 with the brightness and contrast adjusted for visualizing the bones

In Figure 22, we can observe all the segmented organs in the coronal view of the torso CT.

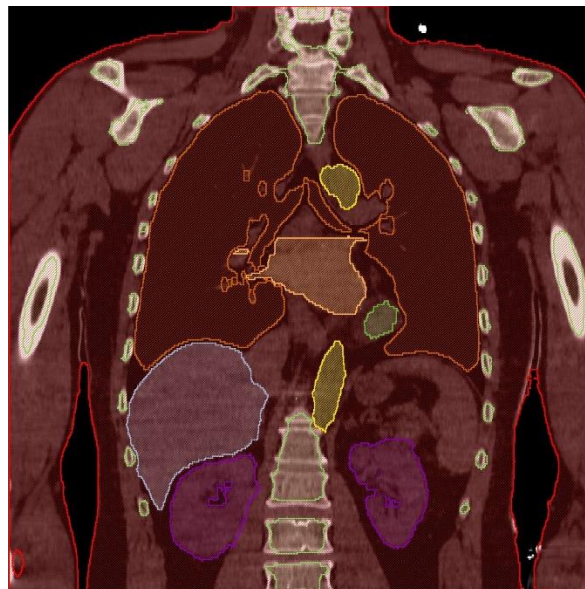


Figure 22. Segmented regions of the main organs of the torso for patient 1403865 in coronal view. In dark orange the lungs, in blue the liver, in purple the kidneys, in yellow the vessels, in dark green the ventricles, in light orange the atria, in light green the bones, and in red the whole torso.

This was done for the patient 1403865.

3.3. CONDITIONING OF THE SURFACE MODELS

3.3.1. Automatic and manual smoothing

The surface models are quite rough after segmentation, so a severe smoothing is needed. For this purpose, as a first approach we used Paraview, an open-source software for data analysis and visualization. The Smooth filter from Paraview was applied with 1000 iterations, as shown in Figure 23. On the left column we can observe the RA and LA surfaces directly obtained from the segmentation with Seg3D (patient 3196630), while in the right column are depicted the surfaces after smoothing.

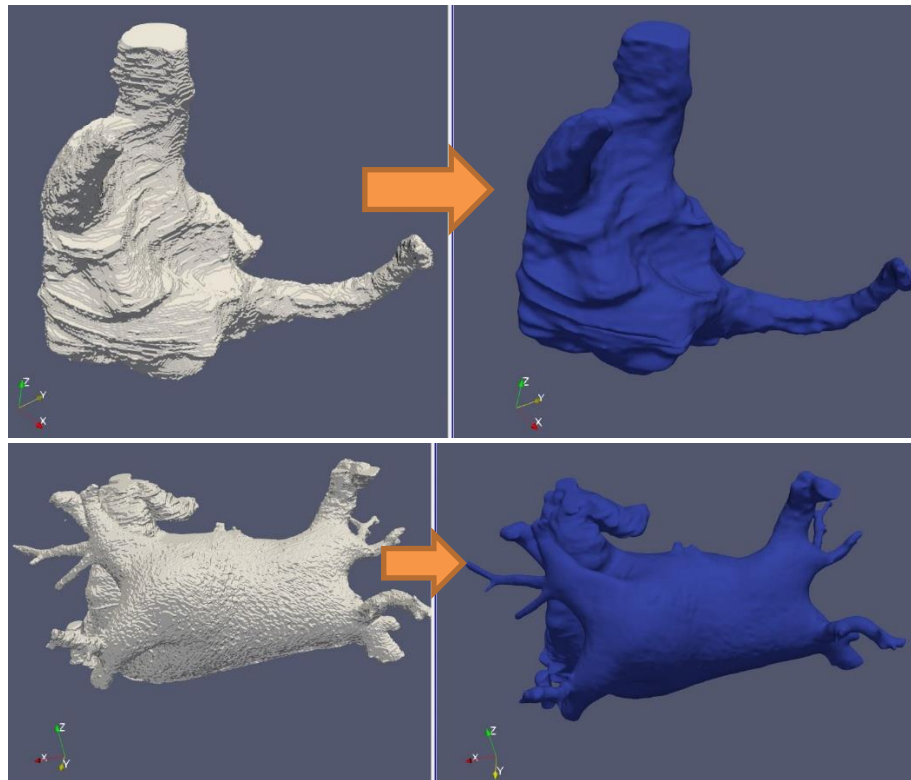


Figure 23. Surfaces before (left column) and after (right column) smoothing (1000 iteration) performed in Paraview: right atrium (top) and left atrium (bottom) geometries from patient 3196630.

Nonetheless, the automatic smoothing performed by Paraview was not enough for our purposes, mainly in very rugged regions, so a manual smoothing focused on that regions was performed with Blender, a free and open source 3D creation suite. In addition to the smoothing, Blender was also used for joining both atria and adding thickness to the surface model. First, the geometries were imported into Blender in .stl format (previously saved in Paraview) and then we edited them in Sculpt mode (see Figure 24), in order to obtain a continuous polished mesh by locally smoothing. Then we exported the meshes as a .stl file for further manipulations.



Figure 24. Blender interface in Sculpt mode showing the available brush tools. The left atria from model with patient ID 3196630 is shown after manual smoothing.

3.3.2. Cutting off vessel extremities and opening of the valves in the atria models

Our models need to have openings in the veins (SVC, IVC and PV), as well as in the MV and TV located between atria and ventricles. Therefore, we generated such orifices with Paraview. For making the openings of the MV and TV, both valves were delimited by using the ventricle models segmented with Seg3D. As shown in Figure 25 (top image, left), the contour of the area corresponding to the valves was selected and extracted from the surfaces. For the slicing of the vessel extremities (SVC, IVC and PV), we decided to make to the cuts approximately 1.5 cm above the initiation with the Clip tool, either with the clip type being a box (Figure 25, top right) or a plane (Figure 25 bottom).

The models were saved again as .stl files for further editing in Blender.

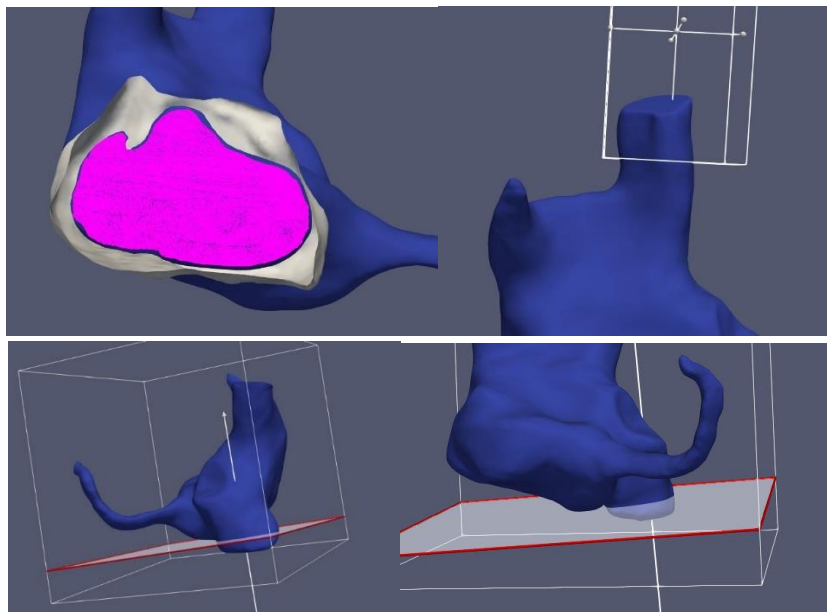


Figure 25. Orifices made in Paraview for patient 3196630 models: cell selection tool (top left, in pink) and Clip tool (box: top right; plane: bottom).

3.3.3. Joining atria and adding thickness to the surface model

After opening the valves, some faces had to be removed in the Edit mode of Blender to make the valves edge uniform (see Figure 26). At this point, we finally had separately the refined model of the RA and LA, which needed to be united together.

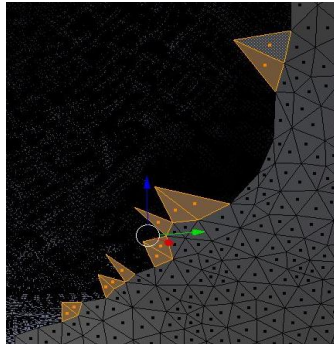


Figure 26. Removal of extra edges in the valves in Blender.

Anatomically, both atria are connected by the BB, the FO, and various connections in the CS. These structures do not appear clearly on the CT scan, so they cannot be segmented. Therefore, we surmised the location of these unions based on 3 criteria: the examination of the anatomy of our models together with the CT images, the comparison with previous atrial models developed by the Ci2B laboratory and the advice of Dr. Sánchez- Quintana, who collaborates with the Ci2B.

In order to join RA and LA surfaces, we used Blender in Edit mode to select the area of the union. As an example, in Figure 27 are shown the selected faces to be removed (left) and the generation of the union (right).

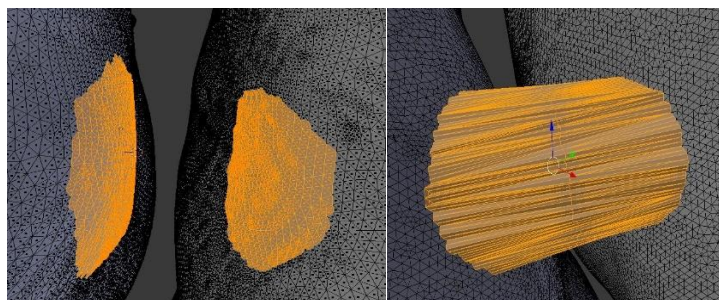


Figure 27. Removal of faces where the FO is established (left) and union of both atria by the FO for patient 3023001 model.

The new added structures were smoothed to obtain uniform connections and end up with a mesh that unified both atria. The resulting unified mesh was the outer surface of the atrial mode, i.e. the epicardium. In order to make the endocardial walls, we shrunk the final smoothed RA and LA surfaces obtained in the previous step up til the thickness was 0.9 mm. As done before, we unified the outer surface and the inner LA and RA surfaces. The epicardium surface with connections on the BB, FO, and CS, as well as the two endocardium surfaces for the RA and LA can be observed in Figure 28.

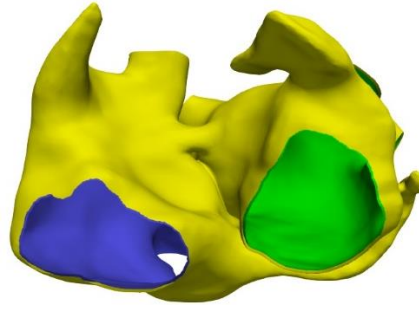


Figure 28. 3 atria layers (epicardium and 2 endocardium) for patient 3196630 before closing the surface model. Epicardium in yellow, RA endocardium in blue, and LA endocardium in green.

The final step in the creation of the atrial surface model with thickness was to close the openings in the vessel extremities and the valves. A procedure similar to the creation of the connections between both atria was performed for this purpose. We first selected the contours to be closed (Figure 29A). Then we added new elements to the mesh in order to close the contours of the outer and inner surfaces selected (Figure 29B). Last we performed a partition of the elements generated (Figure 29C) and converted them into triangles (Figure 29D). This procedure was repeated for all the openings in veins and valves.

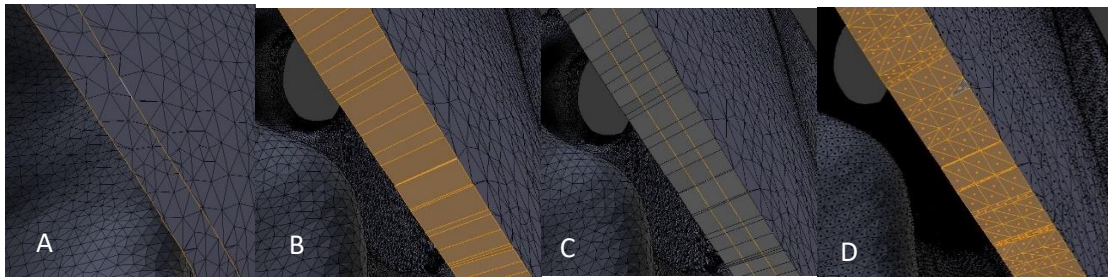


Figure 29. Process of joining epicardium and endocardium. A) Selection of the contours to be closed in the inner and outer surfaces. B) Addition of elements between the selected contours. C) Partition of the elements created. D) Conversion of squared elements into triangles.

The final atrial surfaces to be volumetric meshed will be shown in the results section.

3.4. DIVISION OF THE ATRIA SURFACE MODELS IN DIFFERENT ANATOMICAL REGIONS

Due to the high heterogeneity of the atria, we needed to differentiate our model in different anatomical regions to be assigned different conduction properties, ionic models, and fiber direction. Therefore, one of the goals of this work was to create a semi-automatic algorithm able to divide the models in the desired regions from a set of points and cells in the 3D mesh., in order to achieve the same level of detail as in the model developed by Ferrer et al. [5]. This algorithm, developed in Matlab, divided first the mesh into RA and LA and then semi-automatically delimited the different regions within each atrium. Finally, a few manual modifications were performed for achieving the final labelled surface mesh. The algorithm, which improves a previous work carried out in the Ci2B by Roberto [109], is explained in detail in the following sections. All the Matlab routines are shown in the Annex.

3.4.1. Labelling RA-LA

Elements in the atrial mesh were labelled as RA or LA region based on the comparison between their centroids and the centroids corresponding to the elements in the separated LA and RA surfaces. Centroids were computed with the filter called Cell Centers in Paraview, and were used as an input for the Matlab routine, where the `pdist2` function was used to find the smallest distance between a given element in the atrial mesh and all the elements in the RA and the LA. At this point we worked with meshes saved in `.vtk` format. In addition, we also applied the filter Generate Ids to the atrial mesh in order to keep always the same ID data for points and cells, regardless of the modifications done during the process.

The algorithm reads the atria model and the 3 centroid files, and it calculates the distances from the centroids of the atria model to the centroids of the RA, and to the centroids of the LA. A `CellData` struct was created in the atrial mesh `vtk` with the name RA-LA, where a 1 was assigned if the cell belonged to the RA (distance from that cell centroid to the closest centroid from the RA surface was smaller than for the closest centroid from the LA surface), and a 2 if it belonged to LA (distance from that cell centroid to the closest centroid from the RA surface was higher than for the closest centroid from the LA surface). In the results section images of the labelled models are shown.

3.4.2. Semi-automatic region division algorithm

The objective was to write an algorithm capable of dividing the atria model in all the regions defined in Ferrer et al. [5] by giving as input certain points and cells. This was tried to be achieved with the least possible number of seed points and cells and with the highest precision. Due to the high number of regions, exactly 45, 32 or 35 points, depending on the number of CS connections, and 24 cells were needed for the algorithm to divide the model in the atrial regions. This leads to a ratio of approximately 1.3 points or cells per region.

A `CellData` structure by the name of ORGANID was created in order to assign a different number to each of the different anatomical regions. The algorithm was designed in such a way that the user introduces the seed points and cells and provides as outcome the labelled mesh.

The first part of the algorithm was based on a previous work by Krueger et al. [110]. It consisted in the selection of 3 points, calculating the path that travels the shortest distance along those points in the 3D mesh, and finding the cells that are a given distance away from the points in the obtained path. This procedure was applied to define the following regions surrounding a region: MV, TV, RPV, LPV, IVC, CTS and CS. With this approach, the regions created were uniform and maintained the shape of those structures. In Figure 30, the IVC and the MV corresponding to patient 3014094 can be observed as an example.

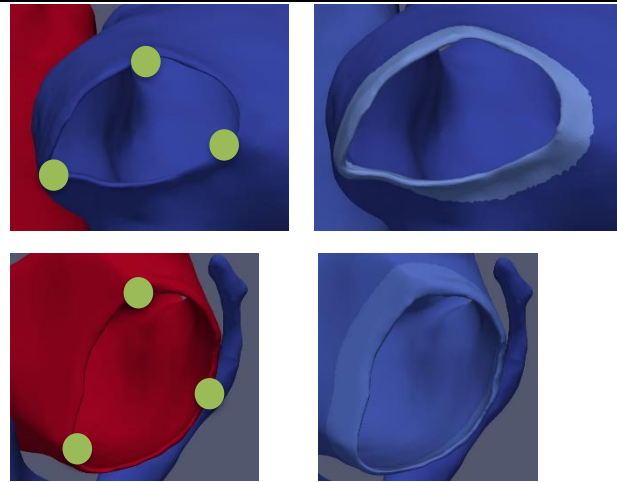


Figure 30. Definition of regions surrounding an orifice: points selected as input for the algorithm (left column) and area provided as a result by the algorithm (right column) for the IVC (top row) and MV (bottom row), corresponding to patient 3014094.

For calculating the path between 2 points in the 3D mesh, we used the Dijkstra's Shortest Path Algorithm created by Joseph Kirk [111] that finds the shortest path and distance from a starting node to an ending node. The code is shown in the Annex in section 8.1.3. Except for the Crista Terminalis (CTS), where the path was calculated from point 1 (at the SAN) to point 2 and from point 2 to point 3, for the rest of the structures the complete path was obtained from point 1 to 2, from point 1 to 3, and from point 2 to 3. This method requires the data of the edges of the mesh, so in Paraview we need to use the filter Extract Edges and save it as a .vtk file. Multiple functions were created for obtaining the cells belonging to these regions. An algorithm for the pulmonary veins (regionPumony, 8.1.6), for the crista terminalis (findCT, 8.1.7), and for the rest of the regions (findREGION, 8.1.5). There is an intermediate function that prepares the data for running the Dijkstra algorithm called findcurveNEW (8.1.4).

For the rest of structures, the algorithm is based on the methodology proposed by Roberto [109]. It consisted on defining delimiter cells by using the coordinate system to constrict the anatomical regions, as all the models acquired have the same spatial orientation. The number of delimiter cells depends on each region. An example of how the program works for delimiting regions with one cell is the following: all the cells which have lower x coordinates than the given cell and belong to the LA will be assigned to the RPVB, as it can be observed in the top images in Figure 31. Instead of using just this mode of operation of marking the bounds by taking all cells with greater or lower x,y, or z coordinates like Roberto [109] did, the possibility of establishing straight lines and curves for defining the boundaries was implemented. With this mechanism, the regions can be defined with much more precision and are adjusted to reality. For establishing the straight and curved boundary lines, one coordinate axis was fix and the other two are used. In the middle and bottom pictures in Figure 31, we can see the application of the straight and curved boundary lines respectively.

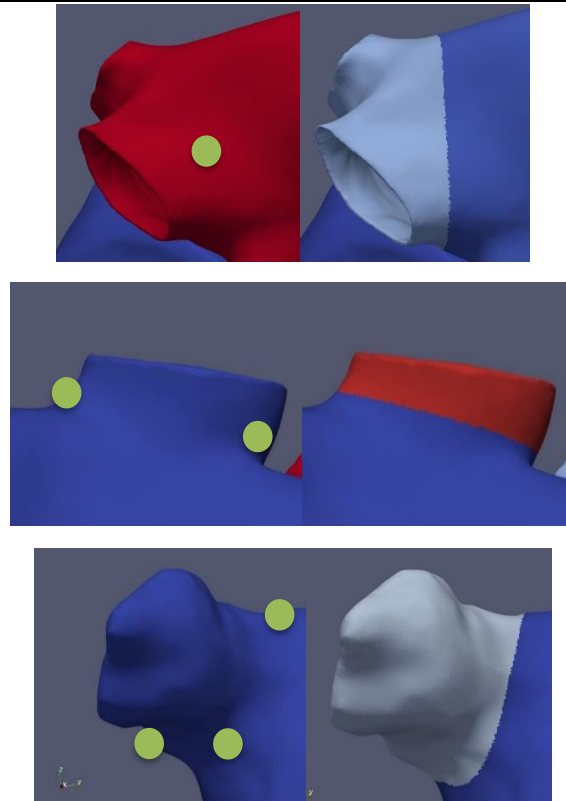


Figure 31. Second mechanism of atrial region division for RPV, UVC, and RAA for model 3014094. In the left the points given as input for the algorithm and in the right the result given. Now, we have a .vtk model with the cells divided in regions in the CellData ORGANID.

3.4.3. Final modifications

There are some final modifications that need to be made before reaching the final labelled atria surface model. The pectinate muscles were assigned by the semi-automatic division algorithm in both the external and internal surfaces, while they should only be present in the endocardium. An algorithm was written for assigning back the pectinate muscle cells of the epicardium to the regions IB and RLW. In Paraview, we needed to first apply a Threshold for getting the pectinate muscles, apply a Connectivity filter, make a Threshold of the regions that belong to the epicardium, and extract their centroids with the Cell Centers filter. Also, we needed to make a Threshold of the HIC and wall regions and extract their centroids.

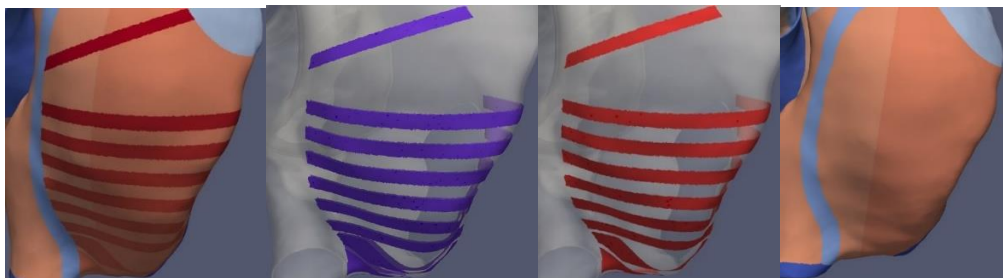


Figure 32. Process of deletion of PM in the epicardium for model 3014094.

In the case there are any small details in the region separation that need to be addressed, manual changes can be performed. There is a commented code to execute this manual assignation at the beginning of the main region division algorithm (8.1.2). In Paraview, the cells desired to be reassigned were selected with the Select Cells with Polygon tool, they were extracted, and then saved. The images of the final labelled surface models can be observed in the results sections.

3.5. MESHING OF THE ATRIA AND TORSO MODELS

3.5.1. Meshing the atria

A volume mesh needs to be created from the surface model for performing electrophysiological simulations. The generation of a volumetric mesh consist on filling the surface model with finite elements creating a solid filled volume model. The meshing was achieved using hexahedral finite elements, as Elvira, the electrophysiological simulation software, is able to solve meshes with this type of finite elements. More specifically, the generated volume meshes are based on irregular hexahedral elements. This means that the volume models have irregular hexahedrons with the shape of an imperfect cube that deforms in a greater or smaller way to adapt to the anatomy. These hexahedral elements are formed by 8 nodes and 6 faces. We want these finite elements to have a uniform size, so every region has a similar node to node distance, as this will influence propagation on the simulations.

The program used for meshing the atria models was MeshGems, which is a trusted meshing software that incorporates fast, reliable and quality meshing capabilities for simulation, optimization and digital product development processes. MeshGems-Hexa, which is fully automatic and requires only a few parameters to control the generated mesh, was explicitly used. [112] The input must be a discrete triangulated surface mesh in the .mesh format. For converting our .vtk surface model into .mesh format the software Gmsh, which is a free 3D finite element mesh generator with a built-in CAD engine and post-processor [113], had to be used. Gmsh does not work with .vtk files, so the model needs to be saved as .stl in Paraview, and then introduced into Gmsh. This tool provides a fast, light and user-friendly meshing mechanism with parametric input and advanced visualization capabilities. MeshGems-Hexa was executed and runned by introducing a series of commands, that are detailed below:

```
run_mg-hexa.bat --in surfMeshes\SurfaceMesh.mesh --out volMeshes\VolumeMesh.mesh --min_size 0.4  
--max_size 0.4 --components outside_skin_only --compute_ridges no --recover_sharp_angles no
```

The minimum and maximum element size was given as an input, with both being 0.4 mm for trying to constrict the element size and make it as uniform as possible. The volume meshes were obtained in .mesh format, so the conversion to .vtk was needed. For this task, a Matlab code programmed by a member of the Ci2B was used to perform this conversion.

As mentioned before, all the atria models were created with a thickness of 0.9 mm. The messing process was successful for all the models at this thickness except for 3196630, resulting in a mesh with holes. To solve this issue, the surface model was redone in Blender increasing the thickness to 1.2 mm and meshed as detailed above. This time the resulting volumetric mesh was satisfactory, being smooth without any holes.

3.5.2 Meshing the torso

The meshing of the torso model was done with tetrahedral finite elements instead of hexahedral. For this task, we used the program TetGen, developed at the Weierstrass Institute in Berlin, which can generate tetrahedral meshes of any 3D polyhedral domain [114]. First, we needed to prepare the surface models that we are giving as input for the meshing. Since TetGen will preserve the input surface mesh, and we want handleable mesh with an adequate number of elements and nodes, a remeshing of the surface models of the torso, atria, and rest of the organs had to be done. This was performed in Blender with the Remesh modifier tool, which gives an output that follows the curvature of the input with a quad topology. The smooth mode was used, and the parameters octree depth, scale, and sharpness were adjusted. Since the resulting remeshed surfaces is a hexahedral mesh, we had to open them in Paraview and apply the Triangulate filter to bring them back to a triangle surface mesh. In Figure 33, the remeshed triangulated models of the torso and atria can be observed, but the rest of organs were also remeshed and used as input for the volumetric torso model. In Blender, we had to make sure that there were no face, edge or point intersections between the different organ models by sculpting the meshes with the brush tool. This is extremely important, since the meshing process will fail if there is any contact between the models.

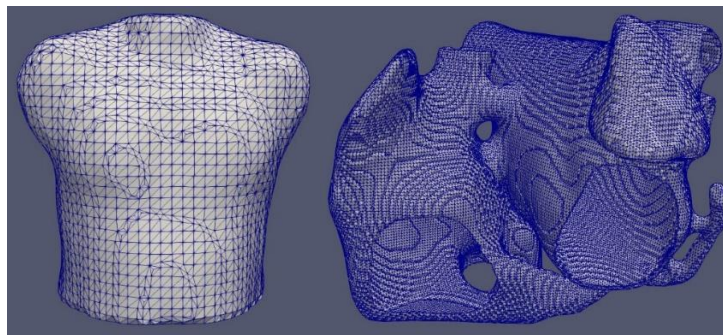


Figure 33. Remeshed surface models of the torso and atria given as input for the volumetric meshing of the torso model. The rest of the organ structures were also given as input even not shown in the Figure.

Now, we selected in Paraview these models and applied the Append Datasets filter to bring them together. We saved it as a .stl file that will be given as input for the meshing of the volumetric mesh in TetGen. We executed TetGen and start the meshing with the following command:

```
./tetgen -pYAq1.1kVC torso_atria_final.stl
```

Each letter is a command with a different function: p tetrahedralizes a piecewise linear complex (PLC), Y preserves the input surface mesh, A assigns attributes to tetrahedra in different regions, q1.1 refines the mesh with a maximum radius-edge ratio of 1.1, k outputs a .vtk mesh file, V gives detailed information about the meshing, and C checks the consistency of the final mesh. The A command will create a CellData property with the different organs that were given as input labelled.

3.6. PREPARATION OF THE VOLUME MODEL FOR SIMULATIONS

3.6.1. Mapping RA-LA and ORGANID properties into the volume model

The ORGANID properties were defined for the surface mesh, although after the meshing, a volume model was obtained without maintaining the properties of the surface one. The meshed volume mesh generated with MeshGems creates a PointData property called `surfnodes` that labels with a 1 the nodes that are in the external surface and with a 0 the rest of them. This data will be useful for differentiating the BB in inner and outer regions, which will be explained in the next point. We opened the volume mesh in Paraview to extract the centroids with the Cell Centers filters, also applied the Generate IDs, and save both files. In Matlab, we needed to open the volume models with the generated IDs, and the one obtained from MeshGems and add the PointData properties of the latter to the first.

A mapping of the RA-LA and ORGANID needed to be done from the surface to the volume model. For this task, a Matlab algorithm, which can be discovered in the section 8.1.10 of Annex, was created to perform this mapping. This process is similar to the one done for the initial RA-LA labelling, by using the centroids of the surface and volume models, and by means of the Matlab function `pdist2`, the smallest distances between the centroids of both models were calculated and the indexes of the centroids of the surface model closest to each of the centroids of the volume model were obtained. The CellData properties RA-LA, and ORGANID were transferred into the volume model by assigning the ones of the closest centroids from the surface mesh. Both RA-LA and ORGANID properties are only defined for cells as CellData, but it will be needed to have them for points/nodes as PointData, since the ionic models will be defined in points instead of cells. An identical procedure was performed between the centroids and the points of the volume mesh, and labelling RA-LA and ORGANID also for points. The volume model was then saved with the `struct2vtk` function.

3.6.2. BB regions separation and insulating

Now, the volume model was labelled in left and right atrium (RA-LA) and in the different anatomical regions (ORGANID), but there were still some details that need to be corrected. In the first place when designating the ORGANID regions, the whole Bachmann Bundle (BB) was defined as one structure. The interior of the BB is insulating and does not propagate APs, but the exterior creates a ring where the AP pulses spread through. An algorithm, located in the Annex section 8.1.11, was designed for dividing the BB in 4 regions: exterior left BB (ELBB), exterior right BB (ERBB), interior left BB (ILBB), interior right BB (IRBB). The algorithm takes advantage of the PointData `surfnodes` property that indicates which nodes are on the surface and finds 3 layers of cells for defining the exterior BB. Dividing into RA and LA was quite simple since there is the PointData and CellData property of RA-LA. By this manner, we pass from 1 BB region in the surface model, left image in Figure 34, to the 4 necessary BB structures in the volume model, shown in the middle and right images in Figure 34.

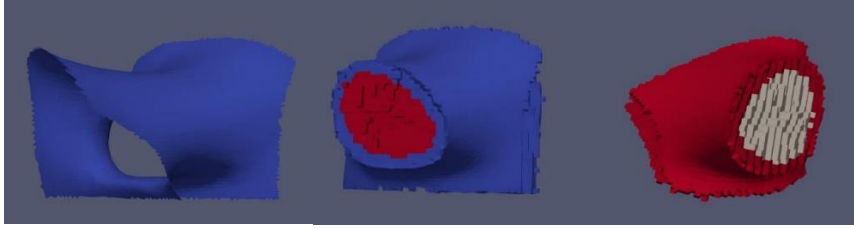


Figure 34. BB before (left) in the surface model and after (middle and right) BB region separation in the volume model for patient 3023001.

After performing the meshing, for most cases in the volume model there appears two regions that are specially compromised. These two regions are adjacent to the FO and the SCc and establish a connection between RA-LA where they should not be united. This is due to the tiny distance between the walls of RA and LA in the surface model and the given mesh element size, propitiating the appearance of cells that bind these walls where there is not supposed to. When running 3D simulations these connected regions will propagate in a fast way the AP pulses from one atrium to the other inducing a surreal behavior. The solution to this inconvenience was to label the cells and nodes that connect RA and LA through these regions with conductivity 0 (insulator) so the propagation would only occur through the defined FO and CSc. An algorithm was designed for this purpose, which can be observed in the Annex section 8.1.11, where the ORGANID of the regions that establish the union between RA and LA should be given, and the cells and points forming this contact are assigned ORGANID 23, that corresponds with the inner FO and has conductivity 0. In the left image of Figure 35, it can be observed how in the surface model RA and LA and only connected by the CSc and the walls are close although not in contact. The same happens for the FO in Figure 36. In the middle images of these figures, the volume with ORGANIDs after doing the mapping is shown, and it can be seen how RA and LA are bound where they are not supposed to. In the right pictures, the area in red shows the cells and points that the algorithm has labelled as insulator.

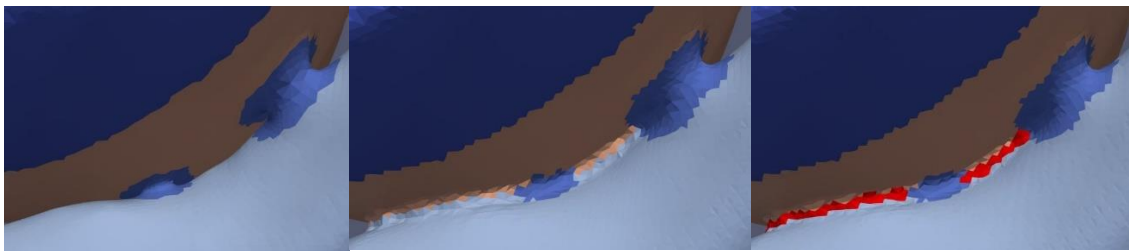


Figure 35. Insulation of the cells that should have not been connecting the CS and the LWLA for model 3023001.

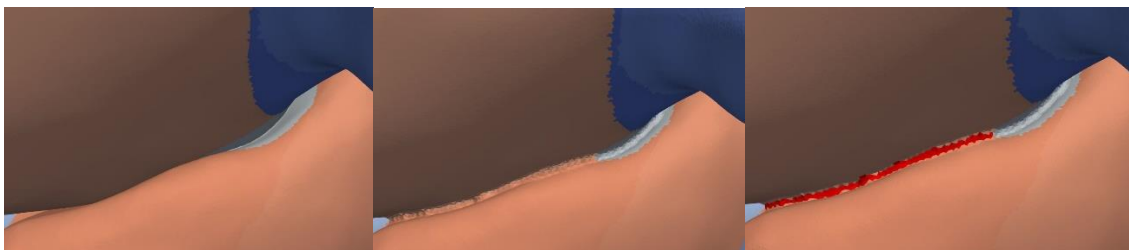


Figure 36. Insulation of the cells that should have not been connecting the walls of LA and RA for model 3023001.

3.6.3. Material, ionic model and fiber orientation

The last step before performing the electrophysiological simulations was the assignment of materials, ionic models, and fibers, and the preparation of the model for Elvira. We have obtained the final volume model with 48 different regions defined in the PointData and CellData ORGANID properties. From these 48 ORGANID regions, 41 have different materials, ionic models, and fibers, which were assigned by an algorithm designed to generate these properties. This reduction is done because in the ORGANID property there were differentiated 8 different PM, which have the same fiber orientation, so they can be defined as one region. The Matlab code is located in the Annex section 8.1.12. Material properties were defined in the cells, so a new property was created in the CellData structure and by means of a switch function the corresponding material was assigned to each ORGANID region. On the other hand, ionic model properties are defined in the nodes, so a property was added to the PointData and in the same manner each region was labelled with its corresponding ionic model.

Finally, before starting with the electrophysiological simulations was the introduction of the fiber direction in the final volume model. The directions of the fibers were replicated from the atria model created by Ferrer [28]. These fiber orientations were obtained from histological data of a diffusion tensor image (DTI). This type of data was not available for our patients, so fiber direction of our models was defined emulating the mentioned model [28]. The user needed to select two points, forming a vector creating a directive that is perpendicular to the desired direction of the fiber, that is previously known. For every region, these two points that create the directive were introduced in an Excel sheet. The cross product between the normal of each cell and the given directive is performed, resulting in the fiber direction. This method using the normal direction adapts in a great way to the regions with curvature and confers better precision. This procedure is detailed in Figure 37, where the cross product of the mentioned vectors culminating in the fiber direction is shown. This approach was applied to every region, except for the BB, FO, and CSc, where the fiber direction will be equal to the directive administered. In Figure 38, examples of the selection of the points creating the directive are shown. For the LIPV and LAA using the cross-product method, and for BB with the fiber direction being the same as the directive.

A Matlab algorithm was used for defining the fiber direction of each region, present in the Annex section 8.1.12. Firstly, the distance between centroids of the surface and volume models was calculated with the pdist2 function. The surface model elements are used for obtaining the normal, since using the volume elements are not useful in this case. For each element of the volumetric mesh, the normal component of the closest surface element is assigned. The directives are imported from the Excel file, and the cross product is performed for each cell, assigning fiber direction in a new property for the CellData structure.

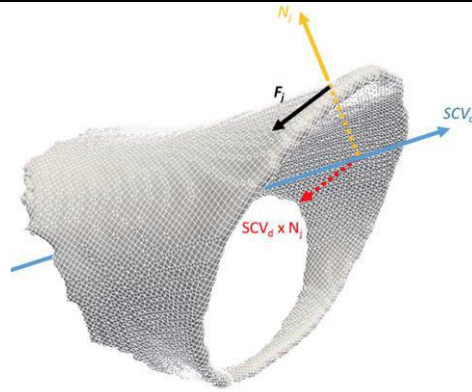


Figure 37. Method for fiber direction calculation. SCV_d is the defined directive, N_j is the normal associated to each element and F_j is the orientation of the fiber calculated with the cross-product $SCV_d \times N_j$ [28].

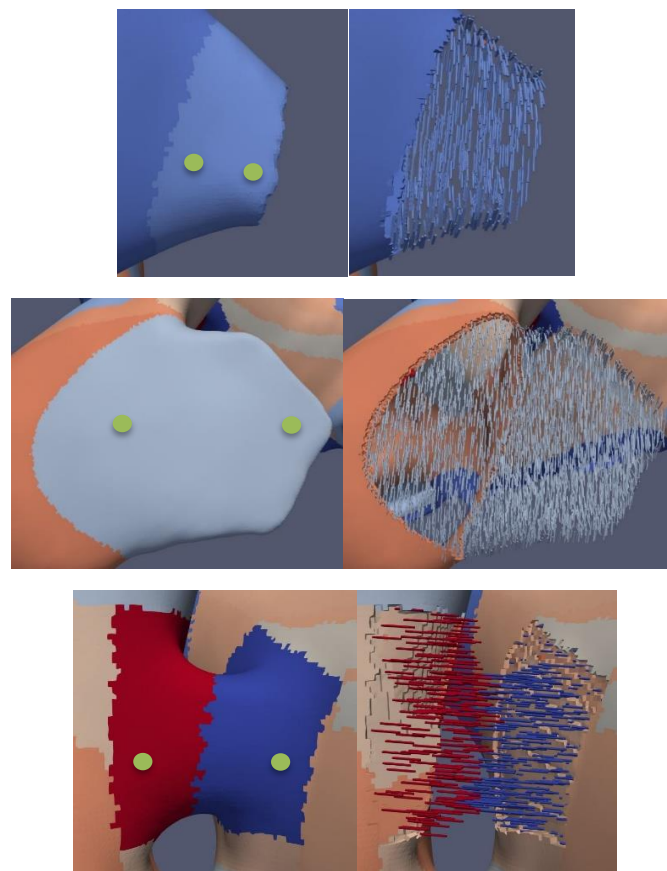


Figure 38. Fiber direction definition for model 1403865 for the left inferior PV (LIPV) (top), RAA (middle), and BB (bottom).

3.7. ELECTROPHYSIOLOGICAL SIMULATIONS

3.7.1. Ionic models

The mathematical model used was the ionic model developed by Courtemanche et al. [90] for simulating normal human atrial APs. This model was chosen because of it has a moderate

computational cost and a simple implementation. The ionic mechanisms controlling the behavior of the human atrial AP are poorly understood, however, a mathematical model of the atrial AP was created using data recorded from human atrial myocytes to reach specific formulations of the Ca^{2+} , K^+ , and Na^+ currents together with representations of pump, exchange, and background currents (see Figure 39). Marc Courtemanche, Rafael J. Ramirez and Stanley Nattel [90] were the responsables of developing the mathematical model so the model will be called CRN, that is based mostly on the guinea pig ventricular cell models by Luo and Rudy [115]. In Figure 39, a schematic representation of currents, pumps and exchangers included in the model can be observed. The cell contains three intracellular compartments: cytoplasm, sarcoplasmic reticulum (SR) release compartment, and SR uptake compartment.

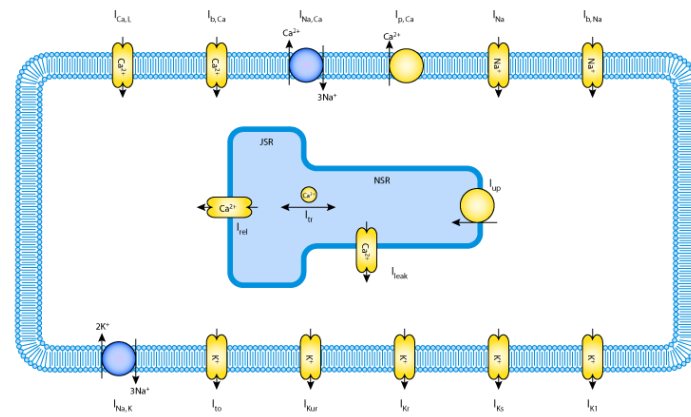


Figure 39. Schematic representation of the CRN ionic model [116]

The CRN model contains 21 variables and formulations for 12 transmembrane currents and for the intracellular calcium dynamics. The total ionic current can be obtained from the sum of all the potassium, calcium, and sodium currents and is expressed in the following equation:

$$I_{ion} = I_{Na} + I_{K1} + I_{to} + I_{Kur} + I_{Kr} + I_{Ks} + I_{Ca,L} + I_{Ca,T} + I_{Ca} + I_{Na,K} + I_{NaCa} + I_{b,Na} + I_{b,Ca} \quad (4)$$

The CRN model is stable with a resting membrane potential of approximately -81 mV and intracellular concentrations at rest of $[Ca^{2+}]_i = 0.1 \mu M$, $[Na^+]_i = 11.2 \text{ mM}$ and $[K^+]_i = 139.0 \text{ mM}$ [90]. Although, the authors didn't provide data about the variations in these concentrations when simulating the cells. These changes could alter the AP morphology and duration, so a stabilization of these concentrations needs to be performed. The electrical activity of an atrial myocyte was simulated during 1 minute with a basic cycle length (BCL) of 500 ms with a stimulus of 2 nA in amplitude and 2 ms in duration. For performing this stabilization, we worked with the software Cellular Open Resource (COR), developed at Oxford University.

The different regions of the atria have different electrophysiological behavior, so in order to match this atrial heterogeneity the ionic models needed to be adjusted. The maximum conductance of the three main ionic currents (I_{to} , I_{CaL} and I_{Kr}) was modified for the ionic models of each different region based on experimental data about AP morphology and duration, as described in [5], [117]–[119]. This modification consisted in applying multiplicative factors to the default values in the CRN model, increasing or decreasing the channel conductance, following the relative regional variations of the experimental APDs ($_{APD90}$ and $_{APD95}$). The result was

nine different cellular models for the regions RA/PM, LA, CT/BBRA, BBLA, PV, MVR, TVR, RAA and LAA. In Table 6, the relative conductances applied to each model can be observed.

	RA/PM	CT/BBRA	TVR	RAA	LA	BBLA	MVR	LAA	PV
g _{to} max	1.00	1.00	1.00	0.68	1.00	1.00	1.00	0.68	1.00
g _{CaL} max	1.00	1.67	0.67	1.00	1.00	1.67	0.67	1.00	1.00
g _{Kr} max	1.00	1.00	1.53	1.00	1.60	1.60	2.44	1.60	2.20

Table 6. Relative conductances with respect to the g_{max} in the original CRN model for the different anatomical regions.

Simulations of 1 minute with the modified control models were performed at a BCL of 1000 ms, and APs were recorded so the atrial heterogeneity in AP morphology and duration can be noticed. In Figure 40, a plot of the APs for the 9 different ionic models is shown, with the BBRA/CTS region having the longest APD and the MVR region the shortest.

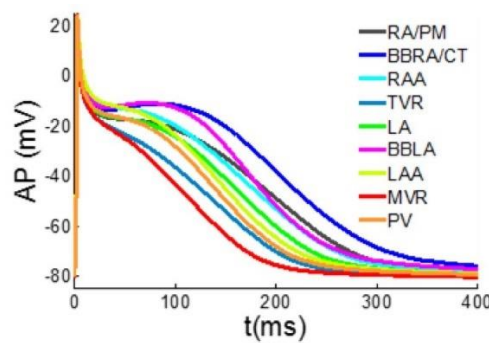


Figure 40. Action potential (AP) plots for each atrial region of the CRN control model

Since cAF was simulated, we needed to work with models that include the atrial electrical remodeling characteristic of cAF. Again, modifications in the maximum conductances of different currents (I_{to}, I_{CaL}, I_{K1}, I_{Kur}, and I_{Ks}) had to be made based in experimental studies [69]–[72], [76], [78], [80] and in concordance with other computational research works [87], [93], [95], [118], [120], [121]. In Table 7, the factors varying the different channels are shown with the remodeling being different in RA and LA. These changes were applied to the already modified CRN models corresponding to the atrial heterogeneity detailed above in Table 6.

	RA/PM	CTS/BBRA	TVR	RAA	LA	BBLA	MVR	LAA	PV	Reference
I _{to}		0.55					0.25			[69]
I _{CaL}		0.35					0.35			[70],[76]
I _{K1}		2.00					2.00			[71], [76], [78]
I _{Kur}		0.40					0.55			[69]
I _{Ks}		2.50					2.00			[69]

Table 7. Remodeling coefficients applied to the modified CRN models for each region.

In Figure 41, we can see the APs for the different regions after applying the cAF remodeling [75]. APD shortening was around 50%, as stated in experimental observations [70].

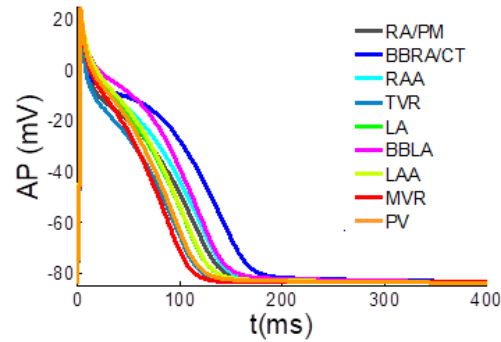


Figure 41. APs for the remodeled ionic models for each atrial region. [75]

3.7.2. Atrial simulations

The electrophysiological simulations were performed with the software Elvira [122], with a temporal resolution of 0.01 ms. This software uses a FEM solver, together with the monodomain formalism detailed in section 1.5.3, with the reactive term being the set of equations that define the ionic CRN model detailed in the previous section. Elvira solves the system of equations and provides a set of .bin files, where the data about the potential for each time instant is present. A postprocessing of these files is done for retrieving files that can be visualized in Paraview (files .case, .geo and .ens).

3.7.2.1. Generation of Elvira files

The model data was provided in a series of .dat files, a generic format for data text files. For converting the information included in our final .vtk volume model into these .dat files, a Matlab interface written by my tutor Laura Martinez, was utilized. The material conductivities and anisotropy properties had to be assigned, and the stimulation protocol needed to be defined. These generated several .dat files: ELEMENTS.dat and NODES.dat with the information about the elements and nodes respectively, PROP_ELEM and PROP_NOD with the properties of these elements and nodes, MATERIALS.dat, STIMULUS.dat, and MAIN.dat, which was run.

3.7.2.2. Simulation process

A protocol of stimulation needed to be established for simulating the propagation of the AP in the atrial tissue. Since the objective is to simulate an atrial fibrillation and induce reentries, the protocol implemented is the S1-S2 standard [79].

First the normal behavior of the atria was simulated by applying stimulation in the SAN region, achieving a sinus activity (S1) and a control propagation. Since each patient's atrial 3D model has a different size and anatomy, the conductivities and anisotropy of the different regions needed to be adjusted so the activation sequences of the different anatomical regions match the experimental values presented by Lemery et al [123]. First, the patient 3196630 atrial model was used for adjusting the conductivities and anisotropy in the control case. The values obtained for this model, seen in Table 8, worked out also for patient 3014094, and the control simulation's activation sequences were in the range established by Lemery et al. [123] as it will be shown in the results section. Although, these values did not perform well with the remaining atrial models, so a new set of parameters was defined for the patient 3023001 and 1403865 patient

models, which can be observed in Table 8. Simulations of 150 ms were performed with the stimulus S1 in the SAN region with an amplitude of 2 nA during 2 ms at the time instant 0 ms.

Material region	3196630 & 3014094		3023001 & 1403865	
	Conductivity (S/cm)	Anisotropy	Conductivity (S/cm)	Anisotropy
RA	0.00615	0.35	0.0045	0.35
CTS	0.012	0.15	0.013	0.15
PV	0.003	0.5	0.002	0.5
BB_PM	0.01125	0.15	0.011	0.15
ISTMO	0.004	1	0.004	1
SAN	0.00104	1	0.000936	1
FO	0	1	0	1
CS	0.019	0.6	0.019	0.5
LA	0.00615	0.35	0.0045	0.35
FO ring	0.01125	0.15	0.010125	0.15
BBLA_FO	0.009	0.15	0.0085	0.15

Table 8. Conductivity and anisotropy values for the electrophysiological simulations performed in control for each atrial region.

Then, the S1 stimulation protocol was implemented but with the cAF remodeled ionic models for obtaining the cAF control simulation. The values for conductivity were reduced by 15% with respect to the ones used in the control case, shown in Table 8. Simulations were runned during 250 ms with the stimulus S1 in the SAN region with an amplitude of 2 nA during 2 ms at the time instant 0 ms. Restart files were saved at the time instants 150, 200, and 250 ms, so that the simulation is not repeated and for the S2 stimulation protocol the simulation can start at one of those points.

Finally, ectopic foci were applied at the LPVs in order to induce reentries. S2 corresponds with the activity of the stimulus administered in between the LPVs. By looking in Paraview at the cAF control simulation aforementioned, we decided the region and time instant where the ectopic focus would be applied. 6 stimulation pulses were given with an amplitude of 2 nA, and a duration of 2 ms with a BCL of 130 ms, and the simulation was performed during 2 s for checking if reentrant activity continued after the ectopic foci.

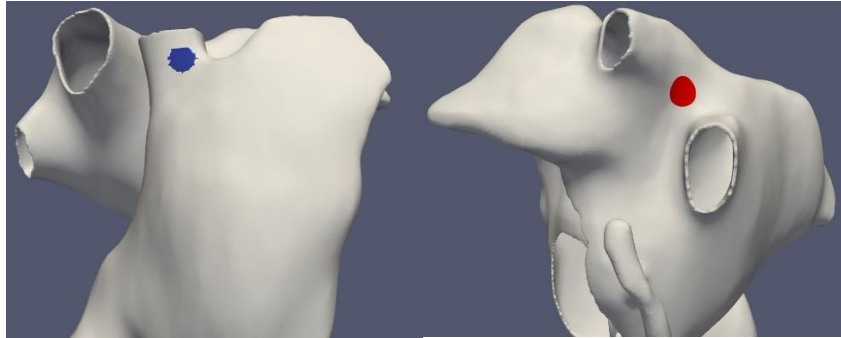


Figure 42. Protocol of stimulation S1-S2. Regions defined for model 1403865.

3.7.3. Torso simulations

After doing the simulations on the 3D atrial models, we performed the electrical propagation of APs of the atria along the torso model. The simulations were performed in Matlab by an approximation of the bidomain formalism, where the extracellular membrane potential is calculated on every node on the torso model from the intracellular membrane potential from the atria simulation. More details about the bidomain model used can be found in the article published by Martinez [124]. A series of Matlab codes were run for performing the torso simulation. The potential at the surface of the torso was the objective, so in Paraview the nodes in the surface were selected, extracted, and saved as .vtk and .csv files. The first two codes Prepare_Torso_elements_1.m and prepare_files_2 were used for preparing the necessary files for running the torso simulation. With the obtained files, the code run_torso3D_3.m was run in the cluster for obtaining the surface signal at every node for the duration of the atria simulation. Conductivities had to be assigned to each region of the torso, and they can be seen in Table 9. The values and references of the experimental conductivities that we based are choice on, are also shown. The conductivity values were the same as the ones used by Ferrer [28], except for the torso, and the kidneys which were not included in the torso model by Ferrer. The torso conductivity was reduced to 2.00, which is justified by supposing an individual with 60% of muscle and 40% of fat, and calculating the conductivity for the torso from the experimental conductivities of muscle and fat given by Keller et al. [125] The result of the simulation will be a .dat file with the potential of every node in the surface for each time instant. This procedure was done for the control and arrhythmia simulations.

	Model conductivities (mS/cm)	Experimental conductivities (mS/cm)	Reference
Ventricles	4.590	5.00	[126]
		0.60-4.00	[127]
		0.537-4.83	[125]
Liver	0.277	0.277-2.00	[125]
		0.277	[128]
Bones	0.200	0.05-0.60	[125]
		0.2	[128]
Lungs	0.389	0.39	[125], [128]
Blood	7.000	0.435-10	[125]
		7	[128]
Torso	2.000	2.39	[129]
		2.20	[126]
		Muscle: 3.3 Fat: 0.12	[125]
Kidneys	0.544	0.544	[128]
		0.544-9	[125]

Table 9. Model and experimental tissue conductivities for the torso model

We decided to filter the surface signals with a Butterworth bandpass filter between 0.5 and 30 Hz. Tereshchenko and Josephson indicate that the content of the P-wave is characterized by 5-30 Hz frequencies [130]. Other studies say that the typically used cutoff for filtering ECG signal clinically is 40 Hz [131], [132], whereas others say that the spectral content of a normal P-wave is below 20 Hz [133], [134]. By opening the torso surface model in Paraview, the precordial and standard leads were located and a node in the surface model was obtained for each lead. The potential at the standard, augmented, and precordial leads was plotted in Matlab.

A body surface potential map (BSPM) was generated from the filtered surface signals. A series of Matlab codes were run for retrieving the appropriate files for visualizing the BSPM in Paraview. The codes used were: `genera_CASE_BSPM.m`, `genera_cas_sup.m`, `genera_ficherosVAR_BSPM.m`, and `genera_geo_supTorso.m`.

3.8. SUMMARY OF THE METHODS

The methodology applied in this work is now summarized in this last section. In Figure 43, the pipeline of the different steps is shown, including the software used for every task. The acquisition of CT scans was done by personnel of Hospital Politécnico y Universitario La Fe with the Philips iCT 256 CT scanner. Segmentation of the desired structures was done with Seg3D. Conditioning of the surface models of the atria and torso organs was performed in Paraview and

Blender. Matlab was used for dividing the atrial regions, and adding fiber direction, and Paraview was utilized for visualization of the surface and volume models, as well as the electrophysiological simulations. The software MeshGems was used for meshing the atria, while for the torso Tetgens was adopted. Regarding the electrophysiological simulations of the generated atrial models, the software Elvira was applied, meanwhile, the torso simulations were performed in Matlab.

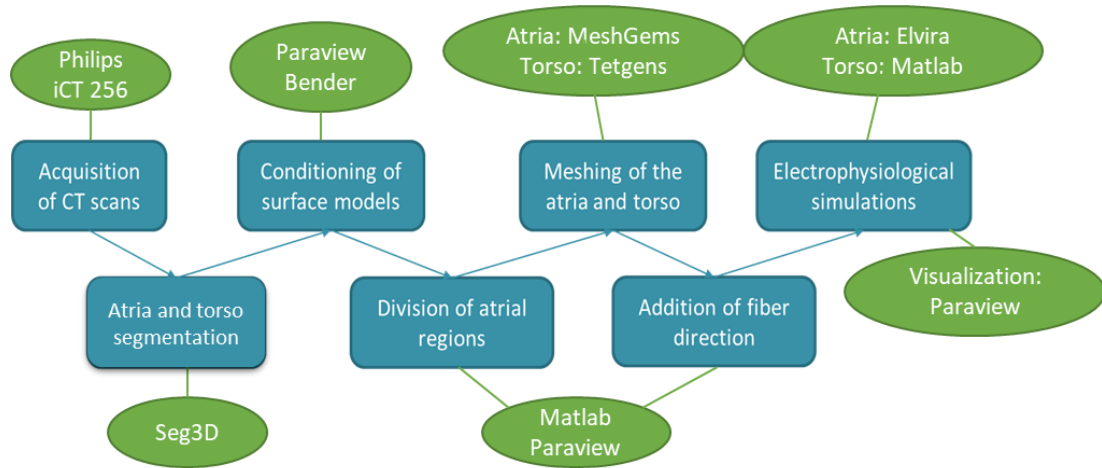


Figure 43. Pipeline of the methodology applied in this work including the software used at each step (green)

CHAPTER 4. RESULTS

In this chapter the resulting atria and torso models obtained after following the methodology detailed in Chapter 3 are shown, and the simulations performed with them are presented. First, the surface geometries are introduced, followed by the final volume models. Regarding the cardiac electrophysiological simulations, the control cases are first displayed, and later the simulations done with cAF remodeling in pursue of inducing reentries are shown.

4.1. SURFACE GEOMETRIES

4.1.1. RA-LA and ORGANID labelled surface models

After segmenting the atria, smoothening and conditioning of the models and division in different atrial regions, the final labelled surface meshes were achieved. A surface mesh was obtained for each patient, with both nodes and cells having the properties of RA-LA and ORGANID. These surface meshes were formed by triangular elements, so each element was composed of 3 nodes. The number of cells and nodes for each of them can be observed in Table 4. It can be noticed how for the atria from patient ID 1403865 the number of cells and points in the surface mesh was considerably lower. This was due to the origin of the images for segmentation, which came from a full torso CT instead of a cardiac CT. Therefore, the resolution of the images was much lower and so did the resulting mesh. Mesh with patient ID 3196630 was the one with the greatest number of points and cells, which makes sense as this was the patient with the biggest atria (see Table 4).

Patient ID	Nº of cells (elements)	Nº of points (nodes)
1403865	308,574	154,269
3014094	1,290,506	645,235
3023001	1,058,031	529,004
3196630	1,443,492	721,726

Table 10. Nº of cells and points for each of the surface atrial meshes

In Figure 44, we can observe the 4 surface meshes labelled in RA (blue) and LA (red). This separation was essential for applying the designed atrial region separation algorithm in order to divide the atria in the necessary detailed regions.

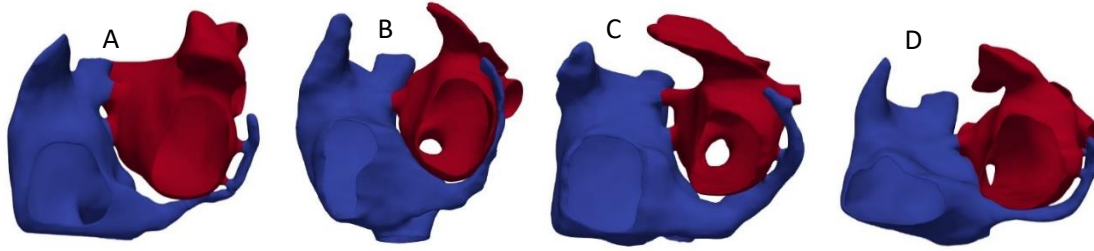


Figure 44. Surface meshes divided into RA (blue) and LA (red) for patient IDs 1403865 (A), 3014094 (B), 3023001 (C), and 3196630 (D).

After applying the developed algorithm for atrial regions separation, new surface meshes with the property of ORGANID were obtained. The 45 different regions established for each mesh are shown in Figure 45. Those 45 regions, needed to introduce later the fibers orientation, were: SAN, CTS, BB, right atrium BB (BB_RA), 3 left atrium BB regions (BB_EXT_1, BB_EXT_2, BB_EXT_3), 2 unions between BB and LFO (BBR_FO_Union, BBL_FO_Union), FO, LFO, IB, TV, RAS, RLW, RAA, IST, SCV, ICV, 9 PM, LSW, LAS, LAA, LPW, MV, RPV, right superior PV (RSPV), right inferior PV (RIPV), right PV union (RPVu), LPV, left superior PV (LSPV), left inferior PV (LIPV), left PV union (LPVu), low CS (CSlow), medium CS (CSmed), and CS connections (CSc).

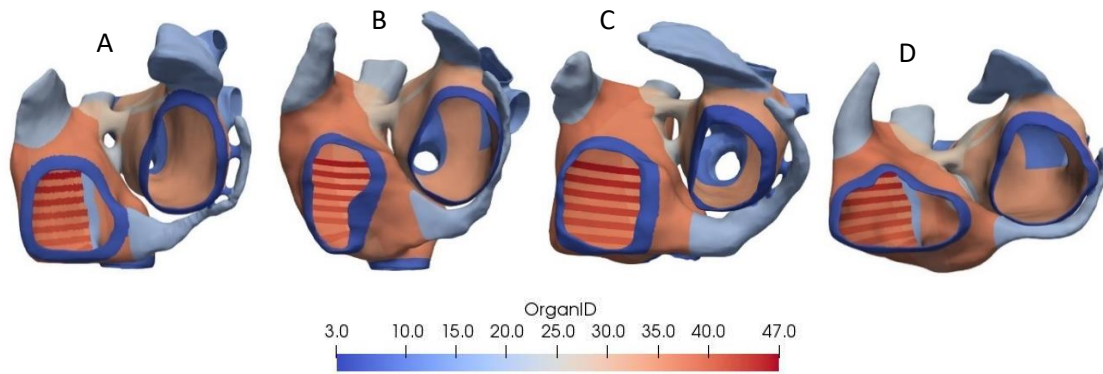


Figure 45. Surface meshes divided in the 45 ORGANID regions for patient ID 1403865 (A), 3014094 (B), 3023001 (C) and 3196630 (D).

4.1.2. Torso model

For patient IDs 1403865, the principal organs (atria, ventricles, liver, bones, lungs, kidneys, blood, and torso skin) were segmented from the torso CT, yielding as a result the organs isosurfaces. They were smoothed, conditioned, and remeshed using the software Blender for achieving triangular surfaces with uniformity and appropriate density of elements. It was essential that there were no intersections between the organ surfaces and no mesh holes, in order to be able to mesh the torso with all the organs. In Figure 46, the segmented surfaces used for meshing the volumetric torso model are shown.

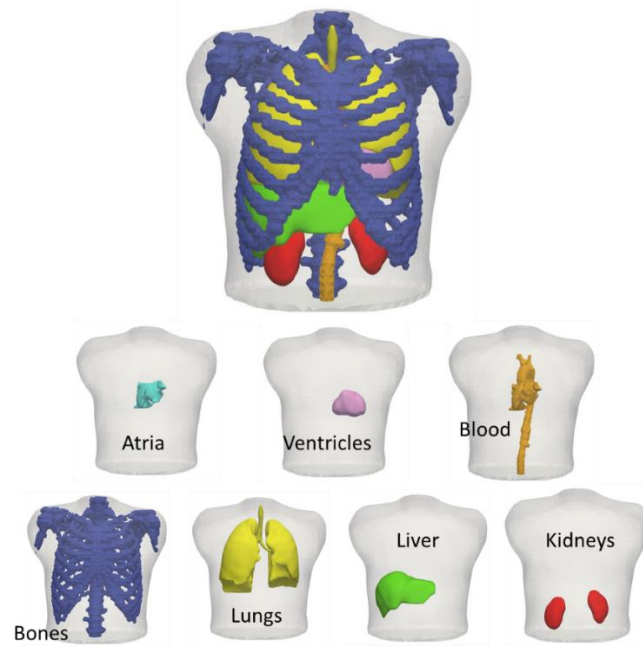


Figure 46. Smoothened surfaces of the organs in the torso model segmented from patient with ID 1403865. Included organs are: atria (light blue), ventricles (pink), blood (orange), bones (dark blue), lungs (yellow), liver (green), kidneys (red), and torso surface (transparent white)

4.2. VOLUME GEOMETRIES

4.2.1. Atrial models

4.2.1.1. Mesh quality analysis

Volumetric meshes were obtained after meshing the atrial surfaces on MeshGems for the 4 case studies presented in this work. The resulting volumetric meshes were formed by hexahedral elements. In Table 11, the number of cells (hexahedral elements) and points (nodes) for each of the patient's ID is shown. Accordingly to the surface meshes, the volumetric mesh with the least number of cells and points is still the one from patient ID 1403865, but the values in this case are much closer to the rest of the meshes, compared to what happened for the surface meshes (Table 10). This fact was due to the spatial resolution imposed during the volumetric meshing process, which was performed with the same conditions for the 4 patients. Therefore, these parameters depend merely on the anatomy and size of the organs.

Patient ID	Nº of cells (elements)	Nº of points (nodes)
1403865	897,292	1,144,947
3014094	1,143,588	1,472,404
3023001	902,537	1,151,552
3196630	1,243,459	1,550,287

Table 11. Nº of cells (hexahedral elements) and points (nodes) for the volumetric meshes of the 4 atria segmented.

For avoiding problems during the simulations of electrical propagation, it is necessary that the mesh fulfills some minimum requirements. A quality analysis was performed for assuring the wellness of the volumetric mesh. Since MeshGems adapted the elements to respect the anatomy of the given surface mesh, there was the possibility that some of these elements were generated in an irregular manner. MeshGems provided a data file with the final mesh statistics, which are summarized in Table 12. From this information, it can be deduced that, in general, the surface was slightly reduced after meshing, with the ratio out/in being around 0.98. The percentage of invalid elements is 0% for all the cases, so the obtained meshes had an adequate quality to perform simulations. For patient ID 3014094 and 3023001 there was a very slight percentage of bad elements that can be considered negligible. The percentage of good elements for all the cases is above 80%, being this a good indicator of the quality of our meshes.

Patient ID	1403865	3014094	3023001	3196630
Input surface (cm^2)	549.369	703.766	550.469	666.416
Output surface (cm^2)	542.111	688.184	542.254	659.218
Ratio out/in	0.98679	0.977859	0.985076	0.989199
Invalid elements (%)	0	0	0	0
Bad elements (%)	0	0.000347	0.000332	0
Average elements (%)	18.421874	19.247982	18.838784	15.306873
Good elements (%)	81.578126	80.751671	81.160883	84.693127

Table 12. Meshing statistics provided by MeshGems for the 4 atrial volumetric meshes

The size of the hexahedral elements was evaluated to make sure the distribution is uniform and there are not elements that are too small or too big. An ununiform element size distribution could affect the propagation of the electrical impulses since the distances between points would be too irregular. The length of the element edges was also given by the software MeshGems after the meshing process. When meshing, it was given as an input that the element size should be constricted between 0.04 cm and 0.04 cm, so the program would try to build the mesh as uniform as possible, and with the size being close to that value. As observed in Figure 47, the

element size distribution shows that the majority of elements is between 0.02 cm and 0.04 cm for the 4 atria.

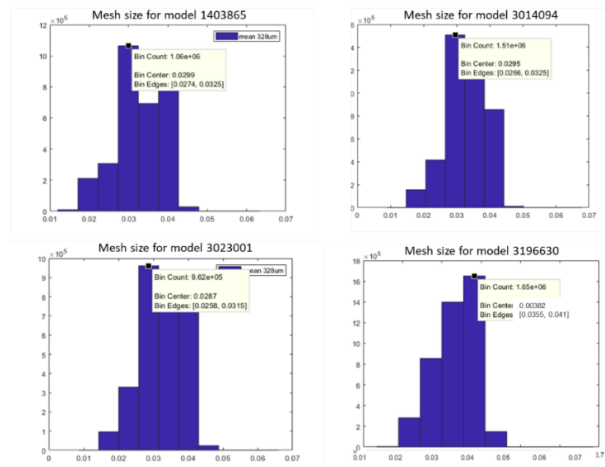


Figure 47. Histogram of the mesh size for the 4 volumetric atrial meshes (x axis: size of the element; y axis: number of elements).

The Scaled Jacobian is a parameter indicative of the degree of deformation of the elements, and it is one of the most important regarding the quality of the volumetric mesh since if it presents negative values, the numerical problem will not be solved. It represents the minimum value of the determinant of the Jacobian matrix calculated in each point, divided by the length of the corresponding edges. In Figure 48 the analysis of the Scaled Jacobian for each mesh is depicted. And, as observed, all the elements in the 4 meshes fulfill the requirement of a positive value for the Scaled Jacobian.

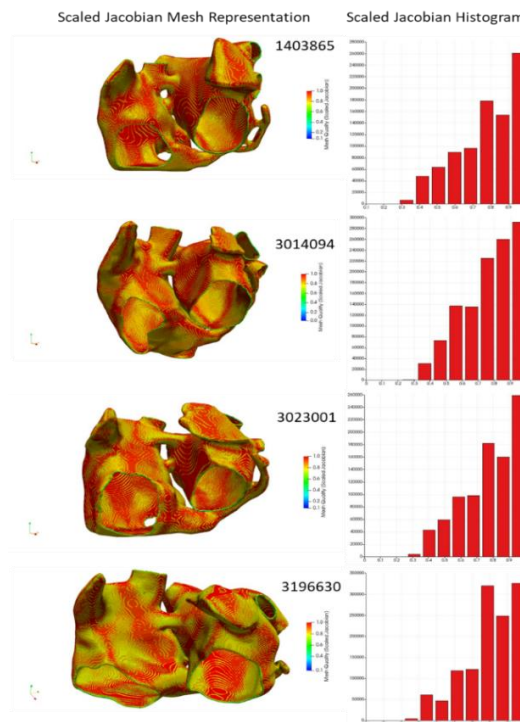


Figure 48. Analysis of the Scaled Jacobian of the atrial volumetric meshes. Left: Scaled Jacobian values color-coded on the mesh, right: histogram (x axis: Scaled Jacobian value; y axis: number of elements).

4.2.1.2. Final atrial volume models

Once obtained the volumetric meshes, the ORGANID property for both, points and cells, had to be defined. For this purpose, we mapped the ORGANID property from the surface meshes into the volumetric meshes. As previously explained in detail in the methods section, some modifications were made. The number of ORGANID regions went from 45 to 48, since the BB was divided into 4: right interior BB (RIBB), left interior BB (LIBB), right exterior BB (REBB), and left exterior BB (LEBB). The ORGANID property was essential for defining the ionic model, material, and fiber direction in each atrial region, all three properties needed for the electrophysiological simulations. As a result, we obtained the realistic and highly detailed atrial models shown in Figures 49-51.

The ionic models were the only property defined in the points, instead of the cells, since the ionic model equations are solved at each point (node) in Elvira. The differentiated 9 ionic model, as in previous computational works [124]: RA/PM, CT/BBRA, TVR, RAA, LA, LAA, PV, MVR, and BBLA. Those regions can be visualized in Figure 49. The resulting APs from each of the regions, corresponding to the different variations of the ionic model detailed in the Methods, are the ones depicted in Figure 41.

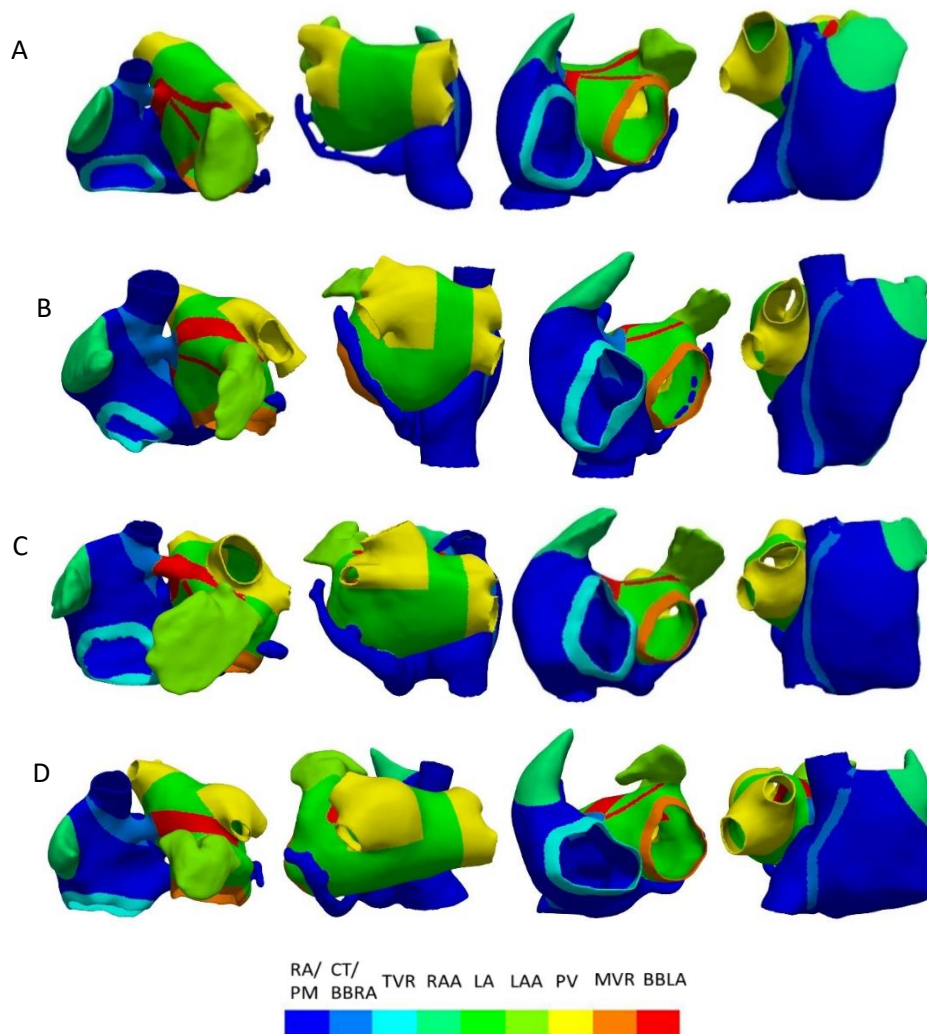


Figure 49. Ionic model property in the 3D atrial models por patient ID 1403865 (A), 3014094 (B), 3023001 (C) and 3196630 (D).

The material property defined the conductivity and anisotropy for each atrial region. As observed in Figure 50, 11 different regions based on their tissue properties were created for all the atrial models. These material regions were: RA, CTS, PV, BBRA/PM, ISTMO, SAN, FO, CS, LA, INS, BBLA/FO.

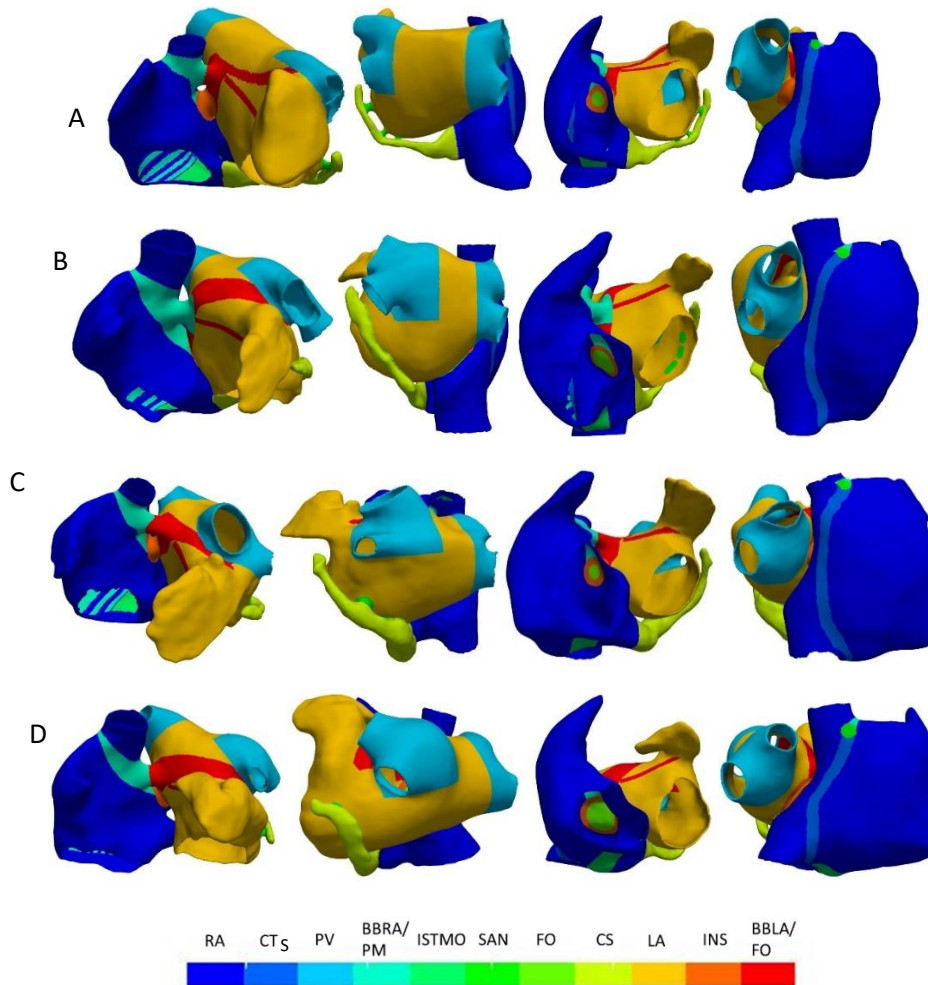


Figure 50. Material property for the 3D atrial models corresponding to patient ID 1403865 (A), 3014094 (B), 3023001 (C) and 3196630 (D).

The last step in the creation of the atrial models for performing the electrophysiological simulations was the introduction of the fiber direction for each region. This property was extremely important since it dictates the propagation of the electrical wavefront along the atria, so it had to be as realistic as possible. As mentioned in the Methods, we were not provided with histological information about the patients (hearts were not explanted), so fiber orientation was defined based on histological observations [6], similarly to prior computational works [5], [28]. In Figure 51, a representation of the fibers orientation for the 4 models, color-coded by ORGANID, is shown. As observed, fibers direction are in accordance with histological patterns. Since 8 out of the 9 PM have the same fiber direction, in reality there is a total of 41 regions that have different material properties, ionic models, and fiber direction.

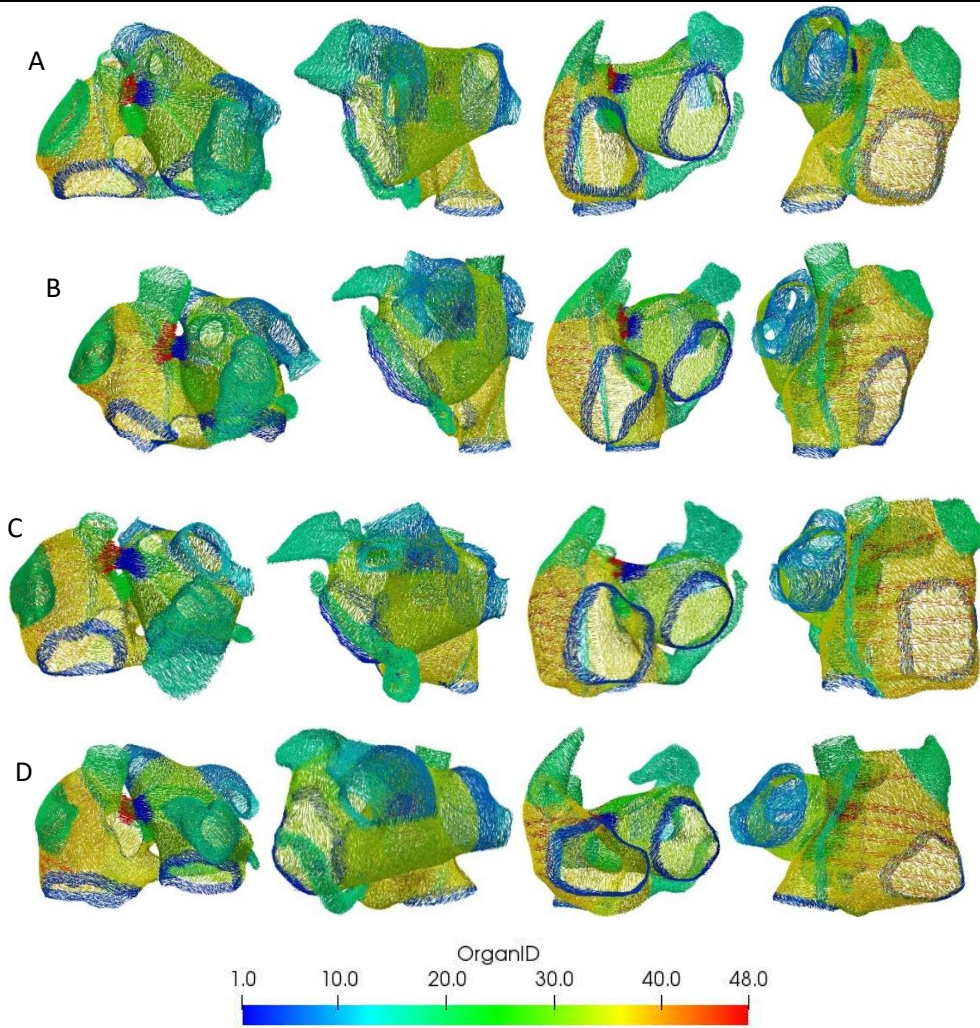
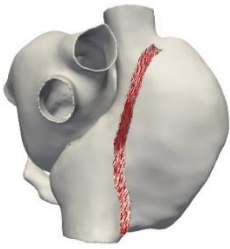
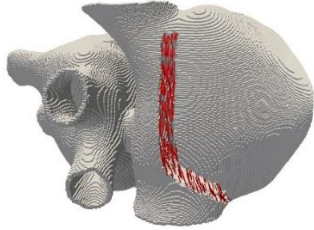
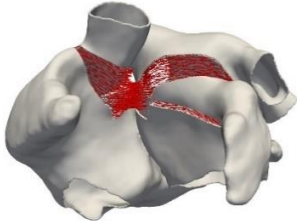
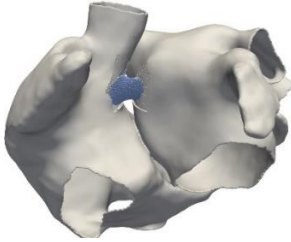
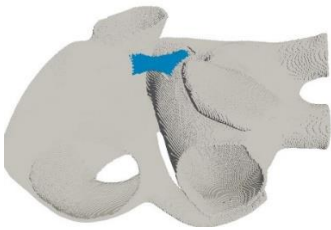
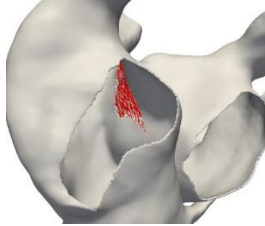
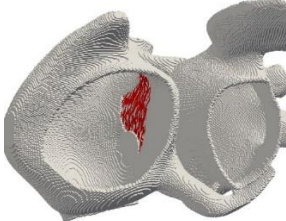
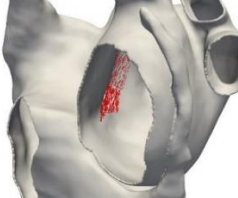
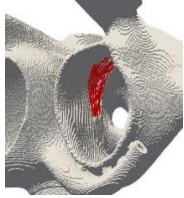
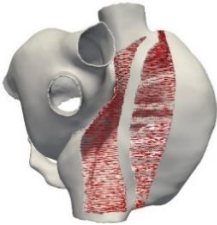
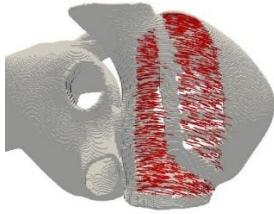
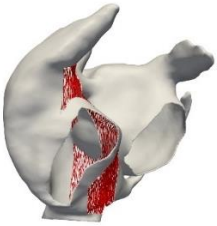
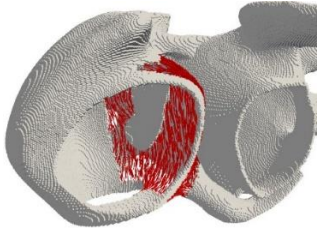
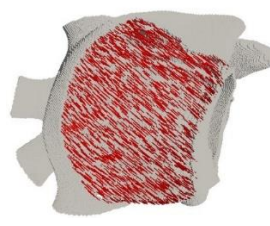
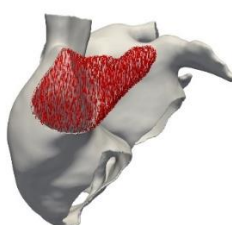
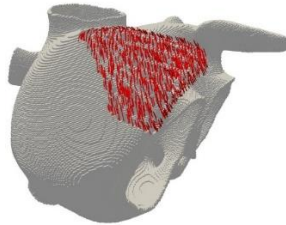
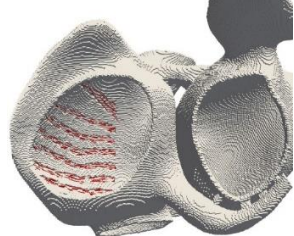
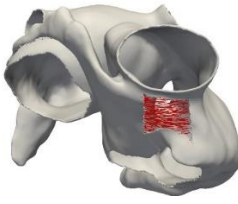
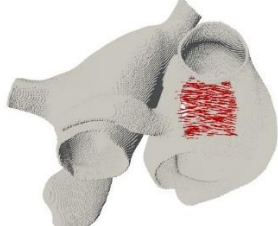
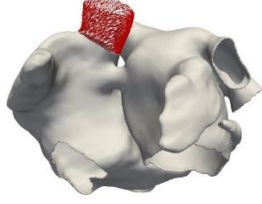
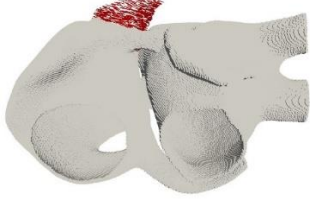
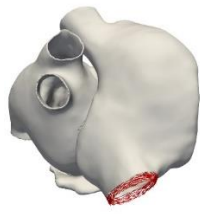
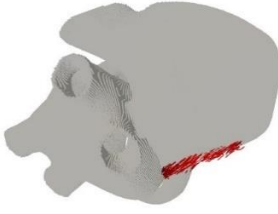
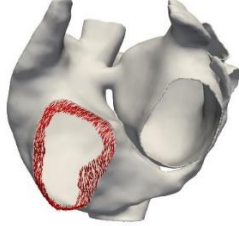
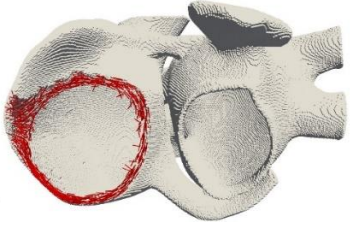


Figure 51. Fiber direction in the 3D atrial models, color-coded by ORGANID, for patient ID 1403865 (A), 3014094 (B), 3023001 (C) and 3196630 (D).

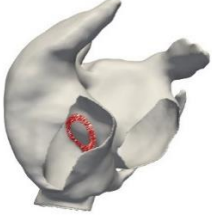
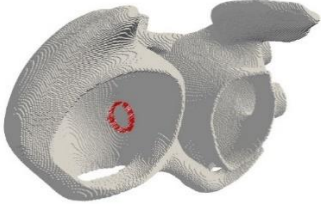
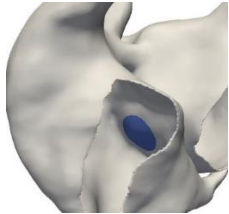
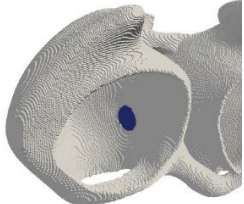
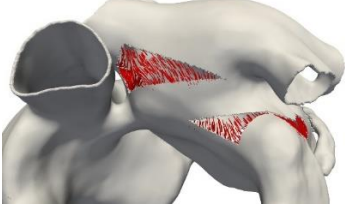
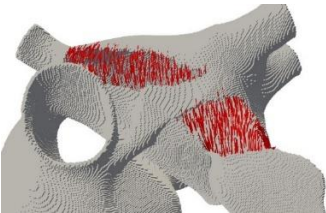
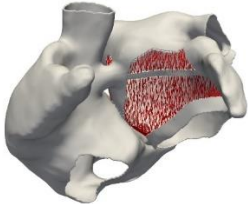
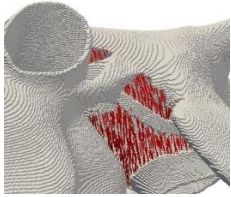
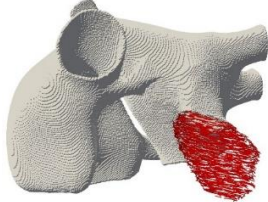
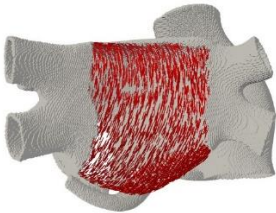
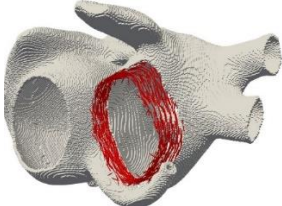
In order to further detail fibers orientation obtained for our models, in Table 13 fibers corresponding to patient ID 3014094 model are shown, as an example for comparison with the model created by Ferrer [28] and validation of our results. As depicted in Figure 51, the rest of the generated models in this work shown similar fiber directions to model 3014094.

Nº	REGION	Patient ID 3014094	Ferrer [28]
1	SAN		

2	CTS		
3	BBR BBL		
	RIBB LIBB (insulating)		
4	BBRA_FO		
5	BBLA_FO		
6	IB		
7	RAS		

8	RLW		
9	RAA		
10	PM		
11	IST		
12	SCV		
13	ICV		
14	TV		

Design and development of a methodology for the creation of personalized anatomical and electrophysiological models of the human atria and torso

15	LFO		
15	FO (insulating)		
16	LSW		
17	LAS		
18	LAA		
19	LPW		
20	MV		

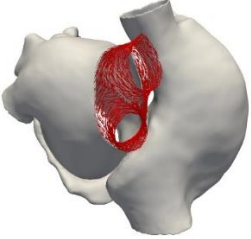
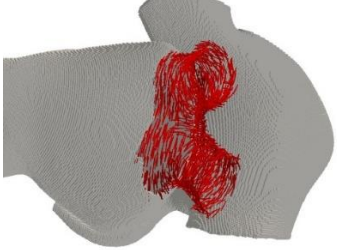
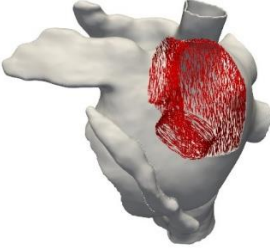
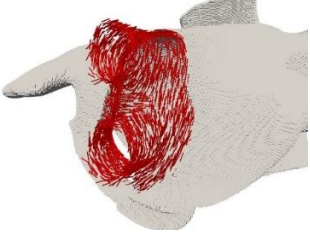
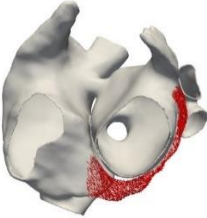
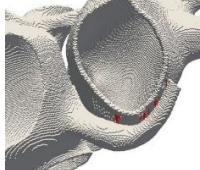
21	RPV		
22	LPV		
23	CS		
24	CS (Unions)		

Table 13. Detailed fiber direction for each anatomical region for the model with patient ID 3014094, compared to the fiber orientation presented by Ferrer [28].

4.2.2. Torso model

4.2.2.1. Mesh quality

The volumetric torso model was obtained after meshing from the surfaces of all the organs in Tetgen. The resulting volumetric model was composed by tetrahedral elements, unlike the atrial models, which were formed by hexahedral elements. The generated torso model is made up by 3,719,113 cells and 593,607 points. A mesh quality analysis was also performed for the volumetric torso model. The element size histogram can be seen in Figure 52. Most elements had the length of their edges in between 0 and 0.1 cm as it happened for the atrial model, although in this case there were a few elements with sizes up to 1 cm. The mesher introduced bigger elements in regions where a high spatial resolution was not needed, respecting the surfaces of the organs.

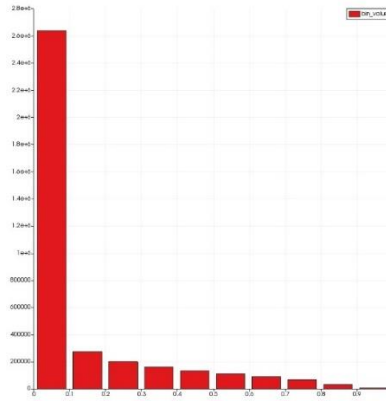


Figure 52. Histogram of the element size for the volumetric torso model

The Scaled Jacobian was also obtained for the volumetric torso model. As mentioned before, the Scaled Jacobian values must be positive, and as shown in the histogram in Figure 53, this requirement has been accomplished (the vast majority of the elements present a Scaled Jacobian value above 0.5).

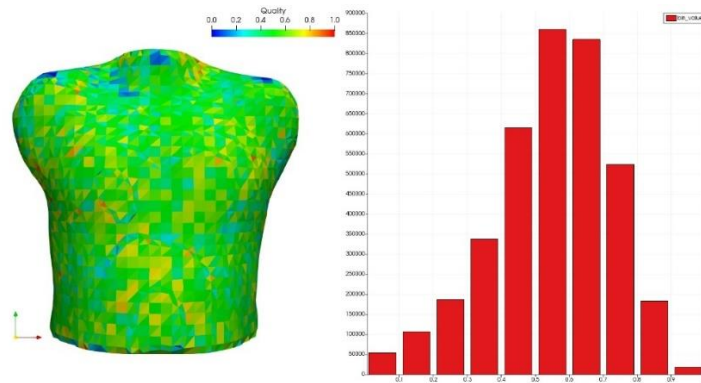


Figure 53. Analysis of the Scaled Jacobian of the torso volume model. Left: Scaled Jacobian color-coded on the mesh, right: histogram (x axis: Scaled Jacobian values; y axis: number of elements).

4.2.2.2. Torso volume model

The final tetrahedral torso mesh includes in detail the most relevant organs. The surface structures used for the meshing of the torso can be observed in Figure 46. The organs present in the torso model apart from the torso surface are: atria, ventricles, blood, bones, lungs, liver, and kidneys. In the torso model developed by Ferrer [28], the kidneys were not present. Other tissues like fat or skeletal muscles have not been included and are part of the general torso region. Although, for defining the conductivity of the general torso region, a tradeoff of 60% muscle and 40% fat was supposed for our model, and conductivity was defined based on this assumption. As mentioned, the mesh size varies significantly depending on the location in the torso, since the mesher maintained the input surface meshes and filled the rest. In Figure 54 the torso volume model can be seen with an axial and sagittal cut for looking at the interior. The difference in the mesh size can be observed, with the elements corresponding to the atria (dark blue) being the smallest, and making the surrounding ones also small, as it is the region that needs to have the highest definition.

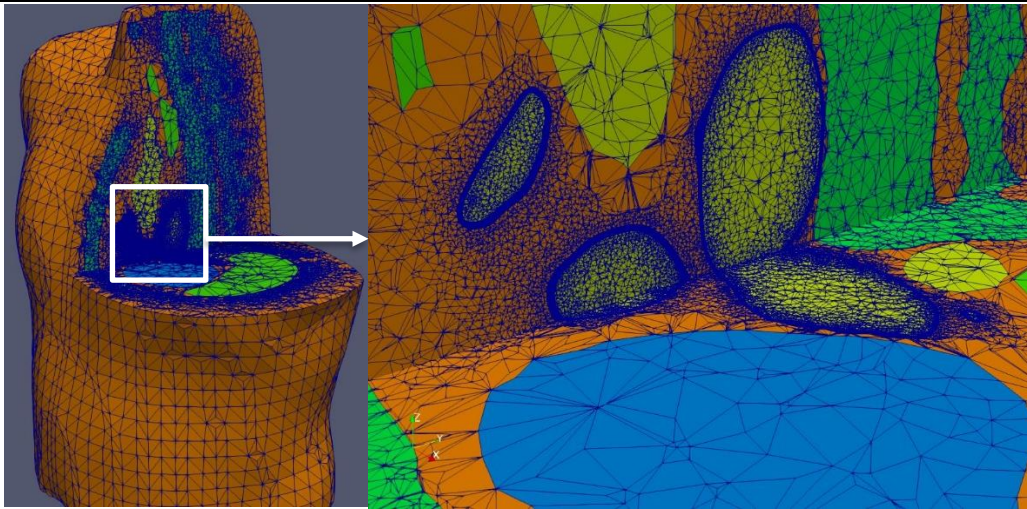


Figure 54. Final torso volume model. Atria (dark blue), blood (yellow), bone (light green), lungs (dark green), liver (blue), torso (orange)

4.3. CONTROL SIMULATIONS

4.3.1. Atrial simulations

The simulations of 150 ms duration performed with the different atrial models in control conditions were validated by comparing the activation times at different regions in the atria with the experimental values presented by Lemery et al [123]. In Figures 55, 56, 57, and 58 is shown the propagation of the cardiac electrical stimulus generated at the SAN along the atria for models corresponding to patient ID 1403865, 3014094, 3023001 and 3196630, respectively, compared to the experimental activation times. For the 4 models, activation times at every region were within the range of the experimental values. The activation times for our models are tending to the upper limit of the experimental range, since the slower we make the atria, the easier that it will be to induce reentry patterns. There is also a slight variation in the activation times between models due to the anatomical differences among them.

In general, for all the models generated in this work, the propagation pattern is in accordance with the experimental data. Depolarization starts at the SAN, where the autorhythmic cells generate the stimulus. Propagation of the electrical impulses is extended to the CTS, BBR, IB, and SCV, which are the next regions in getting depolarized. On one hand, activation goes down rapidly through the CTS towards the ICV, consequently stimulating the activation of the PM and IB. These activation pattern creates a triangular wavefront that spreads from the CTS to the TV through the RLW and RAA. Propagation arrives to the ICS and the ISTM, and spreads through the CS in direction towards the LA. The last activated region in the RA is the TV.

Activation is passed to the LA first through the BB and then through the LFO. The wavefront expands in the LA depolarizing the LSW and the regions around LAA, followed by the RPV, LPV, LPW, and the MV. Finally, the last activation occurs in the ILPV. Exceptionally, for model with patient ID 3023001 the last activation appeared at the tip of the CS, due to its high length.

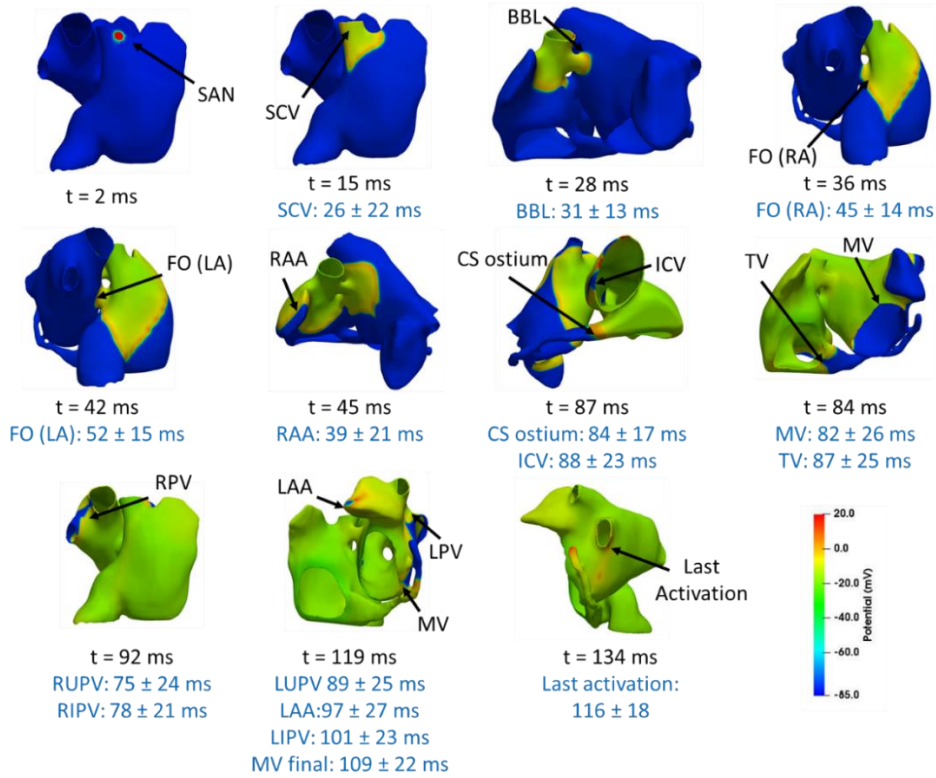


Figure 55. Activation sequence for the atrial model from patient 1403865. Comparison of the activation times of the simulation with the experimental ones provided by Lemery et al [123](blue).

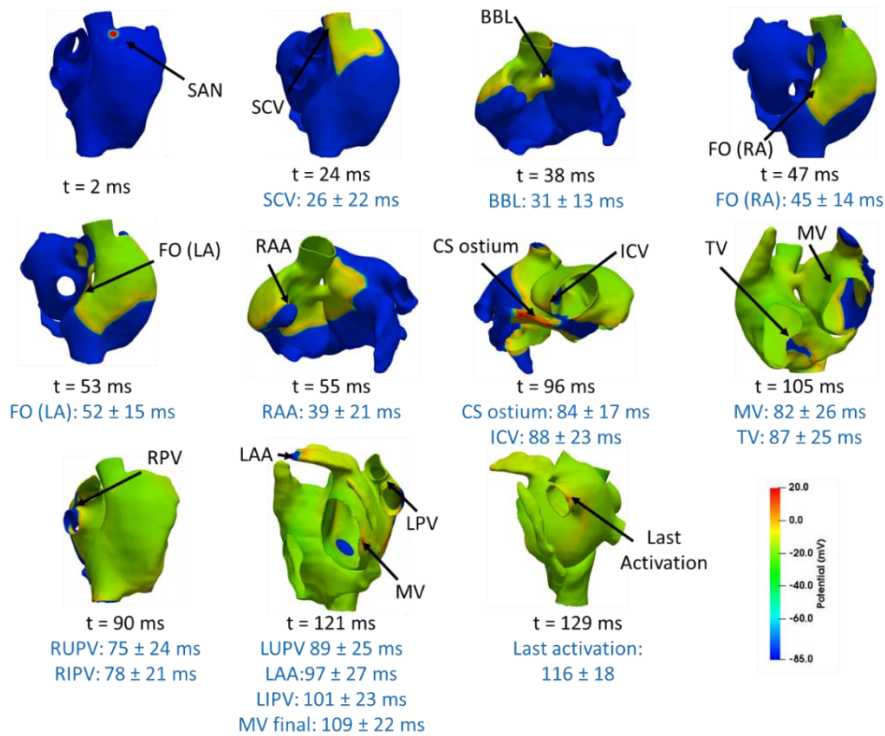


Figure 56. Activation sequence for the atrial model from patient 3014094. Comparison of the activation times of the simulation with the experimental ones provided by Lemery et al [123](blue).

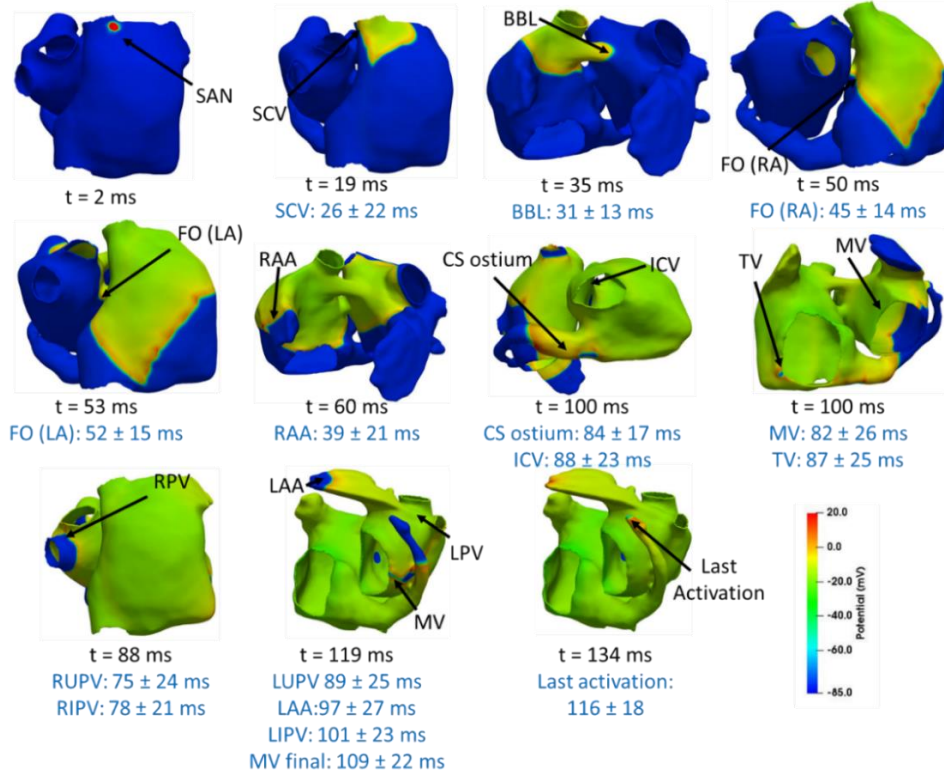


Figure 57. Activation sequence for the atrial model from patient 3023001. Comparison of the activation times of the simulation with the experimental ones provided by Lemery et al [123](blue).

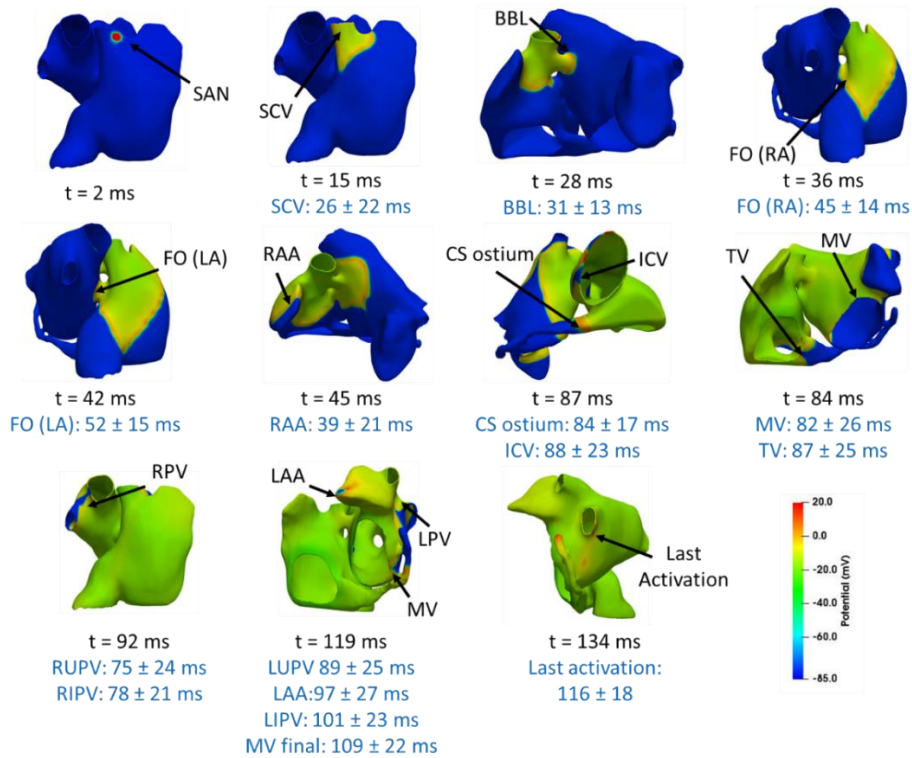


Figure 58. Activation sequence for the atrial model from patient 3196630. Comparison of the activation times of the simulation with the experimental ones provided by Lemery et al [123](blue).

4.3.2. Torso simulations

The control simulation performed in the atrial model for patient 1403865 was propagated along the torso model following the procedure detailed in section 3.7.3. Apart from validating the activation times of the different regions of the atria on the 3D atrial model as done in the previous section, the amplitude and duration of the P-waves obtained at the torso surface need to be validated. The ECG signals at the 12 leads in our torso model were obtained and validated with experimental results and with previous simulation studies. In Figure 59, the torso surface can be observed, together with the position of the 12 standard leads of the ECG and their respective signals. The amplitude and duration of the precordial leads are in accordance with the experimental data reported in the literature [135]. The signals morphology obtained at every lead are characteristic and in agreement with other recent computational studies. [136], [137]

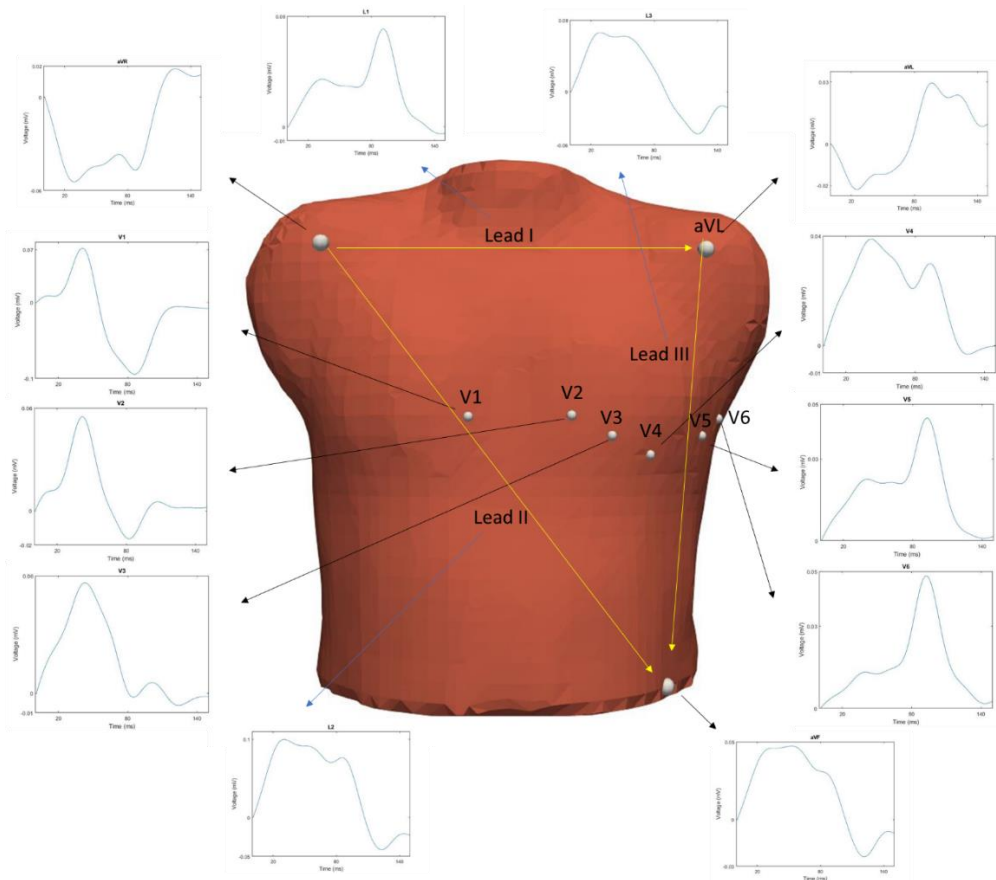


Figure 59. Location of the 12 leads in our torso model, showing the ECG signals obtained at each lead for the control simulation of patient 1403865

The electrical propagation on the front and back coronal views of the complete torso surface is shown in Figure 60 through the BSPM. Although not shown in the figure, during SAN depolarization ($t=0$ ms) the torso surface remains at a resting state (green). While the wavefront is spreading, in the upper torso low voltages start to appear as seen in $t=15$ ms in Figure 60, and then a visible dipole appears on the BSPM since around $t=30$ ms. The maximum potential achieved on the torso surface due to atrial depolarization was achieved at $t=45$ ms, where the

dipole it is most noticed, and when the atrial wavefront is travelling across the RLW and the RAS towards the upper side of the TV, and propagation passes to the LA through the BB as it can be observed in Figure 55. After this, the dipole shifts towards the left side of the torso in a downward direction as seen in $t=65$, and afterwards it rotates backwards, as seen in $t=85$, until it completely disappears. When the RA completely depolarized, the dipole disappears, and the torso surface comes back to the resting state at $t=115$ ms when most of the LA has also depolarized.

Comparing the signals obtained in the leads with the BSPM, we can see that the areas of negative potential in the surface (blue) correspond to negative values in the P-waves, which means that the wavefront has moved away, as it happens in the upper right area in aVR and V1 leads. On the other hand, the P-waves corresponding to leads in the left side of the torso presented positive values, since the wavefront is moving in that direction going from the RA to the LA. Some regions on the torso surface were less sensible to the effect of the atrial propagation and remained at low potentials or at rest.

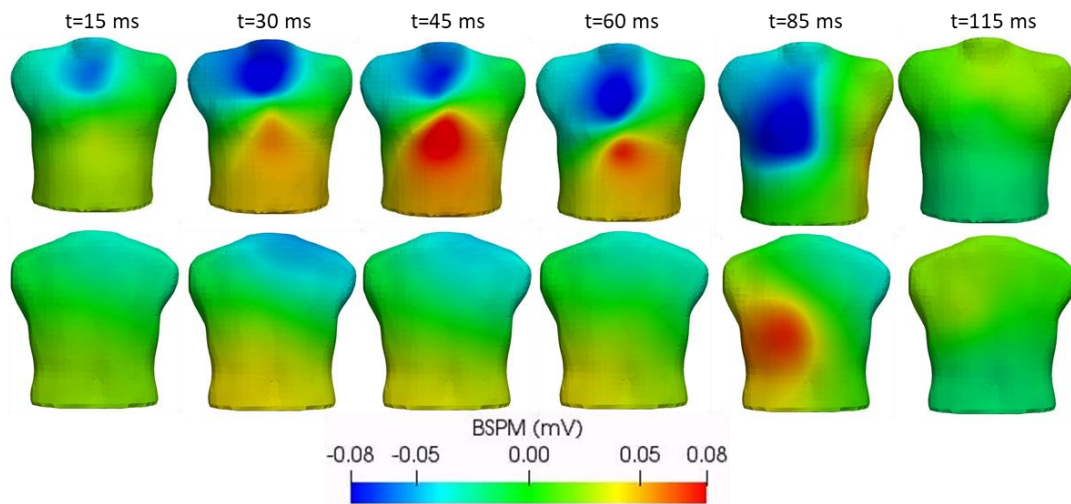


Figure 60. BSPM for the control simulation of patient 1403865 at different time instants in the front (top) and back (bottom) coronal view

4.4. ARRHYTHMIA SIMULATIONS

4.4.1. Atrial simulations

With the aim of generating atrial arrhythmias, the standard stimulation S1-S2 protocol was applied. The stimulus S2 is the responsible of generating an ectopic focus that will try to trigger an arrhythmic pattern. First, we decided to locate the ectopic focus in the PV region since it is a well-known region with ectopic activity [57]. Then we determined the vulnerable window, i.e. the time intervals in which the stimulation protocol induces a maintained arrhythmic activity after the ectopic foci, for each of the atrial models. When comparing vulnerability windows between the 4 models, considerable differences were noticed. Since the ectopic foci was applied at the same region, the outcome of inducing arrhythmic behavior will mainly depend on the anatomy of the atria. For model 3014094, macroreentrant activity could only be induced with

the stimulus launched 195 ms after the SAN depolarization. With the stimulus applied at 190 or 200 ms, maintained reentrant activity did not appear and the atria remained at rest. For the rest of the models, macroreentries were produced no matter at what time instant the stimulus was applied.

For the 4 atrial models, we were able to obtain the same maintained arrhythmic pattern after introducing 6 ectopic foci in the PV region. A self-sustained macroreentry spreading from LA to RA through the BB and LFO, and from RA to LA through the CS, was achieved for every model, which will be explained in detail in this section. In Figure 61, 62, 63, and 64, the activation sequences for the models 1403865, 3014094, 3023001, and 3196630, respectively, can be observed. The time instants present in the sequence go from the beginning of the last ectopic focus in the PV until the macroreentry is induced, in order to show the inducing mechanism. Panel A shows the last ectopic focus applied in the PV. At this time instant the previous stimulus is still propagating from LA to RA. In panel B, the last ectopic focus expanding along the LA can be observed, while the RA is depolarizing towards the MV and CS. The wavefront coming from the RA and the one that arose from the last stimulus collide in the CS region, not allowing one or another pass through the CS and keep propagating along the other atrium. While this occurs, propagation of the last stimulus goes from the LA to the RA through the BB and LFO in the opposite direction of normal rhythm (panel C). Propagation continues through the RA, and now since the ectopic focus has stopped, there is no other wavefront to collide with in the CS area, that is repolarized so propagation advances along the CS into the LA inducing the macroreentry (panel D). In panels E-G it can be observed how propagation is maintained due to the macroreentry through the CS, depolarizing first the LA and passing the electric activity towards the RA.

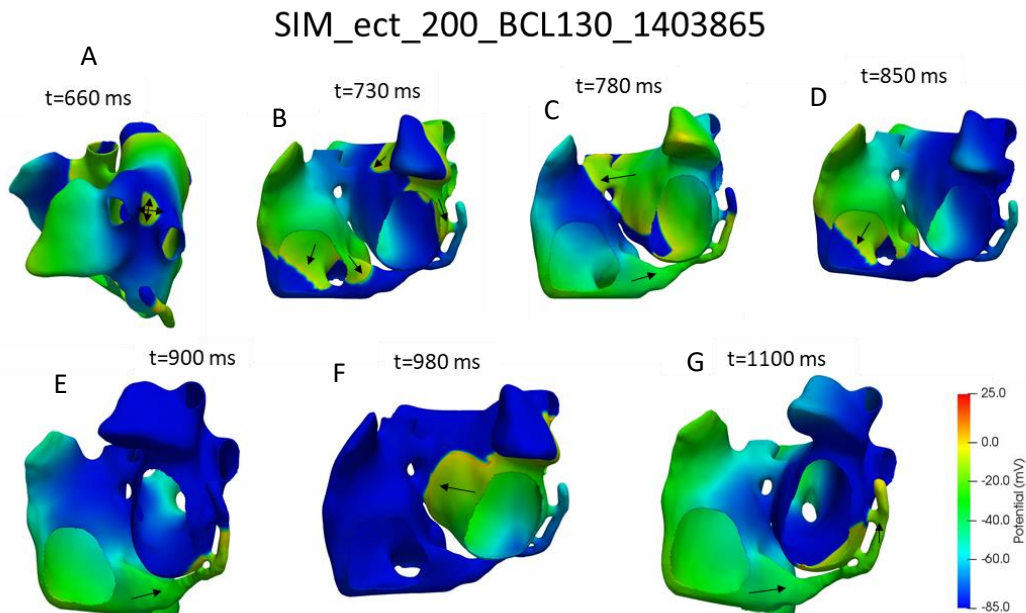


Figure 61. Activation sequence showing the induced the induced macroreentrant activity for model with patient ID 1403865

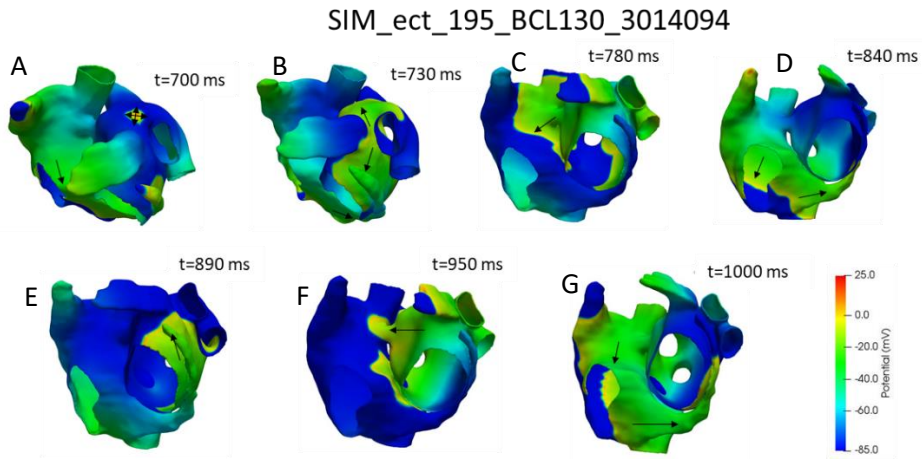


Figure 62. Activation sequence showing the induced the induced macroreentrant activity for model with patient ID 3014094

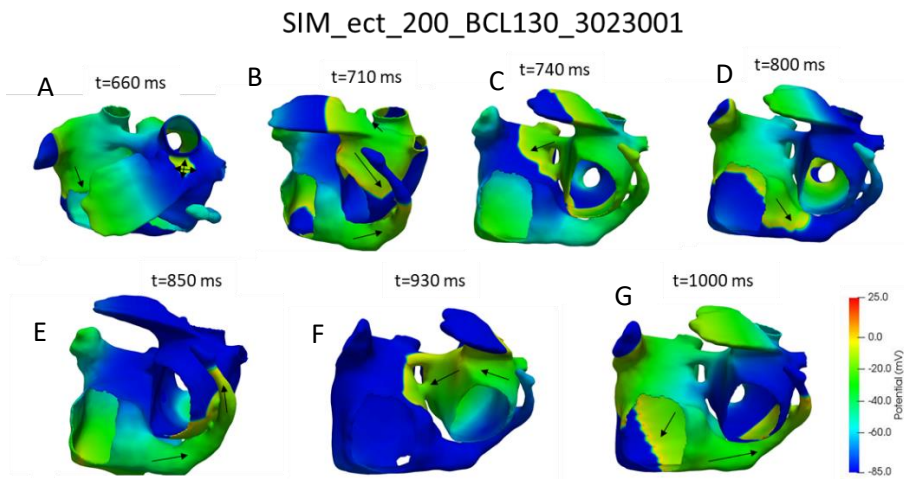


Figure 63. Activation sequence showing the induced the induced macroreentrant activity for model with patient ID 3023001

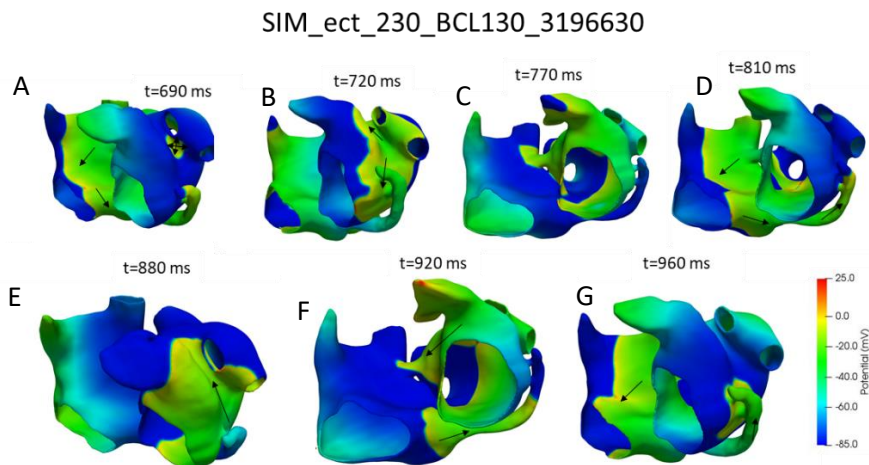


Figure 64. Activation sequence showing the induced the induced macroreentrant activity for model with patient ID 3196630

In Figure 65, 66, 67, and 68, the potential evolution of a node located in the PV region can be observed. This was useful for detecting when the propagation was maintained after the ectopic foci and to determine the atrial pace. Around 800 ms, a delay in the potential propagation coinciding with the macroreentry initiation can be observed, more noticeable in Figures 65 and 67. Prior to this delay the atria were excited at the BCL (130 ms). After that, the macroreentry is maintained at a constant pace, slower than the atrial ectopic foci pacing. For comparing the different model pace rates, the beats in the interval between 800 ms and 2000 ms were counted. For model 1403865 6 beats appeared during that time interval (300 bpm), for model 3014094 9 beats (450 bpm), for model 3023001 8 beats (400), and finally for model 3196630 10 beats (500 bpm).

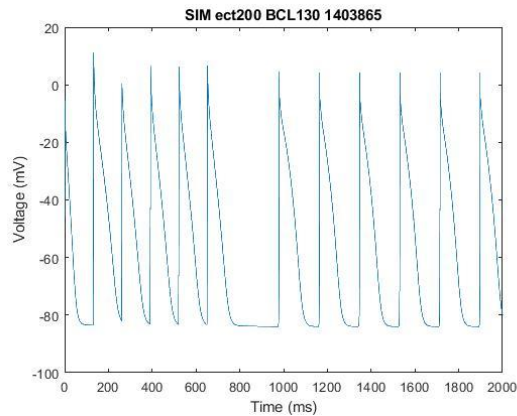


Figure 65. Potential extracted at node 634057 where the ectopic focus is applied in the PV during the simulation with the S2 protocol for simulation with 6 ectopic foci given at a BCL of 130 for model with patient ID 1403865.

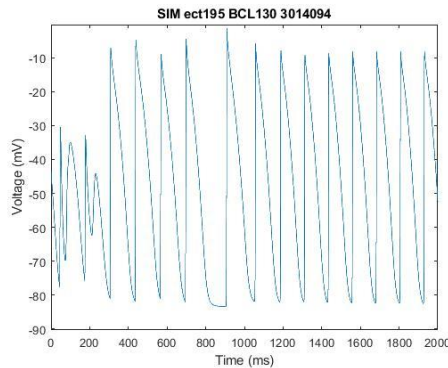


Figure 66. Potential extracted at node 764405 where the ectopic focus is applied in the PV during the simulation with the S2 protocol for simulation with 6 ectopic foci given at a BCL of 130 for model with patient ID 3014094.

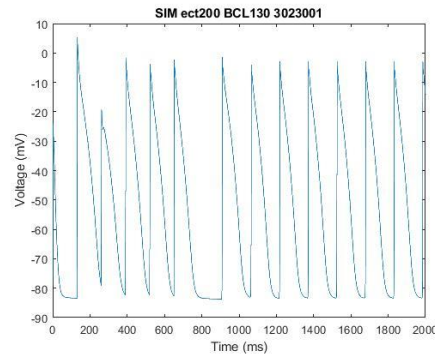


Figure 67. Potential extracted at node 630342 where the ectopic focus is applied in the PV during the simulation with the S2 protocol for simulation with 6 ectopic foci given at a BCL of 130 for model with patient ID 3023001.

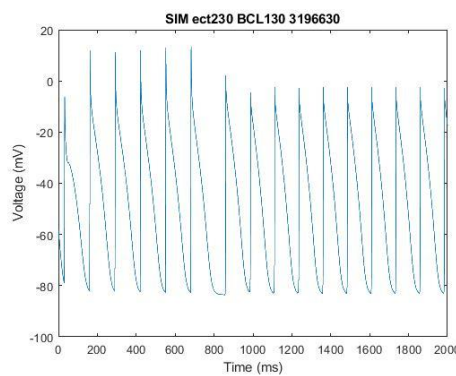


Figure 68. Potential extracted at node 1466884 where the ectopic focus is applied in the PV during the simulation with the S2 protocol for simulation with 6 ectopic foci given at a BCL of 130 for model with patient ID 3196630.

4.3.2. Torso simulations

For patient 1403865, the arrhythmia simulation where a macroreentry through the CS was induced, was propagated along the torso model and compared to the control conditions simulation in order to study the differences in the torso electrical activity through the BSPM. First, the ECG signals at the 6 precordial leads (same position as in Figure 59) were obtained for the macroreentry simulation, as shown in Figure 69. Two clear segments can be differentiated: the electrical activity generated by the ectopic foci, and the one created by the macroreentrant activity, which starts around 850 ms. By looking at the morphology and characteristics of the signals, we can clearly see how they are different from the ones obtained in control. In control, only in the precordial leads V1 and V2 a negative potential was achieved, while in this case every precordial lead gives a signal with negative component due to the inversion of the propagation patterns (electrical impulse travels from LA to RA through the BB and LFO). The amplitude of the signals is also considerably higher compared to the control results.

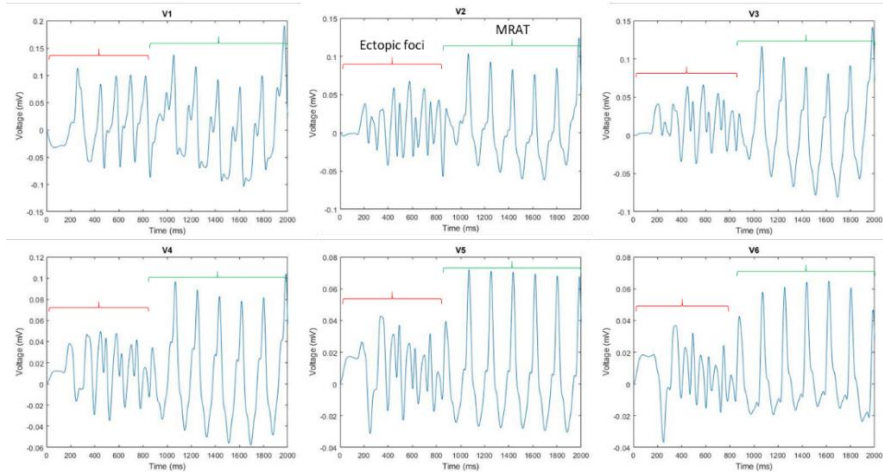


Figure 69. ECG signals of the 6 precordial leads during the macroentry simulation for patient 1403865.

Later, BSPM were computed in order to analyze the electrical propagation in the full torso surface. The electrical propagation of the macroentry simulation on the front and back coronal views of the torso surface is shown in Figure 70. The time instants depicted in the figure correspond to the period of time between the last ectopic focus (panel A) and initiation of the macroentry (panel B), coinciding with the atrial activation sequence shown in Figure 61. It can be clearly seen how the BSPM sequence is unconventional, different from what can be observed in the control situation (Figure 60). While for control conditions the propagation of the wavefront moves from the right upper towards the left lower quadrant of the torso, during the ectopic foci the wavefront propagates towards the inferior half of the torso and then back towards the superior half. In addition, the propagation during the macroentry propagates again from the superior to the inferior half of the torso, and then migrates to the left side. Between time instants 1020 and 1050 a very intense dipole is formed, affecting also the back side of the torso surface, something that did not happen in the control case, where it was barely unaffected throughout the entire propagation.

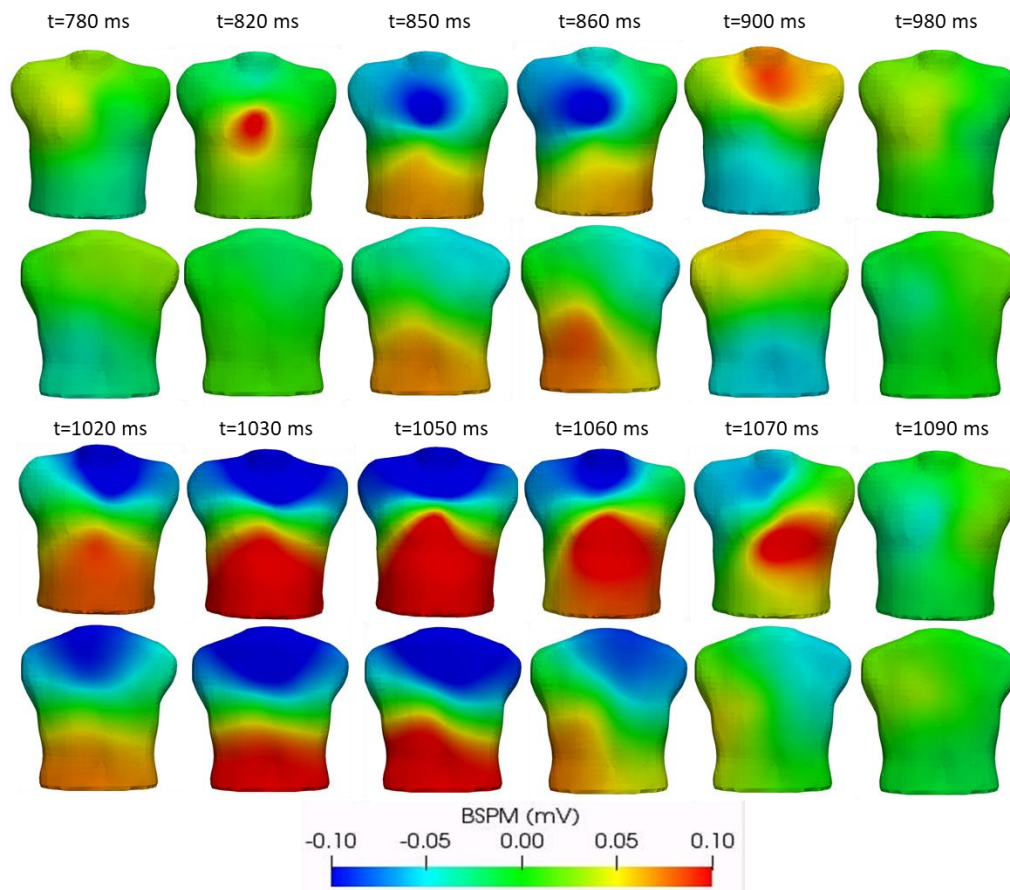


Figure 70. BSPM for the macroreentry simulation for patient 1403865 at different time instants in the front (top) and back (bottom) coronal view

CHAPTER 5. DISCUSSION

The main objective of this work was the development of a methodology for the creation of highly detailed 3D personalized atria and torso models. In addition, electrophysiological simulations in control and pathological conditions were performed with the developed models. In this chapter, the methodology designed, and the results obtained will be discussed.

5.1. CREATION OF PERSONALIZED ATRIA AND TORSO MODELS

First part in the creation process of patient specific atria and torso models consists in the segmentation of the anatomical structures from medical images. For this purpose, we were provided directly the CT scans of different patients. Unfortunately, for irregular and complex anatomies like the atria, no completely automatic segmentation software is yet available and it is always needed a manual adjustment. Not even the segmentation software provided by the CT machines properly performed the segmentation and there is always a need of modifications, as in the work done by Roberto [109], where the Philips Intellispace Portal was used for obtaining automatically segmented models of the heart structures. Different improved algorithms for the segmentation of the RA and LA have been proposed [138]–[141], but they still depend on the characteristics of the images and therefore we chose the free Seg3D software for a semi-automatic segmentation based on seeds growth. As commonly occurs during the segmentation process, although images provided by Hospital Politécnico y Universitario La Fe were of great quality and segmentation could be performed successfully, some modifications were made slice by slice in order to achieve accurate models. Surfaces resulting from the segmentation were validated by specialists to assure the accuracy of the models and the reproducibility of the real patients' anatomy. As a result, the detailed atrial anatomies obtained reflex the variability among patients. For instance, one of the atrial models presents a typical LAA morphology of chicken wing [142], and there is a wide range of sizes between the different atrial models (from 542 cm² to 688 cm²).

An additional problem found while segmenting the atria is the incapability of CT images to show the unions between RA and LA (BB, FO, and CSc). These structures cannot be clearly seen and therefore, their location had to be supposed and added to the model. In order to truly reproduce the atrial anatomy, those regions and their location were defined based on the atrial model created previously by Ferrer et al. [5] and the supervision of specialists. Similarly to the interatrial unions, atrial thickness of the different regions of the atria could not be differentiated in the CT images, due to its thinness, and only the external surface could be segmented. Our models were provided with an homogeneous wall thickness between 0.9 and 1.2 mm in accordance to prior models that do not account for thickness heterogeneity in the atria [5]. However, it has been experimentally observed a variation in the thickness throughout the atria between 2 mm and 5 mm [143], [144]. Based on literature, an atrial model that incorporated a

realistic wall thickness heterogeneity was recently developed by Rocher [68]. Nevertheless, since in the CT scans the thickness cannot be determined, up till now the addition of thickness variability is a manual task that cannot be automatized in the pipeline of personalized atrial model generation.

The generated models comprise a high level of detail regarding the anatomical and electrophysiological regions of the atria. The definition of regions in our atrial models was based on what was done by Ferrer et al. [5], which is one of the most detailed and realistic models in the world. The 4 atrial models developed in this work, with 41 different regions that have assigned different material properties (conductivity and anisotropy), cellular behavior (ionic models), and fiber orientation, have the same level of detail than the one generated by Ferrer et al. [5], but one of the main differences between them is the methodology used for the atrial regions definition. While atrial regions in Ferrer et al model were manually defined, our highly realistic and detailed models were the outcome of a semi-automatic process, which is necessary when building a high number of personalized models. There are other personalized models built in an automatized manner, but they are more simplistic and do not have this high level of detail and atrial region differentiation. The patient specific models generated by Roberto [109] were more simplistic and did not have this high level of detail. Different methods for dividing the regions of the atria can be found in the literature [109], [110], [145], [146]. They all consist in semiautomatic algorithms where the user introduces some points in the atrial mesh, and separation on the specific regions is achieved. Roney et al. [146] used an universal atrial coordinate system by solving Laplace's equation to divide the atria in the PV, SCV, IVC, RAA, and LAA. Hoermann et al. [145] used 13 landmark points to establish a relation with a defined atlas by means of mapping. Krueger et al. [110] developed an algorithm that uses 22 seed points and a 3D fast marching level set method to determine the shortest path between different points. Roberto [109] designed an algorithm that uses 37 points and divides the atria in 16 regions by means of atrial coordinate delimitation. All these methods are able to generate heterogeneous atria model, but not with the level of detail characteristic of reality and reproduced by Ferrer et al. [5] and this work. In this work, an algorithm able to divide the atria in 45 regions by using 59 seed points. The idea of determining the shortest path between points was applied for the regions that have an orifice, and for the rest an improved method was developed based on the work of Roberto [109] as described in the methods section. The fiber direction was assigned based on the model created by Ferrer et al. [5], since histological information was not provided for our patients.

Finally, fiber direction was assigned based on histological observations [6], similarly to the model created by Ferrer et al.[5]. Histological information was not provided from our patients since hearts were not explanted. In order to obtain patient-specific fibers direction, diffusion tensor imaging can be employed [104]. However, this technique is not performed by default in the Hospital Politécnico y Universitario la Fe and we were not provided with this information.

The torso model built in this work includes the following main organs apart from the atria: ventricles, blood, bone, liver, lungs, kidneys, and skin (torso surface). When comparing to the torso model created by Ferrer et al. [5], the mentioned did not include the kidneys. Although, this addition does not seem to affect the results from the simulations, but it is a realistic added element to the model. Also, instead of using just the torso and atria surface models as input for the meshing of the final torso model like Ferrer et al. [5] did, all the organs were remeshed and

used in the meshing of the volumetric torso model. This results in a greater resolution, and more detailed organs, but increases the number of elements and points, elevating the computational cost of the simulations. The generated torso model is made up by 3,719,113 cells and 593,607 points, compared to 1,149,531 cells and 224,709 points in the torso model created by Ferrer et al. [5]. The atria used by Ferrer et al. [5] in the simulations of the propagation on the electrical activity on the torso did not correspond with the original atrial model of the torso. In this case, the entire model is specific of patient with ID 1403865. Every organ was segmented from the original CT scan, adding a high fidelity of reality in our model.

5.2. ELECTROPHYSIOLOGICAL SIMULATIONS

Our models were adjusted based on experimental observations in order to obtain simulations in control conditions that reproduce the experimental activation times indicated by Lemery et al. [123]. As a result, the propagation patterns obtained for all 4 atrial models coincide with a typical propagation in the atria in absence of arrhythmias. Similarly, the torso simulation was also validated through P-waves morphology and duration at the ECG standard leads and BSPM, by comparison with experimental and simulation studies found in the literature [28], [75], [135]–[137]. Altogether, our models have been demonstrated to be a proper, validated and accurate tool to be used for further studies.

When inducing arrhythmias with the standard S1-S2 stimulation protocol, applied at the PV, all the atrial models yielded the same type of macroreentry through the CS. However, due to the difference in the anatomy of the models, different vulnerability windows and pace rates were obtained. Since the ectopic foci was applied at the same region and models had the same atrial regions and fibers orientation, these variations mainly depended on the anatomy of the atria and the slight differences in the conductivities assign to the models. Regarding the torso simulations, like in the atrial simulations, the P-waves and BSPM patterns during arrhythmia considerably differ from those under control conditions, being an indicator of an abnormal electrical activity in the atria. These results are in accordance with other studies [28], [105], in which differences between normal and pathological conditions, as well as between different individuals have been detected.

5.3. LIMITATIONS

In this section the limitations of this work are detailed.

On one hand, although the methodology designed is semi-automatic, there is still a need of interaction from the user. The process is not completely automatized due to the high level of detail needed in our models. Therefore, the process still requires a lot of effort and is time consuming.

On the other hand, although the 3D atrial models developed are highly detailed and realistic, they do not account for the heterogeneous wall thickness existent in real human atria.

In addition, fibers direction was defined based on real histological data but is not patient specific, since diffusion tensor imaging was not available, and there might be some slight variations in the fiber direction between patients. Also, fibrotic regions were not included in these models. Our models could include all these three factors (heterogeneous wall thickness, fibers orientation and fibrosis) as patient-specific in case of performing novel and high definition imaging techniques, which are expensive and are not always available in the hospitals.

Finally, atrial models were adjusted to meet activation times seen in experimental studies. But the simulations were not personalized in terms of electrophysiology. Adjustment of models would be improved in terms of reproducibility of patients' electrophysiology based on the intracavitary registrations (electroanatomical mapping) and the ECG signals of the patients.

CHAPTER 6. CONCLUSION

The principal objective of this work consisted on the design of a methodology for the development of personalized atria and torso models. Applying the methodology designed, 4 3D atria models and 1 torso model were obtained.

First, we can conclude from this work that although segmentation from the CT images is semi-automatic, it is still time consuming since the delimitation of the regions must be smooth and accurate in order to obtain realistic surfaces to be meshed. High quality CT scans facilitates and accelerates the segmentation process.

Second, due to the complex atrial anatomy, the algorithm to define the atrial regions must be semi-automatic and requires the interaction of the user, who has to provide proper selected data in the mesh as an input for the success of the region delimitation. As a result, highly detailed 3D atrial models can be developed, which reflex the variability in the atrial anatomy among patients.

In addition, we also can conclude that models need to be adjusted based on experimental observations to be able to reproduce normal propagation patterns in control conditions, which are well known, and predict unknown abnormal patterns by comparison with the control conditions. The different atrial models gave similar propagation patterns in absence of arrhythmias. Noticeably, simulations of arrhythmic activity showed variations in the propagation patterns and the vulnerable windows between patients, fact that demonstrate the importance of developing personalized models. Similarly, torso simulations allowed the detection of arrhythmias when comparing the BSPM and ECG signals in presence and absence of arrhythmia.

In conclusion, a methodology for creating highly detailed personalized 3D atria and torso models was developed and different simulations with the generated models were performed. The creation of patient specific models is time consuming and implicates considerable manual interaction. In this work, the methodology proposed reduces the generation times with the goal of advancing into introducing these specific cardiac models in the clinical practice. Personalized 3D cardiac models have demonstrated great potential at the clinical level, as they allow to control electrophysiological studies and plan therapies using the real anatomy of the patients.

CHAPTER 7. FUTURE WORK

This work opens different future research lines that can improve the generation of personalized models, and the simulations performed with them.

Automatic segmentation algorithms would reduce considerably the time spent in the creation of the personalized models. With the help of artificial intelligence, automatic algorithms for the segmentation of the atria and the torso organs could be developed. Although, a manual supervision and possibly adjustment will have to be done by the user in order to obtain detailed anatomical models.

In this work, electrical atrial remodeling has been only included, but physiological changes in the remodeling of cAF also include structural variations. Fibrosis could be added to the models in the cases it is present, adding more realism to the simulations.

The standard S1-S2 protocol has been applied at the PV in our arrhythmia simulations for initiating arrhythmic activity. Other locations for the ectopic focus could be assigned, like the CS or CTS, and simulations can be run to study how the propagation changes.

Regarding the electrophysiological simulations, the models have been adjusted based on general experimental studies. In this work, we were not provided with electrophysiological data from the patients, so personalization could only be done at the anatomical level. A future improvement would be the adjustment of the models based on the real acquired signals from the specific patient. Intracavitary recordings would give us the atrial activation times, and models would be modified in order to replicate this behavior. ECG signals can be used for adjusting the model, since with the torso simulation the P-wave is obtained, which could also be imitated. This would replicate with much more realism the electrophysiology of the real patient, and personalized treatments could be conducted based on the simulation performed.

The developed models can be used as a tool for different simulation studies. For example, since models have been used before to improve the success possibilities of ablation procedures [147], with these personalized models, patient specific planification of the ablation lines could be done, improving the results achieved clinically.

Finally, ventricle models could be segmented with more level of detail and electrophysiological properties could be added. A whole heart cardiac model could be obtained, and simulations could be performed to study the complete heart behavior and pathologies such as atrioventricular node block.

CHAPTER 8. ANEXS

8.1 MATLAB CODES

8.1.1. Algorithm for labelling in RA and LA

```
function labelling(varargin)
ambas='auriculas definitiva final cm ids.vtk';
ca='centroides auriculas definitiva nueva.vtk';
cd='centroides auricula derecha definitiva nueva.vtk';
ci='centroides auricula izquierda definitiva nueva.vtk';
auriculas=vtk2structReader(ambas);
CCt=vtk2structReader(ca);
CCd=vtk2structReader(cd);
CCi=vtk2structReader(ci);
display('Files read');
[Dd,posd]=pdist2(CCd.Points,CCt.Points,'euclidean','Smallest',1);
[Di,posit]=pdist2(CCi.Points,CCt.Points,'euclidean','Smallest',1);
display('Distances obtained');
save('Dd.mat','Dd');
save('Di.mat','Di');
for i=1:auriculas.NumCells
    if Dd(i)<Di(i)
        capa(i)=1;
    else
        capa(i)=2;
    end
end
save('capa.mat','capa');
auriculas.CellData(2).Name='RA-LA';
auriculas.CellData(2).Format='double';
auriculas.CellData(2).Type='SCALARS';
auriculas.CellData(2).Data=capa;
struct2vtkWriter(auriculas,'path','labelled model');
end
```

8.1.2. Main algorithm for region division

```
function Region_division(varargin)
%% Start of the program
%Introduction of 35 points (if 4 CS connections), 32 (if 3 CS connections)
%Introduction of 24 cells
%47 regions
%% For modifying manually CellData or PoinData
% celdas=csvread('to8(1).csv',1,0);
% celdas=celdas(:,1);
% celdas=celdas+1;
% atria.CellData(3).Data(celdas)=8;
%%
clc
clear all
atria=vtk2structReader('modelo etiquetado FINAL.vtk');
CC=vtk2structReader('centroides modelo etiquetado FINAL.vtk');
edge=vtk2structReader('edges modelo etiquetado FINAL.vtk');
atria.CellData(3)=atria.CellData(2);
atria.CellData(3).Name='OrganID';
d=size(CC.Points(:,3),1);
```

```

Ref(:,:)=CC.Points(:,:); %Define reference
RefIndex=zeros(length(CC.Points),1);
for i=1:length(CC.Points)
    RefIndex(i,1)=i-1;
end
%% DEFINITION OF POINTS IN RA and LA
%Find points and nodes of the two atria
puntoStotal=atria.PointData.Data;
nodes=[puntoStotal atria.Points(:,:)];
%Find points and nodes of RA
X=find(atria.CellData(2).Data ==1);
puntos=atria.Cells(X,:);
puntos2=[puntos(:,1);puntos(:,2);puntos(:,3)];
puntos3=unique(puntos2);
puntosRA=sort(puntos3);
nodesRA=[puntosRA atria.Points(puntosRA+1,:)];
RefRA=RefIndex(atria.CellData(2).Data ==1);
RefRA=zeros(length(Ref),1);
for i=1:length(RefIndex)
    if atria.CellData(2).Data(i) == 1
        RefRA(i,1)=RefIndex(i,1);
    end
end;
puntosRight=zeros(length(puntoStotal),1);
for i=1:length(puntoStotal)
    if ~isempty(find(i-1==puntosRA))
        puntosRight(i)=i-1;
    end;
end;
%Find points and nodes of RA
Y=find(atria.CellData(2).Data ==2);
puntos5=atria.Cells(Y,:);
puntos6=[puntos5(:,1);puntos5(:,2);puntos5(:,3)];
puntos7=unique(puntos6);
puntosLA=sort(puntos7);
nodesLA=[puntosLA atria.Points(puntosLA+1,:)];
RefLA=zeros(length(Ref),1);
for i=1:length(RefIndex)
    if atria.CellData(2).Data(i) == 2
        RefLA(i,1)=RefIndex(i,1);
    end;
end;
puntosLeft=zeros(length(puntoStotal),1);
for i=1:length(puntoStotal)
    if ~isempty(find(i-1==puntosLA))
        puntosLeft(i)=i-1;
    end;
end;

%% MITRAL VALVE
point1=218006;%point, not cell
point2=32195;
point3=3941;
distmitral=0.7;
IDmitral=3;
[atria,cellsmitral]=findREGION (atria,edge,puntosLA,nodesLA,puntosLeft,point1,point2,point3,distmitral,IDmitral);
for i=1:length(cellsmitral)
    Ref(cellsmitral(i),:)=0;
    RefIndex(cellsmitral(i),:)=0;
end;
save('cellsmitral.mat','cellsmitral');

%% TRICUSPID VALVE %%
point4=525159;
point5=282177;
point6=525020;
disttri=0.7;
IDtri=4;
[atria,cellstri]=findREGION (atria,edge,puntosRA,nodesRA,puntosRight,point4,point5,point6,disttri,IDtri);
for i=1:length(cellstri)
    Ref(cellstri(i),:)=0;

```

```

    RefIndex(cellstri(i,:))=0;
end;
save('cellstri.mat','cellstri');

%% INFERIOR CAVE VEIN %%
point7=382012;
point8=220588;
point9=238925;
distCavalnf=0.35;
IDCavalnf=5;
[atria,cellsCavalnf]=findREGION (atria,edge,puntosRA,nodesRA,puntosRight,point7,point8,point9,distCavalnf,IDCavalnf);
for i=1:length(cellsCavalnf)
    Ref(cellsCavalnf(i,:))=0;
    RefIndex(cellsCavalnf(i,:))=0;
end;
save('cellsCavalnf.mat','cellsCavalnf');

%% CONNECTIONS OF CORONARY SINUS %%
point10=22326;
point11=19988;
point12=302921;
distSN1=0.18;
IDSN=6;
[atria,cellsSN1]=findREGION (atria,edge,puntos,nodes,puntostotal,point10,point11,point12,distSN1,IDSN);
for i=1:length(cellsSN1)
    Ref(cellsSN1(i,:))=0;
    RefIndex(cellsSN1(i,:))=0;
end;
save('cellsSN1.mat','cellsSN1');
point13=9312;
point14=284877;
point15=12071;
distSN2=0.12;
[atria,cellsSN2]=findREGION (atria,edge,puntos,nodes,puntostotal,point13,point14,point15,distSN2,IDSN);
for i=1:length(cellsSN2)
    Ref(cellsSN2(i,:))=0;
    RefIndex(cellsSN2(i,:))=0;
end;
save('cellsSN2.mat','cellsSN2');
point16=277087;
point17=276207;
point18=5991;
distSN3=0.07;
[atria,cellsSN3]=findREGION (atria,edge,puntos,nodes,puntostotal,point16,point17,point18,distSN3,IDSN);
for i=1:length(cellsSN3)
    Ref(cellsSN3(i,:))=0;
    RefIndex(cellsSN3(i,:))=0;
end;
save('cellsSN3.mat','cellsSN3');
%If there is a 4th connection
% point19=275127;
% point20=278563;
% point21=285491;
% distSN4=0.07;
% [atria,cellsSN4]=findREGION (atria,edge,puntos,nodes,puntostotal,point19,point20,point21,distSN4,IDSN);
% for i=1:length(cellsSN4)
%     Ref(cellsSN4(i,:))=0;
%     RefIndex(cellsSN4(i,:))=0;
% end;
% save('cellsSN4.mat','cellsSN4');
%% RIGHT PULMONARY VEIN BASE %%
p1=150431+1; %cell, not point %take all cells from LA with <x than this cell
x=zeros(size(CC.Points));
z=zeros(size(CC.Points));
for i=1:d
    if Ref(i,1)<Ref(p1,1)
        x(i,:)=Ref(i,:);
    end
end
CellsRPulm=find(x(:,1)~=0 & atria.CellData(2).Data==2);
atria.CellData(3).Data(CellsRPulm)=7;

```

```

%% LEFT PULMONARY VEIN BASE %%
p4=174868+1;
p2=98804+1;
p3=173001+1;
x=zeros(size(CC.Points));
z=zeros(size(CC.Points));
m=(Ref(p4,3) - Ref(p2,3)) ./ (Ref(p4,2) - Ref(p2,2));

for i=1:d
if Ref(i,3)>(m*(Ref(i,2)-Ref(p2,2))+Ref(p2,3))
x(i,:)=Ref(i,:);
end
end
CellsLPulm=find(x(:,1)~=0 & atria.CellData(2).Data==2 & x(:,3)>Ref(p2,3) & x(:,1)>Ref(p3,1));
atria.CellData(3).Data(CellsLPulm)=8;
%%%%%%%%%%%%%%%%%%%%%%%%%%%%%%%%%%%%%%%%%%%%%%%%%%%%%%%%%%%%%%%%%%%%%%%%
%% RIGHT PULMONARY VEINS %%
puntos=atria.Cells(CellsRPulm,:);
puntos2=[puntos(:,1);puntos(:,2);puntos(:,3)];
puntos3=unique(puntos2);
puntosRPulm=sort(puntos3);
nodesRPulm=[puntosRPulm atria.Points(puntosRPulm+1,:)];
puntosRefRPulm=zeros(length(puntostotal),1);
for i=1:length(puntostotal)
if ~isempty(find(i-1==puntosRPulm))
puntosRefRPulm(i)=i-1;
end;
end;
point22=642566;%punto, Superior
point23=316422;%punto
point24=643283;%punto
point25=644788;%Inferior
point26=644175;
point27=644439;
distRpulS=0.82;
distRpulI=1;
IDRpulSup=9;
IDRpulInf=10;
IDRpulunion=11;
[atria,cellsRSup,cellsRInf,cellsRUnion,pathRSup,pathRInf]=regionPulmonary
(atria,edge,puntosRPulm,nodesRPulm,puntosRefRPulm,point22,point23,point24,point25,point26,point27,distRpulS,distRpulI,IDRpulSup,IDRpulInf,IDRpulunion);
save('pathRSup.mat','pathRSup');
save('pathRInf.mat','pathRInf');
for i=1:length(cellsRSup)
Ref(cellsRSup(i,:))=0;
end;
for i=1:length(cellsRInf)
Ref(cellsRInf(i,:))=0;
end;
for i=1:length(cellsRUnion)
Ref(cellsRUnion(i,:))=0;
end;
save('cellsRSup.mat','cellsRSup');
save('cellsRInf.mat','cellsRInf');
save('cellsRUnion.mat','cellsRUnion');
%% LEFT PULMONARY VEINS %%
puntos=atria.Cells(CellsLPulm,:);
puntos2=[puntos(:,1);puntos(:,2);puntos(:,3)];
puntos3=unique(puntos2);
puntosLPulm=sort(puntos3);
nodesLPulm=[puntosLPulm atria.Points(puntosLPulm+1,:)];
puntosRefLPulm=zeros(length(puntostotal),1);
for i=1:length(puntostotal)
if ~isempty(find(i-1==puntosLPulm))
puntosRefLPulm(i)=i-1;
end;
end;
point28=641841;%Superior
point29=641976;
point30=642306;

```

```

point31=640944;%Inferior
point32=641402;
point33=641184;
distLpulS=0.46;
distLpull=0.73;
IDLpulSup=12;
IDLpullInf=13;
IDLpulunion=14;
[atria,cellsLSup,cellsLInf,cellsLUnion,pathLSup,pathLInf]=regionPulmonary
(atria,edge,puntosLPulm,nodesLPulm,puntosRefLPulm,point28,point29,point30,point31,point32,point33,distLpulS,distLpull,IDLpul
Sup,IDLpullInf,IDLpulunion);
save('pathLSup.mat','pathLSup');
save('pathLInf.mat','pathLInf');

for i=1:length(cellsLSup)
    Ref(cellsLSup(i,:))=0;
end;
for i=1:length(cellsLInf)
    Ref(cellsLInf(i,:))=0;
end;
for i=1:length(cellsLUnion)
    Ref(cellsLUnion(i,:))=0;
end;
save('cellsLSup.mat','cellsLSup');
save('cellsLInf.mat','cellsLInf');
save('cellsLUnion.mat','cellsLUnion');
%% SAN %%
point34=360842;%points
Y=find(atria.Cells(:,1)==point34 | atria.Cells(:,2)==point34 | atria.Cells(:,3)==point34);
p17=Y(1);
dist=0.30;
[atria,cells] = findSurrounding (atria,Ref,p17,RefIndex,dist);
cells=[cells;725845;727061;727067];
atria.CellData(3).Data(cells)=21;
for i=1:length(cells)
    Ref(cells(i,:))=0;
    RefIndex(cells(i,:))=0;
end;
Z=find(RefIndex);

%% CRISTA TERMINALIS %%
Z=find(RefIndex);
puntos=atria.Cells(Z,:);
puntos2=[puntos(:,1);puntos(:,2);puntos(:,3)];
puntos3=unique(puntos2);
puntosCRESTA=sort(puntos3);
puntosCT=zeros(length(puntostotal),1);
for i=1:length(puntostotal)
    if ~isempty(find(i-1==puntosCRESTA,1))
        puntosCT(i)=i-1;
    end
end
point35=74133;%points
point36=point8;
dist=0.25;
ID=15;
[atria,cells] = findCT (atria,edge,puntosRA,nodesRA,puntosCT,point34,point35,point36,dist,ID);
save('cellsCT.mat','cells');
for i=1:length(cells)
    Ref(cells(i,:))=0;
    RefIndex(cells(i,:))=0;
end;
%% CORONARY SINUS %%
p10=477932+1;
p9=478220+1;
x=zeros(size(CC.Points));
z=zeros(size(CC.Points));
m2=(Ref(p9,2) - Ref(p10,2)) ./ (Ref(p9,1) - Ref(p10,1));
for i=1:d
    if Ref(i,2)>(m2*(Ref(i,1)-Ref(p10,1))+Ref(p10,2)) & Ref(i,2)<(m2*(Ref(i,1)-Ref(p10,1))+Ref(p10,2)+6)
        x(i,:)=Ref(i,:);
    end
end

```

```

end
end
X=find(x(:,1)~=0 & atria.CellData(2).Data==1);
for i=1:length(X)
    Ref(X(i,:))=0;
    RefIndex(X(i,:))=0;
end;
atria.CellData(3).Data(X)=17;%low coronary sinus
for i=1:d
if Ref(i,2)>(m2*(Ref(i,1)-Ref(p10,1))+Ref(p10,2)+6)
z(i,:)=Ref(i,:);
end
end
X=find(z(:,1)~=0 & atria.CellData(2).Data==1);
for i=1:length(X)
    Ref(X(i,:))=0;
    RefIndex(X(i,:))=0;
end;
atria.CellData(3).Data(X)=18;%high coronary sinus
%% LEFT APPENDAGE %%
p7=165551+1;
p5=115142+1;
p6=168581+1;
p99=129785+1;
n2=(CC.Points(p7,3) - CC.Points(p5,3)) ./ (CC.Points(p7,1) - CC.Points(p5,1));
n99=(CC.Points(p99,2) - CC.Points(p6,2)) ./ (CC.Points(p99,1) - CC.Points(p6,1));
z=zeros(size(CC.Points));
for i=1:d
if Ref(i,3)>(n2*(Ref(i,1)-CC.Points(p5,1))+CC.Points(p5,3)) & Ref(i,2)<(n99*(Ref(i,1)-CC.Points(p6,1))+CC.Points(p6,2))
z(i,:)=Ref(i,:);
end
end
Z=find(z(:,1)~=0 & atria.CellData(2).Data==2);
for i=1:length(Z)
    Ref(Z(i,:))=0;
    RefIndex(Z(i,:))=0;
end;
atria.CellData(3).Data(Z)=16;
%% DELETE POSITIONS OF PULMONARY VEINS
for i=1:length(CellsRPulm)
    Ref(CellsRPulm(i,:))=0;
    RefIndex(CellsRPulm(i,:))=0;
end;
for i=1:length(CellsLPulm)
    Ref(CellsLPulm(i,:))=0;
    RefIndex(CellsLPulm(i,:))=0;
end;
%% RIGHT APPENDAGE %%
p12=661366+1;
p13=659006+1;
p11=731568+1;
z1=Ref(p12,[2 3]);
z2=Ref(p11,[2 3]);
z3=Ref(p13,[2 3]);
k=[z1;z2;z3];
fitobject7 = fit(k(:,1),k(:,2),'poly2');
values7 = coeffvalues(fitobject7);
x=zeros(size(CC.Points));
z=zeros(size(CC.Points));
for i=1:d
if Ref(i,3)>values7(1)*Ref(i,2)^2+values7(2)*Ref(i,2)+values7(3)
x(i,:)=Ref(i,:);
end
end
X=find(x(:,1)~=0 & atria.CellData(2).Data==1);
for i=1:length(X)
    Ref(X(i,:))=0;
    RefIndex(X(i,:))=0;
end;
atria.CellData(3).Data(X)=19;

```

```

%% SUPERIOR CAVA VEIN %%
p14=731906+1; %lo mismo que para la orejuela derecha
p16=705549+1;
n=(Ref(p14,3)-Ref(p16,3))./(Ref(p14,2)-Ref(p16,2));
x=zeros(size(CC.Points));
z=zeros(size(CC.Points));
for i=1:d
if Ref(i,3)>(n*(Ref(i,2)-Ref(p16,2))+Ref(p16,3))
x(i,:)=Ref(i,:);
end
end
X=find(x(:,1)~=0 & atria.CellData(2).Data==1);
for i=1:length(X)
Ref(X(i,:),:)=0;
RefIndex(X(i,:),:)=0;
end;
atria.CellData(3).Data(X)=20;

%% FOSSA OVALIS %%
p18=278666+1;%point in the middle
p182=934387+1;
dist=0.4;
dist2=0.8;
CoordFO=CC.Points(p18,:);

[atria,cells2] =findSurrounding (atria,Ref,p18,RefIndex,dist2);
atria.CellData(3).Data(cells2)=23;

[atria,cells21] =findSurrounding (atria,Ref,p182,RefIndex,dist2);
atria.CellData(3).Data(cells21)=23;

[atria,cells] = findSurrounding (atria,Ref,p18,RefIndex,dist);
atria.CellData(3).Data(cells)=22;
for i=1:length(cells)
Ref(cells(i,:),:)=0;
RefIndex(cells(i,:),:)=0;
end;
[atria,cells] = findSurrounding (atria,Ref,p182,RefIndex,dist);
atria.CellData(3).Data(cells)=22;
for i=1:length(cells)
Ref(cells(i,:),:)=0;
RefIndex(cells(i,:),:)=0;
end;
for i=1:length(cells2)
Ref(cells2(i,:),:)=0;
RefIndex(cells2(i,:),:)=0;
end;
for i=1:length(cells21)
Ref(cells21(i,:),:)=0;
RefIndex(cells21(i,:),:)=0;
end;
%% BB_EXT_3
p19=509025+1;
p20=(CC.Points(p5,:)+CC.Points(p7,:))./2;
m3=(p20(3) - CC.Points(p19,3)) ./ (p20(1) - CC.Points(p19,1));
x=zeros(size(CC.Points));
z=zeros(size(CC.Points));
for i=1:d
if Ref(i,3)<(m3*(Ref(i,1)-CC.Points(p19,1))+CC.Points(p19,3)) & Ref(i,3)>(m3*(Ref(i,1)-CC.Points(p19,1))+CC.Points(p19,3)-0.3)
x(i,:)=Ref(i,:);
end
end
X=find(x(:,1)~=0 & x(:,1)>CC.Points(p19,1) & x(:,2)<p20(2) & atria.CellData(2).Data==2);
for i=1:length(X)
Ref(X(i,:),:)=0;
RefIndex(X(i,:),:)=0;
end;
atria.CellData(3).Data(X)=24;
%% BB_EXT_1
p21=524322+1;

```

```

p22=p4;
p23=p6;
m4=(CC.Points(p22,2) - CC.Points(p21,2)) ./ (CC.Points(p22,1) - CC.Points(p21,1));
m5=(CC.Points(p23,2) - CC.Points(p19,2)) ./ (CC.Points(p23,1) - CC.Points(p19,1));
m6=(CC.Points(p19,2) - CC.Points(p21,2)) ./ (CC.Points(p19,1) - CC.Points(p21,1));
m7=(CC.Points(p23,2) - CC.Points(p22,2)) ./ (CC.Points(p23,1) - CC.Points(p22,1));
m8=(CC.Points(p19,3) - CC.Points(p21,3)) ./ (CC.Points(p19,1) - CC.Points(p21,1));
x=zeros(size(CC.Points));
z=zeros(size(CC.Points));
for i=1:d
if Ref(i,2)<(m4*(Ref(i,1)-CC.Points(p21,1))+CC.Points(p21,2)) & Ref(i,2)>(m5*(Ref(i,1)-CC.Points(p19,1))+CC.Points(p19,2)) &
Ref(i,2)>(m6*(Ref(i,1)-CC.Points(p21,1))+CC.Points(p21,2)) & Ref(i,2)<(m7*(Ref(i,1)-CC.Points(p22,1))+CC.Points(p22,2)) &
Ref(i,3)>(m8*(Ref(i,1)-CC.Points(p21,1))+CC.Points(p21,3))
x(i,:)=Ref(i,:);
end
end
X=find(x(:,1)~=0 & atria.CellData(2).Data==2);
for i=1:length(X)
    Ref(X(i,:),:)=0;
    RefIndex(X(i,:),:)=0;
end;
atria.CellData(3).Data(X)=25;
%% BACHMANN BUNDLE (BB)
p24=273677+1;
p25=283947+1;
p26=241112+1;
m6=(Ref(p19,2) - Ref(p21,2)) ./ (Ref(p19,1) - Ref(p21,1));
m7=(Ref(p25,2) - Ref(p24,2)) ./ (Ref(p25,1) - Ref(p24,1));
m8=(Ref(p19,2) - Ref(p24,2)) ./ (Ref(p19,1) - Ref(p24,1));
m9=(Ref(p25,2) - Ref(p21,2)) ./ (Ref(p25,1) - Ref(p21,1));
x=zeros(size(CC.Points));
for i=1:d
if Ref(i,2)<(m6*(Ref(i,1)-Ref(p21,1))+Ref(p21,2)) & Ref(i,2)>(m7*(Ref(i,1)-Ref(p24,1))+Ref(p24,2)) & Ref(i,2)>(m8*(Ref(i,1)-
Ref(p24,1))+Ref(p24,2)) & Ref(i,2)<(m9*(Ref(i,1)-Ref(p21,1))+Ref(p21,2)) & Ref(i,3)>Ref(p26,3)
x(i,:)=Ref(i,:);
end
end
X=find(x(:,1)~=0);
for i=1:length(X)
    Ref(X(i,:),:)=0;
    RefIndex(X(i,:),:)=0;
end;
atria.CellData(3).Data(X)=26;

%% BB_EXT_2
p27=518495+1;
p28=544500+1;
m4=(CC.Points(p22,2) - CC.Points(p27,2)) ./ (CC.Points(p22,1) - CC.Points(p27,1));
m5=(CC.Points(p23,2) - CC.Points(p28,2)) ./ (CC.Points(p23,1) - CC.Points(p28,1));
m3=(CC.Points(p27,2) - CC.Points(p28,2)) ./ (CC.Points(p27,1) - CC.Points(p28,1));

x=zeros(size(CC.Points));
z=zeros(size(CC.Points));
for i=1:d
if Ref(i,2)>(m7*(Ref(i,1)-CC.Points(p22,1))+CC.Points(p22,2)) & Ref(i,2)<(m3*(Ref(i,1)-CC.Points(p28,1))+CC.Points(p28,2)) &
Ref(i,2)<(m4*(Ref(i,1)-CC.Points(p27,1))+CC.Points(p27,2)) & Ref(i,2)>(m5*(Ref(i,1)-CC.Points(p28,1))+CC.Points(p28,2)) &
Ref(i,3)>CC.Points(p27,3)
x(i,:)=Ref(i,:);
end
end
X=find(x(:,1)~=0 & atria.CellData(2).Data==2);
for i=1:length(X)
    Ref(X(i,:),:)=0;
    RefIndex(X(i,:),:)=0;
end;
atria.CellData(3).Data(X)=27;

%% BB_RA
p29=CC.Points(p17,:);
p30=p29;
p29(2)=p29(2)+0.3;

```

```

p30(2)=p29(2)-0.6;
p36=CC.Points(306825+1,:);
z1=p30(1:2);
z2=p36(1:2);
z3=CC.Points(p24,[1 2]);
k=[z1;z2;z3];
fitobject10 = fit(k(:,1),k(:,2),'poly2');
values10 = coeffvalues(fitobject10);
m17=(CC.Points(p24,2) - p30(2)) ./ (CC.Points(p24,1) - p30(1));
m18=(CC.Points(p24,1) - p29(1)) ./ (CC.Points(p24,3) - p29(3));
m19=(p30(3) - p29(3)) ./ (p30(1) - p29(1));
x=zeros(size(CC.Points));
for i=1:d
if Ref(i,2)<=(m7*(CC.Points(i,1)-CC.Points(p24,1))+CC.Points(p24,2))&
Ref(i,2)>values10(1)*Ref(i,1)^2+values10(2)*Ref(i,1)+values10(3) & Ref(i,1)>=(m18*(CC.Points(i,3)-p29(3))+p29(1)) &
Ref(i,3)>CC.Points(p24,3)
x(i,:)=Ref(i,:);
end
end
X=find(x(:,1)~=0 & atria.CellData(2).Data==1);
for i=1:length(X)
    Ref(X(i,:))=0;
    RefIndex(X(i,:))=0;
end;
atria.CellData(3).Data(X)=28;

%% BBR_FO_UNION
x=zeros(size(CC.Points));
for i=1:d
if Ref(i,2)<(m6*(Ref(i,1)-CC.Points(p21,1))+CC.Points(p21,2)) & Ref(i,2)>(m7*(Ref(i,1)-CC.Points(p24,1))+CC.Points(p24,2)) &
Ref(i,2)>(m8*(Ref(i,1)-CC.Points(p24,1))+CC.Points(p24,2)) & Ref(i,2)<(m9*(Ref(i,1)-CC.Points(p21,1))+CC.Points(p21,2)) &
Ref(i,3)>CoordFO(3)
x(i,:)=Ref(i,:);
end
end
X=find(x(:,1)~=0 & atria.CellData(2).Data==1);
for i=1:length(X)
    Ref(X(i,:))=0;
    RefIndex(X(i,:))=0;
end;
atria.CellData(3).Data(X)=29;

%% BBL_FO_UNION
x=zeros(size(CC.Points));
for i=1:d
if Ref(i,2)<(m6*(Ref(i,1)-CC.Points(p21,1))+CC.Points(p21,2)) & Ref(i,2)>(m7*(Ref(i,1)-CC.Points(p24,1))+CC.Points(p24,2)) &
Ref(i,2)>(m8*(Ref(i,1)-CC.Points(p24,1))+CC.Points(p24,2)) & Ref(i,2)<(m9*(Ref(i,1)-CC.Points(p21,1))+CC.Points(p21,2)) &
Ref(i,3)>CoordFO(3)
x(i,:)=Ref(i,:);
end
end
X=find(x(:,1)~=0 & atria.CellData(2).Data==2);
for i=1:length(X)
    Ref(X(i,:))=0;
    RefIndex(X(i,:))=0;
end;
atria.CellData(3).Data(X)=30;

%% ANTERIOR WALL LA
m10=(CC.Points(p4,2) - CC.Points(p1,2)) ./ (CC.Points(p4,1) - CC.Points(p1,1));
m11=(p20(2) - CC.Points(p21,2)) ./ (p20(1) - CC.Points(p21,1));
x=zeros(size(CC.Points));
for i=1:d
if Ref(i,2)<(m10*(Ref(i,1)-CC.Points(p1,1))+CC.Points(p1,2)) & Ref(i,2)>=(m11*(Ref(i,1)-CC.Points(p21,1))+CC.Points(p21,2)) &
Ref(i,3)>=CC.Points(p27,3)
x(i,:)=Ref(i,:);
end
end
X=find(x(:,1)~=0 & atria.CellData(2).Data==2);
for i=1:length(X)
    Ref(X(i,:))=0;

```

```

    RefIndex(X(i,:))=0;
end;
atria.CellData(3).Data(X)=31;

%% ANTERIOR WALL SEPTUM LA
x=zeros(size(CC.Points));
for i=1:d
if Ref(i,2)<(m11*(Ref(i,1)-CC.Points(p21,1))+CC.Points(p21,2)+1)
x(i,:)=Ref(i,:);
end
end
X=find(x(:,1)~=0 & atria.CellData(2).Data==2);
for i=1:length(X)
    Ref(X(i,:))=0;
    RefIndex(X(i,:))=0;
end;
atria.CellData(3).Data(X)=32;

%% POSTERIOR WALL LA
x=zeros(size(CC.Points));
for i=1:d
if Ref(i,2)>=(m11*(Ref(i,1)-CC.Points(p21,1))+CC.Points(p21,2)+1)
x(i,:)=Ref(i,:);
end
end
X=find(x(:,1)~=0 & atria.CellData(2).Data==2);
for i=1:length(X)
    Ref(X(i,:))=0;
    RefIndex(X(i,:))=0;
end;
atria.CellData(3).Data(X)=33;
%% ISTMUS
Y=find(atria.Cells(:,1)==point36 | atria.Cells(:,2)==point36 | atria.Cells(:,3)==point36);
p31=Y(1);
Y=find(atria.Cells(:,1)==point4 | atria.Cells(:,2)==point4 | atria.Cells(:,3)==point4);
p32=Y(1);
Y=find(atria.Cells(:,1)==point5 | atria.Cells(:,2)==point5 | atria.Cells(:,3)==point5);
p37=Y(1);
m12=(CC.Points(p32,2) - CC.Points(p31,2)) ./ (CC.Points(p32,1) - CC.Points(p31,1));
x=zeros(size(CC.Points));
for i=1:d
if Ref(i,2)>=(m12*(CC.Points(i,1)-CC.Points(p31,1))+CC.Points(p31,2)) & Ref(i,2)<(m12*(CC.Points(i,1)-CC.Points(p31,1)-1.5)+CC.Points(p31,2)) & Ref(i,3)<CC.Points(p37,3) & Ref(i,2)<CC.Points(p31,2)+1
x(i,:)=Ref(i,:);
end
end
X=find(x(:,1)~=0 & atria.CellData(2).Data==1);
for i=1:length(X)
    Ref(X(i,:))=0;
    RefIndex(X(i,:))=0;
end;
atria.CellData(3).Data(X)=34;
%% INTERCAVAL BUNDLE RA
p33=CC.Points(p11,:);
p33(2)=p33(2)+0.5;
p34=CC.Points(p31,:);
p34(2)=p34(2)-1;
Y=find(atria.Cells(:,1)==point7 | atria.Cells(:,2)==point7 | atria.Cells(:,3)==point7);
p35=Y(1);
m13=(p34(3) - p33(3)) ./ (p34(2) - p33(2));
m14=(p33(1) - p34(1)) ./ (p33(3) - p34(3));
m15=(CC.Points(p35,3) - CC.Points(p25,3)) ./ (CC.Points(p35,2) - CC.Points(p25,2));
x=zeros(size(CC.Points));
for i=1:d
if Ref(i,3)>(m13*(CC.Points(i,2)-p33(2))+p33(3)) & Ref(i,1)<(m14*(CC.Points(i,3)-p34(3))+p34(1)) & Ref(i,3)<(m15*(CC.Points(i,2)-CC.Points(p25,2))+CC.Points(p25,3))
x(i,:)=Ref(i,:);
end
end
X=find(x(:,1)~=0 & atria.CellData(2).Data==1);
for i=1:length(X)

```

```

Ref(X(i,:),:)=0;
RefIndex(X(i,:),:)=0;
end;
atria.CellData(3).Data(X)=35;
%% INTERATRIA WALL SEPTUM RA
x=zeros(size(CC.Points));
for i=1:d
if Ref(i,2)>=(m12*(CC.Points(i,1)-CC.Points(p31,1))+CC.Points(p31,2))
x(i,:)=Ref(i,:);
end
end
X=find(x(:,1)~=0 & atria.CellData(2).Data==1);
for i=1:length(X)
Ref(X(i,:),:)=0;
RefIndex(X(i,:),:)=0;
end;
atria.CellData(3).Data(X)=36;

%% LATERAL WALL RA
x=zeros(size(CC.Points));
for i=1:d
if Ref(i,2)<(m12*(CC.Points(i,1)-CC.Points(p31,1))+CC.Points(p31,2))
x(i,:)=Ref(i,:);
end
end
X=find(x(:,1)~=0 & atria.CellData(2).Data==1);
for i=1:length(X)
Ref(X(i,:),:)=0;
RefIndex(X(i,:),:)=0;
end;
atria.CellData(3).Data(X)=37;
%% PECTINATE MUSCLES
Y=find(atria.Cells(:,1)==point35 | atria.Cells(:,2)==point35 | atria.Cells(:,3)==point35);
p36=Y(1);
p36=CC.Points(p36,:);
Y=find(atria.Cells(:,1)==point5 | atria.Cells(:,2)==point5 | atria.Cells(:,3)==point5);
p37=Y(1);
p37=CC.Points(p37,:);
p29=CC.Points(p17,:);
p40=CC.Points(p31,:);
p40(2)=p40(2);

m16=(p36(3) - p37(3)) ./ (p36(2) - p37(2));
m17=(p36(3) - p29(3)) ./ (p36(2) - p29(2));
m18=(p36(3) - p40(3)) ./ (p36(2) - p40(2));

x=zeros(size(CC.Points));
for i=1:d
if Ref(i,2)<=(m12*(CC.Points(i,1)-CC.Points(p31,1))+CC.Points(p31,2)-0.4) & Ref(i,2)>(m12*(CC.Points(i,1)-
CC.Points(p31,1))+CC.Points(p31,2)-0.8) & Ref(i,3)<CC.Points(p32,3) & Ref(i,2)<CC.Points(p31,2) && Ref(i,3)<(m18*(CC.Points(i,2)-
p40(2))+p40(3))
x(i,:)=Ref(i,:);
end
end
X=find(x(:,1)~=0 & atria.CellData(2).Data==1);
atria.CellData(3).Data(X)=38;

x=zeros(size(CC.Points));
for i=1:d
if Ref(i,2)<=(m12*(CC.Points(i,1)-CC.Points(p31,1))+CC.Points(p31,2)-1.1) & Ref(i,2)>(m12*(CC.Points(i,1)-
CC.Points(p31,1))+CC.Points(p31,2)-1.5) & Ref(i,3)<CC.Points(p32,3) & Ref(i,2)<CC.Points(p31,2) && Ref(i,3)<(m18*(CC.Points(i,2)-
p40(2))+p40(3))
x(i,:)=Ref(i,:);
end
end
X=find(x(:,1)~=0 & atria.CellData(2).Data==1);
atria.CellData(3).Data(X)=39;

x=zeros(size(CC.Points));
for i=1:d

```

```

if Ref(i,2)<=(m12*(CC.Points(i,1)-CC.Points(p31,1))+CC.Points(p31,2)-1.8) & Ref(i,2)>(m12*(CC.Points(i,1)-
CC.Points(p31,1))+CC.Points(p31,2)-2.7) & Ref(i,2)<CC.Points(p31,2) & Ref(i,2)<CC.Points(p31,2) && Ref(i,3)<(m18*(CC.Points(i,2)-
p40(2))+p40(3)) && Ref(i,3)>=(m16*(CC.Points(i,2)-p37(2))+p37(3)-2.2) & Ref(i,3)<(m16*(CC.Points(i,2)-p37(2))+p37(3)-1.8)
x(i,:)=Ref(i,:);
end
end
X=find(x(:,1)~=0 & atria.CellData(2).Data==1);
atria.CellData(3).Data(X)=40;

x=zeros(size(CC.Points));
for i=1:d
if Ref(i,3)>=(m16*(CC.Points(i,2)-p37(2))+p37(3)-1.7) & Ref(i,3)<(m16*(CC.Points(i,2)-p37(2))+p37(3)-1.4) &
Ref(i,3)<(m17*(CC.Points(i,2)-p29(2))+p29(3)) && Ref(i,3)<(m18*(CC.Points(i,2)-p40(2))+p40(3))
x(i,:)=Ref(i,:);
end
end
X=find(x(:,1)~=0 & atria.CellData(2).Data==1);
atria.CellData(3).Data(X)=41;

x=zeros(size(CC.Points));
for i=1:d
if Ref(i,3)>=(m16*(CC.Points(i,2)-p37(2))+p37(3)-1.1) && Ref(i,3)<(m16*(CC.Points(i,2)-p37(2))+p37(3)-0.8) &&
Ref(i,3)<(m17*(CC.Points(i,2)-p29(2))+p29(3)) && Ref(i,3)<(m18*(CC.Points(i,2)-p40(2))+p40(3))
x(i,:)=Ref(i,:);
end
end
X=find(x(:,1)~=0 & atria.CellData(2).Data==1);
atria.CellData(3).Data(X)=42;

x=zeros(size(CC.Points));
for i=1:d
if Ref(i,3)>=(m16*(CC.Points(i,2)-p37(2))+p37(3)-0.5) & Ref(i,3)<(m16*(CC.Points(i,2)-p37(2))+p37(3)-0.2) &&
Ref(i,3)<(m17*(CC.Points(i,2)-p29(2))+p29(3)) && Ref(i,3)<(m18*(CC.Points(i,2)-p40(2))+p40(3))
x(i,:)=Ref(i,:);
end
end
X=find(x(:,1)~=0 & atria.CellData(2).Data==1);
atria.CellData(3).Data(X)=43;

x=zeros(size(CC.Points));
for i=1:d
if Ref(i,3)>=(m16*(CC.Points(i,2)-p37(2))+p37(3)+0.1) & Ref(i,3)<(m16*(CC.Points(i,2)-p37(2))+p37(3)+0.4) &&
Ref(i,3)<(m17*(CC.Points(i,2)-p29(2))+p29(3)) && Ref(i,3)<(m18*(CC.Points(i,2)-p40(2))+p40(3))
x(i,:)=Ref(i,:);
end
end
X=find(x(:,1)~=0 & atria.CellData(2).Data==1);
atria.CellData(3).Data(X)=44;

x=zeros(size(CC.Points));
for i=1:d
if Ref(i,3)>=(m16*(CC.Points(i,2)-p37(2))+p37(3)+0.7) & Ref(i,3)<(m16*(CC.Points(i,2)-p37(2))+p37(3)+1) &&
Ref(i,3)<(m17*(CC.Points(i,2)-p29(2))+p29(3)) && Ref(i,3)<(m18*(CC.Points(i,2)-p40(2))+p40(3))
x(i,:)=Ref(i,:);
end
end
X=find(x(:,1)~=0 & atria.CellData(2).Data==1);
atria.CellData(3).Data(X)=45;

x=zeros(size(CC.Points));
for i=1:d
if Ref(i,3)>=(m16*(CC.Points(i,2)-p37(2))+p37(3)+1.3) && Ref(i,3)<(m16*(CC.Points(i,2)-p37(2))+p37(3)+1.6) &&
Ref(i,3)<(m17*(CC.Points(i,2)-p29(2))+p29(3)) && Ref(i,3)<(m18*(CC.Points(i,2)-p40(2))+p40(3))
x(i,:)=Ref(i,:);
end
end
X=find(x(:,1)~=0 & atria.CellData(2).Data==1);
atria.CellData(3).Data(X)=46;

```

```
p41=p29;
p41(3)=p37(3)+2.3;
p42=CC.Points(p13,:);
p42(2)=p42(2)-0.5;
p42(3)=p42(3)-0.5;
m19=(p42(3) - p41(3)) ./ (p42(2) - p41(2));

x=zeros(size(CC.Points));
for i=1:d
if Ref(i,3)>=(m19*(CC.Points(i,2)-p41(2))+p41(3)) && Ref(i,3)<(m19*(CC.Points(i,2)-p41(2))+p41(3)+0.3) &&
Ref(i,3)<(m17*(CC.Points(i,2)-p29(2))+p29(3)) && Ref(i,3)<(m18*(CC.Points(i,2)-p40(2))+p40(3))
x(i,:)=Ref(i,:);
end
end
X=find(x(:,1)~=0 & atria.CellData(2).Data==1);
atria.CellData(3).Data(X)=47;

struct2vtkWriter(atria,'folder','final ORGANID model')
end
```

8.1.3. Dijkstra's Shortest Path Algorithm []

```
function [dist,path] = dijkstra(nodes,segments,start_id,finish_id)
%DIJKSTRA Calculates the shortest distance and path between points on a map
% using Dijkstra's Shortest Path Algorithm
%
% [DIST, PATH] = DIJKSTRA(NODES, SEGMENTS, SID, FID)
% Calculates the shortest distance and path between start and finish nodes SID and FID
%
% [DIST, PATH] = DIJKSTRA(NODES, SEGMENTS, SID)
% Calculates the shortest distances and paths from the starting node SID to all
% other nodes in the map
%
% Note:
% DIJKSTRA is set up so that an example is created if no inputs are provided,
% but ignores the example and just processes the inputs if they are given.
%
% Inputs:
% NODES should be an Nx3 or Nx4 matrix with the format [ID X Y] or [ID X Y Z]
% where ID is an integer, and X, Y, Z are cartesian position coordinates)
% SEGMENTS should be an Mx3 matrix with the format [ID N1 N2]
% where ID is an integer, and N1, N2 correspond to node IDs from NODES list
% such that there is an [undirected] edge/segment between node N1 and node N2
% SID should be an integer in the node ID list corresponding with the starting node
% FID (optional) should be an integer in the node ID list corresponding with the finish
%
% Outputs:
% DIST is the shortest Euclidean distance
% If FID was specified, DIST will be a 1x1 double representing the shortest
% Euclidean distance between SID and FID along the map segments. DIST will have
% a value of INF if there are no segments connecting SID and FID.
% If FID was not specified, DIST will be a 1xN vector representing the shortest
% Euclidean distance between SID and all other nodes on the map. DIST will have
% a value of INF for any nodes that cannot be reached along segments of the map.
% PATH is a list of nodes containing the shortest route
% If FID was specified, PATH will be a 1xP vector of node IDs from SID to FID.
% NAN will be returned if there are no segments connecting SID to FID.
% If FID was not specified, PATH will be a 1xN cell of vectors representing the
% shortest route from SID to all other nodes on the map. PATH will have a value
% of NAN for any nodes that cannot be reached along the segments of the map.
%
% Example:
% dijkstra; % calculates shortest path and distance between two nodes
%           % on a map of randomly generated nodes and segments
%
% Author: Joseph Kirk
% Email: jdkirk630 at gmail dot com
% Release: 1.3
```

```

% Release Date: 5/18/07

if (nargin < 3) % SETUP
    % (GENERATE RANDOM EXAMPLE OF NODES AND SEGMENTS IF NOT GIVEN AS INPUTS)
    % Deleted since it is not relevant
else %-----
    % MAIN FUNCTION - DIJKSTRA'S ALGORITHM
    % initializations
    node_ids = nodes(:,1);
    [num_map_pts,cols] = size(nodes);
    table = sparse(num_map_pts,2);
    shortest_distance = Inf(num_map_pts,1);
    settled = zeros(num_map_pts,1);
    path = num2cell(NaN(num_map_pts,1));
    col = 2;
    pidx = find(start_id == node_ids);
    shortest_distance(pidx) = 0;
    table(pidx,col) = 0;
    settled(pidx) = 1;
    path(pidx) = {start_id};
    if (nargin < 4) % compute shortest path for all nodes
        while_cmd = 'sum(~settled) > 0';
    else % terminate algorithm early
        while_cmd = 'settled(zz) == 0';
        zz = find(finish_id == node_ids);
    end
    while eval(while_cmd)
        % update the table
        table(:,col-1) = table(:,col);
        table(pidx,col) = 0;
        % find neighboring nodes in the segments list
        neighbor_ids = [segments(node_ids(pidx) == segments(:,2),3);
            segments(node_ids(pidx) == segments(:,3),2)];
        % calculate the distances to the neighboring nodes and keep track of the paths
        for k = 1:length(neighbor_ids)
            cidx = find(neighbor_ids(k) == node_ids);
            if ~settled(cidx)
                d = sqrt(sum((nodes(pidx,2:cols) - nodes(cidx,2:cols)).^2));
                if (table(cidx,col-1) == 0) || ...
                    (table(cidx,col-1) > (table(pidx,col-1) + d))
                    table(cidx,col) = table(pidx,col-1) + d;
                    tmp_path = path(pidx);
                    path(cidx) = {[tmp_path{1} neighbor_ids(k)]};
                else
                    table(cidx,col) = table(cidx,col-1);
                end
            end
        end
        % find the minimum non-zero value in the table and save it
        nidx = find(table(:,col));
        ndx = find(table(nidx,col) == min(table(nidx,col)));
        if isempty(ndx)
            break
        else
            pidx = nidx(ndx(1));
            shortest_distance(pidx) = table(pidx,col);
            settled(pidx) = 1;
        end
    end
    if (nargin < 4) % return the distance and path arrays for all of the nodes
        dist = shortest_distance';
        path = path';
    else % return the distance and path for the ending node
        dist = shortest_distance(zz);
        path = path(zz);
        path = path{1};
    end
end

```

8.1.4. FindcurveNEW

```
function path=findcurveNEW(nodes,puntos4,edge,start_id,finish_id)
segments=zeros(length(edge.Cells),3);
id=0;
for i=1:length(edge.Cells)
    if (~isempty(find(puntos4==edge.Cells{i,2}{1})) & ~isempty(find(puntos4==edge.Cells{i,2}{2})))
        segments(i,:)=[id edge.Cells{i,2}{1} edge.Cells{i,2}{2}];
        id=id+1;
    end;
end;
disp('Nodes and segments created');
[dist,path] = dijkstra(nodes,segments,start_id,finish_id);
end
```

8.1.5. FindREGION

```
function [atria,cells,path] = findREGION (atria,edge,puntos,nodes,Ref,point1,point2,point3,dist,ID)
%Find trajectory of the opening
[path1]=findcurveNEW(nodes,puntos,edge,point1,point2);
[path2]=findcurveNEW(nodes,puntos,edge,point1,point3);
[path3]=findcurveNEW(nodes,puntos,edge,point2,point3);
path1=path1';
path2=path2';
path3=path3';
path=[path1;path2;path3];
disp('Path obtained');
%Find points that are a certain distance (dist) from the trajectory of the points in the opening
%For each of the points, find the ones that are the given distance dist
bueno=[];
for i=1:length(path)
    %Reduce the search region
    region=Ref (atria.Points(:,1)< atria.Points(path(i)+1,1)+1 & atria.Points(:,1)> atria.Points(path(i)+1,1)-1 & atria.Points(:,2)<
    atria.Points(path(i)+1,2)+1 & atria.Points(:,2)> atria.Points(path(i)+1,2)-1 & atria.Points(:,3)< atria.Points(path(i)+1,3)+1 &
    atria.Points(:,3)> atria.Points(path(i)+1,3)-1);
    [Dd,posd]=pdist2(atria.Points(path(i)+1,:),atria.Points(region(:)+1,:),'euclidean','Smallest',1);

    for j=1:length(Dd)
        if Dd(j)<dist & isempty(find(bueno==region(j)))
            bueno=[bueno;region(j)];
        end;
    end;
end;
%Find the cells that correspond to the obtained points
cells=[];
for i=1:length(bueno)
    X=find(atria.Cells(:,1)==bueno(i) | atria.Cells(:,2)==bueno(i) | atria.Cells(:,3)==bueno(i));
    cells=[cells; X];
end;
cells=unique(cells);
atria.CellData(3).Data(cells)=ID;
end
```

8.1.6 RegionPulmonary

```
function
[atria,cells,cells1,cells2,path,path7]=regionPulmonary(atria,edge,puntos,nodes,Ref,point1,point2,point3,point4,point5,point6,dist,
dist2,ID1,ID2,ID3)
%Find trajectory of the superior pulmonary vein edge
[path1]=findcurveNEW(nodes,puntos,edge,point1,point2);
[path2]=findcurveNEW(nodes,puntos,edge,point1,point3);
[path3]=findcurveNEW(nodes,puntos,edge,point2,point3);
path1=path1';
path2=path2';
path3=path3';
path=[path1;path2;path3];
disp('Path obtained');
```

```

%Find points that are a distance dist to the points in the trajectory found
bueno=[];
for i=1:length(path)
    region=Ref (atria.Points(:,1)< atria.Points(path(i)+1,1)+2 & atria.Points(:,1)> atria.Points(path(i)+1,1)-2 & atria.Points(:,2)<
    atria.Points(path(i)+1,2)+2 & atria.Points(:,2)> atria.Points(path(i)+1,2)-2 & atria.Points(:,3)< atria.Points(path(i)+1,3)+2 &
    atria.Points(:,3)> atria.Points(path(i)+1,3)-2);
    [Dd,posd]=pdist2(atria.Points(path(i)+1,:),atria.Points(region(:)+1,:),'euclidean','Smallest',1);
    for j=1:length(Dd)
        if Dd(j)<dist & isempty(find(bueno==region(j)))
            bueno=[bueno;region(j)];
        end;
    end;
end;

%Find trajectory of the inferior pulmonary vein edge
[path4]=findcurveNEW(nodes,puntos,edge,point4,point5);
[path5]=findcurveNEW(nodes,puntos,edge,point4,point6);
[path6]=findcurveNEW(nodes,puntos,edge,point5,point6);
path4=path4';
path5=path5';
path6=path6';
path7=[path4;path5;path6];
disp('Path obtained');
bueno1=[];
bueno2=[];
for i=1:length(path7)
    region=Ref (atria.Points(:,1)< atria.Points(path7(i)+1,1)+2 & atria.Points(:,1)> atria.Points(path7(i)+1,1)-2 & atria.Points(:,2)<
    atria.Points(path7(i)+1,2)+2 & atria.Points(:,2)> atria.Points(path7(i)+1,2)-2 & atria.Points(:,3)< atria.Points(path7(i)+1,3)+2 &
    atria.Points(:,3)> atria.Points(path7(i)+1,3)-2);
    [Dd,posd]=pdist2(atria.Points(path7(i)+1,:),atria.Points(region(:)+1,:),'euclidean','Smallest',1);
    for j=1:length(Dd)
        if Dd(j)<dist2 & isempty(find(bueno1==region(j))) & isempty(find(bueno2==region(j)))
            bueno1=[bueno1;region(j)];
        end;
        if Dd(j)<dist2 & isempty(find(bueno2==region(j))) & ~isempty(find(bueno1==region(j)))
            bueno2=[bueno2;region(j)];
        end;
    end;
end;

%Find the cells that correspond to the obtained pointsv
cells=[];
for i=1:length(bueno)
    X=find(atria.Cells(:,1)==bueno(i) | atria.Cells(:,2)==bueno(i) | atria.Cells(:,3)==bueno(i));
    cells=[cells; X];
end;
cells=unique(cells);
atria.CellData(3).Data(cells)=ID1;

cells1=[];
for i=1:length(bueno1)
    X=find(atria.Cells(:,1)==bueno1(i) | atria.Cells(:,2)==bueno1(i) | atria.Cells(:,3)==bueno1(i));
    cells1=[cells1; X];
end;
cells1=unique(cells1);
atria.CellData(3).Data(cells1)=ID2;

cells2=[];
for i=1:length(bueno2)
    X=find(atria.Cells(:,1)==bueno2(i) | atria.Cells(:,2)==bueno2(i) | atria.Cells(:,3)==bueno2(i));
    cells2=[cells2; X];
end;
cells2=unique(cells2);
atria.CellData(3).Data(cells2)=ID3;
end

```

8.1.7. FindCT

```

function [atria,cells] = findCT (atria,edge,puntos,nodes,puntosLeft,point1,point2,point3,dist,ID)
path1=findcurveNEW(nodes,puntos,edge,point1,point2);
path3=findcurveNEW(nodes,puntos,edge,point2,point3);
path1=path1';

```

```
path3=path3';
path=[path1;path3];
save('pathCT.mat','path');
disp('Path obtained');
bueno=[];
for i=1:length(path)
    region=puntosLeft(atria.Points(:,1)< atria.Points(path(i)+1,1)+2 & atria.Points(:,1)> atria.Points(path(i)+1,1)-2 & atria.Points(:,2)<
    atria.Points(path(i)+1,2)+2 & atria.Points(:,2)> atria.Points(path(i)+1,2)-2 & atria.Points(:,3)< atria.Points(path(i)+1,3)+2 &
    atria.Points(:,3)> atria.Points(path(i)+1,3)-2);
    [Dd,posd]=pdist2(atria.Points(path(i)+1,:),atria.Points(region(:)+1:),'euclidean','Smallest',1);

    for j=1:length(Dd)
        if Dd(j)<dist & isempty(find(region(j)==bueno))
            bueno=[bueno;region(j)];
        end;
    end;
end;

cells=[];
for i=1:length(bueno)
    X=find(atria.Cells(:,1)==bueno(i) | atria.Cells(:,2)==bueno(i) | atria.Cells(:,3)==bueno(i));
    cells=[cells; X];
end;
cells=unique(cells);
atria.CellData(3).Data(cells)=ID;
end
```

8.1.8. FindSurrounding

```
function [atria,cells] = findSurrounding (atria,Ref,path,puntos,dist)
%Find cells that are certain distance from the given cells
bueno=[];
region=puntos (Ref(:,1)< Ref(path,1)+2 & Ref(:,1)> Ref(path,1)-2 & Ref(:,2)< Ref(path,2)+2 & Ref(:,2)> Ref(path,2)-2 & Ref(:,3)<
Ref(path,3)+2 & Ref(:,3)> Ref(path,3)-2);
[Dd,posd]=pdist2(Ref(path,:),Ref(region(:)+1:),'euclidean','Smallest',1);
for j=1:length(Dd)
    if Dd(j)<dist & isempty(find(bueno==region(j)+1))
        bueno=[bueno;region(j)+1];
    end;
end;
cells=bueno;
end
```

8.1.9. Delete pectineal muscles from epicardium

```
atria=vtk2structReader('pectineos.vtk');
celdas=csvread('peceliminar.csv',1,0);
Cpec.IDs=celdas(:,1)+1;
Cpec.Points=celdas(:,5:7);
celdas=csvread('HIC.csv',1,0);
Chic.IDs=celdas(:,1)+1;
Chic.Points=celdas(:,4:6);
celdas=csvread('pared.csv',1,0);
Cpared.IDs=celdas(:,1)+1;
Cpared.Points=celdas(:,4:6);

[Dhich,posd]=pdist2(Chic.Points,Cpec.Points,'euclidean','Smallest',1);
[Dpared,posit]=pdist2(Cpared.Points,Cpec.Points,'euclidean','Smallest',1);
display('Distances obtained');
hic=[];
pared=[];
for i=1:length(Dhich)
    if Dhich(i)<Dpared(i)
        hic(i)=Cpec.IDs(i);
        atria.CellData(3).Data(Cpec.IDs(i))=35;
    else
end
```

```
pared(i)=Cpec.IDs(i);
atria.CellData(3).Data(Cpec.IDs(i))=37;
end
end
```

8.1.10. Mapping RA-LA and ORGANID into volume model

```
%% Mapping RA-LA and OrganID
%% Mapping from surface to volume RA-LA and ORGANID
% Reading surface and volume models
atriaV1=vtk2structReader('FINALISIMO 1403865.vtk');
atriaV2=vtk2structReader('volume 1403865.vtk');

% Reading centroids of the cells
celdas=csvread('centroids FINALISIMO.csv',1,0);
centroidesV1.Points=celdas(:,4:6);
celdas=csvread('centroids volume 1403865.csv',1,0);
centroidesV2.Points=celdas(:,1:3);

disp('Files read');

%Calculate proximity between cells of the two models
[D,I]=pdist2(centroidesV1.Points,centroidesV2.Points,'euclidean','Smallest',1);
I=I';
save('Icells.mat','I');

% Add RA-LA and ORGANID data to the volume model
atriaV2.CellData(2).Type= 'SCALARS';
atriaV2.CellData(2).Name= 'RA-LA';
atriaV2.CellData(2).Format= 'double';

atriaV2.CellData(3).Type= 'SCALARS';
atriaV2.CellData(3).Name= 'OrganID';
atriaV2.CellData(3).Format= 'double';

for i=1:atriaV2.NumCells
    atriaV2.CellData(2).Data(i)=atriaV1.CellData(2).Data(I(i));
end

for i=1:atriaV2.NumCells
    atriaV2.CellData(3).Data(i)=atriaV1.CellData(3).Data(I(i));
end

atriaV2.CellData(2).Data=atriaV2.CellData(2).Data';
atriaV2.CellData(3).Data=atriaV2.CellData(3).Data';
atriaV2.Field=[];

%% Create PointData RA-LA and ORGANID

%Calculate proximity between the centroids of the cells and the points of the volume model
[D,I]=pdist2(centroidesV2.Points,atriaV2.Points,'euclidean','Smallest',1);
I=I';
save('Ipoints.mat','I');

% Add PointData for RA-LA and ORGANID
atriaV2.PointData(3).Type= 'SCALARS';
atriaV2.PointData(3).Name= 'RA-LA';
atriaV2.PointData(3).Format= 'double';

atriaV2.PointData(4).Type= 'SCALARS';
atriaV2.PointData(4).Name= 'OrganID';
atriaV2.PointData(4).Format= 'double';

for i=1:atria.NumPoints
    atriaV2.PointData(3).Data(i)=atriaV2.CellData(2).Data(I(i));
end

for i=1:atria.NumPoints
    atriaV2.PointData(4).Data(i)=atriaV2.CellData(3).Data(I(i));
end
```

```
atriaV2.PointData(3).Data=atria.PointData(3).Data';
atriaV2.PointData(4).Data=atria.PointData(4).Data';

struct2vtkWriter(atriaV2,'folder','labelled volume ORGANID');
%% Needed for defining normals and fibers
[dist,pos]=pdist2(atriaV1.Points,centroidesV2.Points,'euclidean','Smallest',1);
save('pos.mat','pos');
```

8.1.11. Refine atrial volume model

```
%% Generate final ORGANID volume model before defining material, models, and fibers
%% Define final regions for the BB
posHB=find(atria.CellData(3).Data==26);
puntos=atria.Cells(posHB,:);
puntos2=[puntos{:,2}];
puntos3=unique(puntos2);
puntosHB=sort(puntos3);
puntosSurface=puntosHB((atria.PointData(2).Data(puntosHB+1)==1) & atria.PointData(4).Data(puntosHB+1)==26);
atria.PointData(4).Data(puntosSurface+1)=48;
Y=[];
points=atria.Cells{:,2};
points2=[points{:,1}];
for i=1:length(puntosSurface)
    [row,col]=find(points2==puntosSurface(i));
    Y=[Y;col];
end
layer=unique(Y);
layer=sort(layer);
layer2=layer(atria.CellData(3).Data(layer)==26);
atria.CellData(3).Data(layer2)=48;

puntos=atria.Cells(layer2,:);
puntos2=[puntos{:,2}];
puntos3=unique(puntos2);
puntosHB=sort(puntos3);
puntosSurface=puntosHB((atria.PointData(2).Data(puntosHB)==0) & atria.PointData(4).Data(puntosHB+1)==26);
atria.PointData(4).Data(puntosSurface+1)=48;
Y=[];
points=atria.Cells{:,2};
points2=[points{:,1}];
for i=1:length(puntosSurface)
    [row,col]=find(points2==puntosSurface(i));
    Y=[Y;col];
end
layer=unique(Y);
layer=sort(layer);
layer2=layer(atria.CellData(3).Data(layer)==26);
atria.CellData(3).Data(layer2)=48;

puntos=atria.Cells(layer2,:);
puntos2=[puntos{:,2}];
puntos3=unique(puntos2);
puntosHB=sort(puntos3);
puntosSurface=puntosHB((atria.PointData(2).Data(puntosHB)==0) & atria.PointData(4).Data(puntosHB+1)==26);
atria.PointData(4).Data(puntosSurface+1)=48;
Y=[];
points=atria.Cells{:,2};
points2=[points{:,1}];
for i=1:length(puntosSurface)
    [row,col]=find(points2==puntosSurface(i));
    Y=[Y;col];
end
layer=unique(Y);
layer=sort(layer);
layer2=layer(atria.CellData(3).Data(layer)==26);
atria.CellData(3).Data(layer2)=48;

atria.CellData(3).Data(atria.CellData(3).Data==48 & atria.CellData(2).Data==2)=1;
atria.PointData(4).Data(atria.PointData(4).Data==48 & atria.PointData(3).Data==2)=1;
```

```
atria.CellData(3).Data(atria.CellData(3).Data==26 & atria.CellData(2).Data==2)=2;
atria.PointData(4).Data(atria.PointData(4).Data==26 & atria.PointData(3).Data==2)=2;

%% Assign conductivity 0 (ORGANID=23) to cells that should not connect two regions
elementos=find(atria.CellData(3).Data==33 | atria.CellData(3).Data==18 | atria.CellData(3).Data==6);
elem=[];
for i=1:length(elementos)
    nodos1=atria.Cells(elementos(i),2);
    nodos=[nodos1{:},1];
    k33=[];
    k18=[];
    k6=[];
    for j=1:8
        if (atria.PointData(4).Data(nodos(j)+1) == 33)
            k33=1;
        end
        if (atria.PointData(4).Data(nodos(j)+1) == 18)
            k18=1;
        end
    end
end
if (k33==1 & k18==1)
    atria.CellData(3).Data(elementos(i))=23;
    elem=[elem;elementos(i)];
end
end

elementos=find(atria.PointData(4).Data==33 | atria.PointData(4).Data==18 | atria.PointData(4).Data==22);
elem=[];
cells=atria.Cells(:,2);
cells=[cells{:},1];
for i=1:length(elementos)

    [~,cellaim]=find(elementos(i)==cells);
    k33=[];
    k18=[];
    for j=1:length(cellaim)
        if (atria.CellData(3).Data(cellaim(j)+1) == 33)
            k33=1;
        end
        if (atria.CellData(3).Data(cellaim(j)+1) == 18)
            k18=1;
        end
    end
end
if (k33==1 & k18==1)
    atria.PointData(4).Data(elementos(i))=23;
    elem=[elem;elementos(i)];
end
end

struct2vtkWriter(atria, 'folder', 'volume final before mat mod');
```

8.1.12. Generate final atria volume model

```
% Code to generate the properties for ionic model and material, and add the fiber direction
close all
clear
clc
%% Read the volumen model labelled with RA-LA and ORGANID for both Point and Data
atria=vtk2structReader('volume labelled.vtk');
%% Define Material
atria.CellData(4).Type= 'SCALARS';
atria.CellData(4).Name= 'Material';
atria.CellData(4).Format= 'double';
atria.CellData(4).Data=zeros(atria.NumCells,1);

for i=1:atria.NumCells
    switch atria.CellData(3).Data(i)
        case {4,5,19,20,35,36,37}
            atria.CellData(4).Data(i)=1;
    end
end
```

```

case 15
    atria.CellData(4).Data(i)=2;
case {7,8,9,10,11,12,13,14}
    atria.CellData(4).Data(i)=3;
case {28,29,38,39,40,41,42,43,44,45,46,47,48}
    atria.CellData(4).Data(i)=4;
case 34
    atria.CellData(4).Data(i)=5;
case {21,6}
    atria.CellData(4).Data(i)=6;
case {23,26,2}
    atria.CellData(4).Data(i)=7;
case {17,18}
    atria.CellData(4).Data(i)=8;
case {3,16,31,32,33}
    atria.CellData(4).Data(i)=9;
case 22
    atria.CellData(4).Data(i)=10;
case {24,25,27,30,1}
    atria.CellData(4).Data(i)=11;
end
end

%% Define Ionic models
atria.PointData(5).Type= 'SCALARS';
atria.PointData(5).Name= 'Model';
atria.PointData(5).Format= 'double';
atria.PointData(5).Data=zeros(atria.NumPoints,1);

for i=1:atria.NumPoints
    switch atria.PointData(4).Data(i)
        case {35,5,20,21,22,23,34,6,17,18,36,37,38,39,40,41,42,43,44,45,46,47}
            atria.PointData(5).Data(i)=231;
        case {15,26,28,29,48}
            atria.PointData(5).Data(i)=232;
        case 4
            atria.PointData(5).Data(i)=233;
        case 19
            atria.PointData(5).Data(i)=234;
        case {31,32,33}
            atria.PointData(5).Data(i)=235;
        case 16
            atria.PointData(5).Data(i)=236;
        case {7,8,9,10,11,12,13,14}
            atria.PointData(5).Data(i)=237;
        case 3
            atria.PointData(5).Data(i)=238;
        case {24,25,27,30,2,1}
            atria.PointData(5).Data(i)=239;
    end
end

%*****
% Generate fibers
%*****
atriaS=vtk2structReader('FINALISIMO 3014094.vtk'); % Surface mesh with ORGANID
% Centroids of the elements in the volume mesh
A=importdata('centroides modelo etiquetado 5.csv',';',1);
centroidesV=A.data(:,2:4);
% Calculate the normal of the surface mesh
TRI_atria=atriaS.Cells + 1;
P_atria=atriaS.Points;
TR_atria=triangulation(TRI_atria,P_atria);
N_atria=vertexNormal(TR_atria, (1:double(atriaS.NumPoints))');
%Find the elements in the mesh volume closest to the nodes in the surface mesh
[dist,pos]=pdist2(atriaS.Points,centroidesV,'euclidean','Smallest',1);
% Assign the normal of the nodes of the surface mesh to the elements of the volume mesh
normales=zeros(atria.NumCells,3); % definimos la longitud del vector
for i=1:atria.NumCells
    nodo=pos(i);
    normales(i,:)=N_atria(nodo,:);
end

```

```
end
%save('Normales_3014094.mat','normales')
% Save properties of the normals
atria.CellData(5).Name= 'Normals';
atria.CellData(5).Format= 'float';
atria.CellData(5).Type= 'VECTORS';
atria.CellData(5).Data= normales;
% Obtain the directives of the fibers for each ORGANID region
DR=importdata('Directriz_Regiones_3014094.xlsx');
dir=zeros(max(DR.data(:,10)),3);
myO=DR.data(:,10);
for i=1:length(DR.data(:,1))
    P1=[DR.data(i,3),DR.data(i,4),DR.data(i,5)];
    P2=[DR.data(i,6),DR.data(i,7),DR.data(i,8)];
    dis=P2-P1;
    dis=dis/norm(dis);
    dir(myO(i,:))=dis;
end

longitudinal=[1,2,6,22,23,26,48]; % Regions with fiber direction = directive

fibra=zeros(atria.NumCells,3);
fibra2=zeros(atria.NumCells,3);
normales2=zeros(atria.NumCells,3);
% Calculate the direction of the fiber for each element
for i=1:atria.NumCells
    normales2(i,:)=normales(i,:)/norm(normales(i,:)); % Vector unitario de las normales
    OrganID=atria.CellData(3).Data(i);
    if ismember(OrganID,longitudinal) % Fibra=directriz
        fibra(i,:)= dir(OrganID,:);
        fibra2(i,:)= dir(OrganID,:);
    else
        t=cross(dir(OrganID,:),normales(i,:)); % Dirección de la fibra= directriz x normal
        fibra(i,:)=t;
        fibra2(i,:)=t/norm(t); % Vector unitario de dirección de la fibra normalizada
    end
end

% Save the property of the fibers
atria.CellData(6).Name= 'Fibres';
atria.CellData(6).Format= 'float';
atria.CellData(6).Type= 'VECTORS';
atria.CellData(6).Data= fibra2;
% Save the mesh with all properties: ORGANID, normals, models, materials
% and fibers
struct2vtkWriter(atria,'folder','AllProperties');
```

CHAPTER 9. REFERENCES

- [1] A. C. Guyton, "T E X T B O O K of Medical Physiology."
- [2] G. A. Thibodeau and K. T. Patton, *Anatomía y fisiología*. Ediciones Harcourt, 2000.
- [3] K. Wang, S. Y. Ho, D. G. Gibson, and R. H. Anderson, "Architecture of atrial musculature in humans.," *Br. Heart J.*, vol. 73, no. 6, p. 559, Jun. 1995.
- [4] R. H. Anderson and A. C. Cook, "The structure and components of the atrial chambers," *Europace*, vol. 9, no. Supplement 6, pp. vi3-vi9, Nov. 2007.
- [5] A. Ferrer *et al.*, "Detailed anatomical and electrophysiological models of human atria and torso for the simulation of atrial activation," *PLoS One*, vol. 10, no. 11, pp. 1–29, 2015.
- [6] D. Sánchez-Quintana, G. Pizarro, J. R. López-Mínguez, S. Y. Ho, and J. A. Cabrera, "Standardized Review of Atrial Anatomy for Cardiac Electrophysiologists," *J. Cardiovasc. Transl. Res.*, vol. 6, no. 2, pp. 124–144, Apr. 2013.
- [7] P. G. PLATONOV, V. IVANOV, S. Y. HO, and L. MITROFANOVA, "Left Atrial Posterior Wall Thickness in Patients with and without Atrial Fibrillation: Data from 298 Consecutive Autopsies," *J. Cardiovasc. Electrophysiol.*, vol. 19, no. 7, pp. 689–692, Jul. 2008.
- [8] B. Hall, V. Jeevanantham, R. Simon, J. Filippone, G. Vorobiof, and J. Daubert, "Variation in left atrial transmural wall thickness at sites commonly targeted for ablation of atrial fibrillation," *J. Interv. Card. Electrophysiol.*, vol. 17, no. 2, pp. 127–132, Mar. 2007.
- [9] K. Otomo, K. Uno, H. Fujiwara, M. Isobe, and Y. Iesaka, "Local unipolar and bipolar electrogram criteria for evaluating the transmural of atrial ablation lesions at different catheter orientations relative to the endocardial surface," *Heart. Rhythm*, vol. 7, no. 9, pp. 1291–1300, Sep. 2010.
- [10] P. Neher *et al.*, "Automatic Segmentation of Cardiac CTs - Personalized Atrial Models Augmented with Electrophysiological Structures," Springer, Berlin, Heidelberg, 2011, pp. 80–87.
- [11] C. A. RUIZ VILLA, "Estudio de la vulnerabilidad a reentradas a través de modelos matemáticos y simulación de la aurícula humana," Universitat Politècnica de València, Valencia (Spain), 2010.
- [12] C. Tobón Zuluaga, "Modelización y evaluación de factores que favorecen las arritmias auriculares y su tratamiento mediante técnicas quirúrgicas. Estudio de simulación," Universitat Politècnica de València, Valencia (Spain), 2010.
- [13] R. M. Negoescu, "Shift Of Sinoatrial True Pacemaker Under Autonomic Drive In Man," in *Proceedings of the Annual International Conference of the IEEE Engineering in Medicine and Biology Society Volume 13: 1991*, pp. 2321–2322.
- [14] M. J. Weigner, S. E. Katz, P. S. Douglas, and W. J. Manning, "Left atrial appendage anatomy and function: short term response to sustained atrial fibrillation," *Heart*, vol. 82, no. 5, pp. 555–558, Nov. 1999.
- [15] G. I. Cohen *et al.*, "Reference values for normal adult transesophageal echocardiographic

-
- measurements.," *J. Am. Soc. Echocardiogr.*, vol. 8, no. 3, pp. 221–30.
- [16] M. Akcay, E. S. Bilen, M. Bilge, T. Durmaz, and M. Kurt, "Prominent Crista Terminalis: As An Anatomic Structure Leading to Atrial Arrhythmias and Mimicking Right Atrial Mass," *J. Am. Soc. Echocardiogr.*, vol. 20, no. 2, p. 197.e9-197.e10, Feb. 2007.
- [17] F. Sunderman, *Normal values in clinical medicine*. Philadelphia: W.B. Saunders, 1949.
- [18] J L Coffey, M Cristy, and G G Warner, "Specific absorbed fractions for photon sources uniformly distributed in the heart chambers and heart wall of a heterogenous phantom | J L Coffey," 1981.
- [19] T. MATSUYAMA *et al.*, "Anatomical diversity and age-related histological changes in the human right atrial posterolateral wall," *Europace*, vol. 6, no. 4, pp. 307–315, Jul. 2004.
- [20] A. Hiraoka, S. Karakawa, T. Yamagata, H. Matsuura, and G. Kajiyama, "Structural characteristics of Koch's triangle in patients with atrioventricular node reentrant tachycardia," *Hiroshima J. Med. Sci.*, vol. 47, no. 1, pp. 7–15, Mar. 1998.
- [21] D. W. Kitzman, D. G. Scholz, P. T. Hagen, D. M. Ilstrup, and W. D. Edwards, "Age-related changes in normal human hearts during the first 10 decades of life. Part II (Maturity): A quantitative anatomic study of 765 specimens from subjects 20 to 99 years old.," *Mayo Clin. Proc.*, vol. 63, no. 2, pp. 137–46, Feb. 1988.
- [22] S. Y. Ho, D. Sanchez-Quintana, J. A. Cabrera, and R. H. Anderson, "Anatomy of the left atrium: implications for radiofrequency ablation of atrial fibrillation.," *J. Cardiovasc. Electrophysiol.*, vol. 10, no. 11, pp. 1525–33, Nov. 1999.
- [23] W. Bommer, L. Weinert, A. Neumann, J. Neef, D. T. Mason, and A. DeMaria, "Determination of right atrial and right ventricular size by two-dimensional echocardiography.," *Circulation*, vol. 60, no. 1, pp. 91–100, Jul. 1979.
- [24] J. A. Cabrera, D. Sanchez-Quintana, S. Y. Ho, A. Medina, and R. H. Anderson, "The architecture of the atrial musculature between the orifice of the inferior caval vein and the tricuspid valve: the anatomy of the isthmus.," *J. Cardiovasc. Electrophysiol.*, vol. 9, no. 11, pp. 1186–95, Nov. 1998.
- [25] J. Reig, R. Mirapeix, A. Jornet, and M. Petit, "Morphologic characteristics of the fossa ovalis as an anatomic basis for transseptal catheterization," *Surg. Radiol. Anat.*, vol. 19, no. 5, pp. 279–282, Sep. 1997.
- [26] R. Lemery, G. Guiraudon, and J. P. Veinot, "Anatomic description of Bachmann's bundle and its relation to the atrial septum.," *Am. J. Cardiol.*, vol. 91, no. 12, pp. 1482–5, A8, Jun. 2003.
- [27] A. J. M. D. Chandrasekhar, H.V.M.D. & Chandrasekhar, "Radiological Anatomy of Heart and Vessels in Thorax," 2012. [Online]. Available: http://www.meddean.luc.edu/lumen/MedEd/Radio/curriculum/Vascular/Structure_Vessels_thorax_f.htm.
- [28] A. FERRER ALBERO, "Three-dimensional Multiscale Modelling and Simulation of Atria and Torso Electrophysiology," no. July, 2017.
- [29] "Tissues and Organs - Fundamentals - Merck Manuals Consumer Version." [Online]. Available: <https://www.merckmanuals.com/home/fundamentals/the-human-body/tissues-and-organs>. [Accessed: 03-Jul-2019].
- [30] "Seniors Center - Penn State Hershey Medical Center - Kidney function - Penn State Hershey Medical Center." [Online]. Available: <http://pennstatehershey.adam.com/content.aspx?productId=113&pid=2&gid=19615>.

[Accessed: 03-Jul-2019].

- [31] F. Mas Milian, R. Kramer, and C. Alberto Brayner de Oliveira Lira, "Standing adult human phantoms based on 10th, 50th and 90th mass and height percentiles of male and female Caucasian populations Prostatic artery embolization View project Treatment Planning System Ion Therapy (TPS) View project Vagner Ferreira Cassola," *Artic. Phys. Med. Biol.*, 2011.
- [32] J.-F. Bellemare, M.-P. Cordeau, P. Leblanc, and F. Bellemare, "Thoracic Dimensions at Maximum Lung Inflation in Normal Subjects and in Patients With Obstructive and Restrictive Lung Diseases," *Chest*, vol. 119, no. 2, pp. 376–386, Feb. 2001.
- [33] F. H. DeLand and W. A. North, "Relationship Between Liver Size and Body Size," *Radiology*, vol. 91, no. 6, pp. 1195–1198, Dec. 1968.
- [34] G. H. Kramer, K. Capello, B. Bearrs, A. Lauzon, and L. Normandeau, "LINEAR DIMENSIONS AND VOLUMES OF HUMAN LUNGS OBTAINED FROM CT IMAGES," *Health Phys.*, vol. 102, no. 4, pp. 378–383, Apr. 2012.
- [35] I. Busscher, J. J. W. Ploegmakers, G. J. Verkerke, and A. G. Veldhuizen, "Comparative anatomical dimensions of the complete human and porcine spine," *Eur. Spine J.*, vol. 19, no. 7, pp. 1104–1114, Jul. 2010.
- [36] R. Selthofer *et al.*, "Morphometric analysis of the sternum.," *Coll. Antropol.*, vol. 30, no. 1, pp. 43–7, Mar. 2006.
- [37] P. Colli Franzone, L. F. Pavarino, and S. Scacchi, *Mathematical Cardiac Electrophysiology*, vol. 13. Cham: Springer International Publishing, 2014.
- [38] R. B. Shepard, "Stimulation and Excitation of Cardiac Tissues," *Clin. Card. Pacing, Defibrillation Resynchronization Ther.*, pp. 61–113, Jan. 2017.
- [39] K. E. Barrett, S. M. Barman, S. Boitano, and H. Brooks, "Ranges of Normal Values in Human Whole Blood (B), Plasma (P), or Serum (S)a Normal Value (Varies with Procedure Used) Determination Traditional Units SI Units Normal Value (Varies with Procedure Used)."
- [40] Z. G. Wang, L. C. Pelletier, M. Talajic, and S. Nattel, "Effects of flecainide and quinidine on human atrial action potentials. Role of rate-dependence and comparison with guinea pig, rabbit, and dog tissues.," *Circulation*, vol. 82, no. 1, pp. 274–283, Jul. 1990.
- [41] A.J. Pullan, M.L. Buist, and L.K. Cheng, "Mathematically modelling the electrical activity of the heart: From cell to body surface and back again | A.J. Pullan." [Online]. Available: https://www.researchgate.net/publication/310628318_Mathematically_modelling_the_electrical_activity_of_the_heart_From_cell_to_body_surface_and_back_again. [Accessed: 03-Jul-2019].
- [42] "Proyecto ITACA." [Online]. Available: <https://www.itaca.edu.es/cardiac-action-potential.htm>. [Accessed: 03-Jul-2019].
- [43] H. Ni, I. Adeniran, and H. Zhang, "In-silico investigations of the functional impact of KCNA5 mutations on atrial mechanical dynamics," *J. Mol. Cell. Cardiol.*, vol. 111, pp. 86–95, Oct. 2017.
- [44] W. Einthoven, G. Fahr, and A. de Waart, "On the direction and manifest size of the variations of potential in the human heart and on the influence of the position of the heart on the form of the electrocardiogram," *Am. Heart J.*, vol. 40, no. 2, pp. 163–211, Aug. 1950.
- [45] *Chou's Electrocardiography in Clinical Practice*. Elsevier, 2008.

-
- [46] S. D. Carley, "Beyond the 12 lead: Review of the use of additional leads for the early electrocardiographic diagnosis of acute myocardial infarction," *Emerg. Med. Australas.*, vol. 15, no. 2, pp. 143–154, Apr. 2003.
- [47] D. D. Finlay, C. D. Nugent, P. J. McCullagh, and N. D. Black, "Mining for diagnostic information in body surface potential maps: A comparison of feature selection techniques," *Biomed. Eng. Online*, vol. 4, no. 1, p. 51, Sep. 2005.
- [48] J. R. Fitz-Clarke, J. L. Sapp, J. W. Warren, J. C. Clements, and B. M. Horáček, "Body surface potential mapping and computer simulation of human ventricular fibrillation," *undefined*, 2006.
- [49] N. Saoudi, "A classification of atrial flutter and regular atrial tachycardia according to electrophysiological mechanisms and anatomical bases. A Statement from a Joint Expert Group from the Working Group of Arrhythmias of the European Society of Cardiology and the North American Society of Pacing and Electrophysiology," *Eur. Heart J.*, vol. 22, no. 14, pp. 1162–1182, Jul. 2001.
- [50] Javier E. Banchs, "Atrial Tachycardia: Diagnosis and Treatment - The Cardiology Advisor." [Online]. Available: <https://www.thecardiologyadvisor.com/home/decision-support-in-medicine/cardiology/atrial-tachycardia-diagnosis-and-treatment/>. [Accessed: 03-Jul-2019].
- [51] G. Steinbeck and E. Hoffmann, "'True' atrial tachycardia.," *Eur. Heart J.*, vol. 19 Suppl E, pp. E10-2, E48-9, May 1998.
- [52] F. García-Cosío, A. Pastor Fuentes, and A. Núñez Angulo, "Clinical Approach to Atrial Tachycardia and Atrial Flutter From an Understanding of the Mechanisms. Electrophysiology Based on Anatomy," *Rev. Española Cardiol. (English Ed.)*, vol. 65, no. 4, pp. 363–375, 2012.
- [53] F. Anselme, "Macroreentrant atrial tachycardia: Pathophysiological concepts," *Hear. Rhythm*, vol. 5, no. 6, pp. S18–S21, 2008.
- [54] M. Zoni-Berisso, F. Lercari, T. Carazza, and S. Domenicucci, "Epidemiology of atrial fibrillation: European perspective," *Clin. Epidemiol.*, vol. 6, p. 213, Jun. 2014.
- [55] S. Bellet, *Clinical disorders of the heart beat*. Lea & Febiger, 1971.
- [56] J. Jalife, "Rotors and Spiral Waves in Atrial Fibrillation," *J. Cardiovasc. Electrophysiol.*, vol. 14, no. 7, pp. 776–780, Jul. 2003.
- [57] M. Haïssaguerre *et al.*, "Spontaneous Initiation of Atrial Fibrillation by Ectopic Beats Originating in the Pulmonary Veins," *N. Engl. J. Med.*, vol. 339, no. 10, pp. 659–666, Sep. 1998.
- [58] C. Sanchez, "Multiscale Analysis of Atrial Fibrillation Mechanisms," no. April, p. 200, 2014.
- [59] J. E. P. Waktare, "Atrial Fibrillation," *Circulation*, vol. 106, no. 1, pp. 14–16, Jul. 2002.
- [60] R. Goel, K. Srivathsan, and M. Mookadam, "Supraventricular and Ventricular Arrhythmias," *Prim. Care Clin. Off. Pract.*, vol. 40, no. 1, pp. 43–71, Mar. 2013.
- [61] P. Kirchhof *et al.*, "2016 ESC Guidelines for the management of atrial fibrillation developed in collaboration with EACTS," *Eur. Heart J.*, vol. 37, no. 38, pp. 2893–2962, Oct. 2016.
- [62] M.A. Allesie, Willem Lammers, and F.I.M. Bonke, "Experimental evaluation of Moe's multiple wavelet hypothesis of atrial fibrillation. In: Cardiac electrophysiology and arrhythmias | M.A. Allesie | Request PDF."

- [63] R. Mandapati, A. Skanes, J. Chen, O. Berenfeld, and J. Jalife, "Stable microreentrant sources as a mechanism of atrial fibrillation in the isolated sheep heart.," *Circulation*, vol. 101, no. 2, pp. 194–9, Jan. 2000.
- [64] M. Yamazaki *et al.*, "Heterogeneous atrial wall thickness and stretch promote scroll waves anchoring during atrial fibrillation," *Cardiovasc. Res.*, vol. 94, no. 1, pp. 48–57, Apr. 2012.
- [65] S. M. Narayan, D. E. Krummen, K. Shivkumar, P. Clopton, W.-J. Rappel, and J. M. Miller, "Treatment of Atrial Fibrillation by the Ablation of Localized Sources," *J. Am. Coll. Cardiol.*, vol. 60, no. 7, pp. 628–636, Aug. 2012.
- [66] J. Luis Merino, "Mecanismos electrofisiológicos y diagnóstico de la fibrilación auricular," *Rev. Española Cardiol. Supl.*, vol. 16, pp. 12–19, Jan. 2016.
- [67] "INFORMACIÓN PARA EL PACIENTE GUÍA PARA FIBRILACIÓN AURICULAR - PDF." [Online]. Available: <https://docplayer.es/10112847-Informacion-para-el-paciente-guia-para-fibrilacion-auricular.html>. [Accessed: 03-Jul-2019].
- [68] S. Rocher Ventura, "DESARROLLO DE UN MODELO COMPUTACIONAL REALISTA 3D DE LA AURICULA," 2016.
- [69] R. Caballero *et al.*, "In Humans, Chronic Atrial Fibrillation Decreases the Transient Outward Current and Ultrarapid Component of the Delayed Rectifier Current Differentially on Each Atria and Increases the Slow Component of the Delayed Rectifier Current in Both," *J. Am. Coll. Cardiol.*, vol. 55, no. 21, pp. 2346–2354, 2010.
- [70] A. J. Workman, K. A. Kane, and A. C. Rankin, "The contribution of ionic currents to changes in refractoriness of human atrial myocytes associated with chronic atrial fibrillation.," *Cardiovasc. Res.*, vol. 52, no. 2, pp. 226–35, Nov. 2001.
- [71] R. Bosch, "Ionic mechanisms of electrical remodeling in human atrial fibrillation," *Cardiovasc. Res.*, vol. 44, no. 1, pp. 121–131, Oct. 1999.
- [72] M. C. Wijffels, C. J. Kirchhof, R. Dorland, and M. A. Allesie, "Atrial fibrillation begets atrial fibrillation. A study in awake chronically instrumented goats.," *Circulation*, vol. 92, no. 7, pp. 1954–68, Oct. 1995.
- [73] A. Boldt *et al.*, "Fibrosis in left atrial tissue of patients with atrial fibrillation with and without underlying mitral valve disease," *Heart*, vol. 90, no. 4, pp. 400–405, Apr. 2004.
- [74] N. Ellinwood, D. Dobrev, S. Morotti, and E. Grandi, "In Silico Assessment of Efficacy and Safety of IKur Inhibitors in Chronic Atrial Fibrillation: Role of Kinetics and State-Dependence of Drug Binding.," *Front. Pharmacol.*, vol. 8, p. 799, 2017.
- [75] L. MARTÍNEZ MATEU, "Mapping of the electrical activity of human atria. Multiscale modelling and simulations," 2018.
- [76] D. R. Van Wagoner, A. L. Pond, M. Lamorgese, S. S. Rossie, P. M. McCarthy, and J. M. Nerbonne, "Atrial L-type Ca²⁺ currents and human atrial fibrillation.," *Circ. Res.*, vol. 85, no. 5, pp. 428–36, Sep. 1999.
- [77] M. Skasa, E. Jüngling, E. Picht, F. Schöndube, and A. Lückhoff, "L-type calcium currents in atrial myocytes from patients with persistent and non-persistent atrial fibrillation," *Basic Res. Cardiol.*, vol. 96, no. 2, pp. 151–159, Mar. 2001.
- [78] D. Dobrev *et al.*, "Molecular Basis of Downregulation of G-Protein–Coupled Inward Rectifying K⁺ Current (I_{K,ACh}) in Chronic Human Atrial Fibrillation," *Circulation*, vol. 104, no. 21, pp. 2551–2557, Nov. 2001.

-
- [79] D. Dobrev, "Human inward rectifier potassium channels in chronic and postoperative atrial fibrillation," *Cardiovasc. Res.*, vol. 54, no. 2, pp. 397–404, May 2002.
- [80] N. Voigt *et al.*, "Left-to-Right Atrial Inward Rectifier Potassium Current Gradients in Patients With Paroxysmal Versus Chronic Atrial Fibrillation," *Circ. Arrhythmia Electrophysiol.*, vol. 3, no. 5, pp. 472–480, Oct. 2010.
- [81] D. R. Van Wagoner, A. L. Pond, P. M. McCarthy, J. S. Trimmer, and J. M. Nerbonne, "Outward K⁺ current densities and Kv1.5 expression are reduced in chronic human atrial fibrillation," *Circ. Res.*, vol. 80, no. 6, pp. 772–81, Jun. 1997.
- [82] M. C. Brandt, L. Priebe, T. Böhle, M. Südkamp, and D. J. Beuckelmann, "The Ultrarapid and the Transient Outward K⁺ Current in Human Atrial Fibrillation. Their Possible Role in Postoperative Atrial Fibrillation," *J. Mol. Cell. Cardiol.*, vol. 32, no. 10, pp. 1885–1896, Oct. 2000.
- [83] "CT Scan." [Online]. Available: <https://www.mayoclinic.org/tests-procedures/ct-scan/about/pac-20393675>.
- [84] "Heart CT Scan: Purpose, Risks, and Procedure." [Online]. Available: <https://www.healthline.com/health/heart-ct-scan#purpose>. [Accessed: 03-Jul-2019].
- [85] "Diagnosing Heart Disease With Cardiac Computed Tomography (CT)." [Online]. Available: <https://www.webmd.com/heart-disease/guide/ct-heart-scan#1>. [Accessed: 03-Jul-2019].
- [86] "Radiation risk from medical imaging - Harvard Health." [Online]. Available: <https://www.health.harvard.edu/cancer/radiation-risk-from-medical-imaging>. [Accessed: 03-Jul-2019].
- [87] O. Dössel, M. W. Krueger, F. M. Weber, M. Wilhelms, and G. Seemann, "Computational modeling of the human atrial anatomy and electrophysiology," *Med. Biol. Eng. Comput.*, vol. 50, no. 8, pp. 773–799, Aug. 2012.
- [88] A. L. HODGKIN and A. F. HUXLEY, "A quantitative description of membrane current and its application to conduction and excitation in nerve.," *J. Physiol.*, vol. 117, no. 4, pp. 500–44, Aug. 1952.
- [89] D. NOBLE, "Cardiac Action and Pacemaker Potentials based on the Hodgkin-Huxley Equations," *Nature*, vol. 188, no. 4749, pp. 495–497, Nov. 1960.
- [90] M. Courtemanche, R. J. Ramirez, and S. Nattel, "Ionic mechanisms underlying human atrial action potential properties: insights from a mathematical model," *Am. J. Physiol. Circ. Physiol.*, vol. 275, no. 1, pp. H301–H321, Jul. 1998.
- [91] A. Nygren *et al.*, "Mathematical Model of an Adult Human Atrial Cell," *Circ. Res.*, vol. 82, no. 1, pp. 63–81, Jan. 1998.
- [92] M. M. Maleckar, J. L. Greenstein, W. R. Giles, and N. A. Trayanova, "Electrotonic coupling between human atrial myocytes and fibroblasts alters myocyte excitability and repolarization.," *Biophys. J.*, vol. 97, no. 8, pp. 2179–90, Oct. 2009.
- [93] E. Grandi *et al.*, "Human Atrial Action Potential and Ca²⁺ Model," *Circ. Res.*, vol. 109, no. 9, pp. 1055–1066, Oct. 2011.
- [94] J. T. Koivumäki, T. Korhonen, and P. Tavi, "Impact of Sarcoplasmic Reticulum Calcium Release on Calcium Dynamics and Action Potential Morphology in Human Atrial Myocytes: A Computational Study," *PLoS Comput. Biol.*, vol. 7, no. 1, p. e1001067, Jan. 2011.

-
- [95] M. Wilhelms, H. Hettmann, M. M. Maleckar, J. T. Koivumäki, O. Dössel, and G. Seemann, "Benchmarking electrophysiological models of human atrial myocytes," *Front. Physiol.*, vol. 3, p. 487, Jan. 2013.
- [96] C. S. H. ; David M. Harrild, Craig S. Henrique, "A Computer Model of Normal Conduction in the Human Atria," *Circ. Res.*, vol. 87, no. 7, Sep. 2000.
- [97] D. B. Geselowitz and W. T. Miller, "A bidomain model for anisotropic cardiac muscle.," *Ann. Biomed. Eng.*, vol. 11, no. 3–4, pp. 191–206, 1983.
- [98] Elvio A Heidenreich, J. Félix, R. Matas, and J. M. Ferrero Y De Loma-Ororio, "ALGORITMOS PARA ECUACIONES DE REACCIÓN REACCIÓN REACCIÓN DIFUSIÓN DIFUSIÓN DIFUSIÓN APLICADOS A ELECTROFISIOLOGÍA ELECTROFISIOLOGÍA ELECTROFISIOLOGÍA."
- [99] "Principales causas de muerte por grupos de enfermedades 1."
- [100] H. Calkins *et al.*, "2012 HRS/EHRA/ECAS expert consensus statement on catheter and surgical ablation of atrial fibrillation: recommendations for patient selection, procedural techniques, patient management and follow-up, definitions, endpoints, and research trial design," *J. Interv. Card. Electrophysiol.*, vol. 33, no. 2, pp. 171–257, Mar. 2012.
- [101] S. M. Narayan, D. E. Krummen, K. Shivkumar, P. Clopton, W.-J. Rappel, and J. M. Miller, "Treatment of Atrial Fibrillation by the Ablation of Localized Sources," *J. Am. Coll. Cardiol.*, vol. 60, no. 7, pp. 628–636, Aug. 2012.
- [102] E. Buch *et al.*, "Long-term clinical outcomes of focal impulse and rotor modulation for treatment of atrial fibrillation: A multicenter experience," *Heart. Rhythm*, vol. 13, no. 3, pp. 636–641, Mar. 2016.
- [103] J. Mayourian, E. A. Sobie, and K. D. Costa, "An Introduction to Computational Modeling of Cardiac Electrophysiology and Arrhythmogenicity," in *Methods in molecular biology (Clifton, N.J.)*, vol. 1816, 2018, pp. 17–35.
- [104] N. A. Trayanova *et al.*, "Computational cardiology: how computer simulations could be used to develop new therapies and advance existing ones.," *Europace*, vol. 14 Suppl 5, no. Suppl 5, pp. v82–v89, Nov. 2012.
- [105] M. W. Krüger, *Personalized Multi-Scale Modeling of the Atria: Heterogeneities, Fiber Architecture, Hemodialysis and Ablation Therapy*, vol. 19 de Karl. 2013.
- [106] H. Ni, S. Morotti, and E. Grandi, "A Heart for Diversity: Simulating Variability in Cardiac Arrhythmia Research," *Front. Physiol.*, vol. 9, p. 958, Jul. 2018.
- [107] "Seg3D." [Online]. Available: <http://www.sci.utah.edu/cibc-software/seg3d.html>. [Accessed: 03-Jul-2019].
- [108] J. Tate, B. Burton, and A. Khan, "Seg3D Basic Functionality," pp. 1–54.
- [109] C. Roberto Velert, "DISEÑO DE UNA METODOLOGIA PARA EL DESARROLLO DE MODELOS AURICULARES PERSONALIZADOS," 2017.
- [110] M. W. Krueger *et al.*, "Modeling Atrial Fiber Orientation in Patient-Specific Geometries : A Semi-automatic Rule-Based Approach," pp. 223–232.
- [111] Joseph Kirk, "Dijkstra's Shortest Path Algorithm - File Exchange - MATLAB Central." [Online]. Available: <https://es.mathworks.com/matlabcentral/fileexchange/12850-dijkstra-s-shortest-path-algorithm>. [Accessed: 03-Jul-2019].
- [112] "Distene's MeshGems suite | Meshing Software Components for CAD and CAE applications from Distene." [Online]. Available: <http://www.meshgems.com/>. [Accessed: 14-Jul-2019].

-
- [113] “Gmsh: a three-dimensional finite element mesh generator with built-in pre- and post-processing facilities.” [Online]. Available: <http://gmsh.info/>. [Accessed: 14-Jul-2019].
- [114] H. Si, “TetGen, a Delaunay-Based Quality Tetrahedral Mesh Generator,” *ACM Trans. Math. Softw.*, vol. 41, no. 2, pp. 1–36, Feb. 2015.
- [115] C. H. Luo and Y. Rudy, “A dynamic model of the cardiac ventricular action potential. I. Simulations of ionic currents and concentration changes,” *Circ. Res.*, vol. 74, no. 6, pp. 1071–96, Jun. 1994.
- [116] “Courtemanche, Ramirez, Nattel, 1998 — Physiome Model Repository.” [Online]. Available: <https://models.cellml.org/exposure/0e03bbe01606be5811691f9d5de10b65>. [Accessed: 03-Jul-2019].
- [117] M. W. Krueger *et al.*, “In-silico modeling of atrial repolarization in normal and atrial fibrillation remodeled state,” *Med. Biol. Eng. Comput.*, vol. 51, no. 10, pp. 1105–1119, Oct. 2013.
- [118] C. Tobón, C. A. Ruiz-Villa, E. Heidenreich, L. Romero, F. Hornero, and J. Saiz, “A Three-Dimensional Human Atrial Model with Fiber Orientation. Electrograms and Arrhythmic Activation Patterns Relationship,” *PLoS One*, vol. 8, no. 2, p. e50883, Feb. 2013.
- [119] G. Seemann, C. Höper, F. B. Sachse, O. Dössel, A. V Holden, and H. Zhang, “Heterogeneous three-dimensional anatomical and electrophysiological model of human atria,” *Philos. Trans. R. Soc. A Math. Phys. Eng. Sci.*, vol. 364, no. 1843, pp. 1465–1481, Jun. 2006.
- [120] M. Courtemanche, R. J. Ramirez, and S. Nattel, “Ionic targets for drug therapy and atrial fibrillation-induced electrical remodeling: insights from a mathematical model,” *Cardiovasc. Res.*, vol. 42, no. 2, pp. 477–89, May 1999.
- [121] M. A. Colman *et al.*, “Pro-arrhythmogenic effects of atrial fibrillation-induced electrical remodeling: insights from the three-dimensional virtual human atria,” *J. Physiol.*, vol. 591, no. 17, pp. 4249–4272, Sep. 2013.
- [122] E. A. Heidenreich, J. M. Ferrero, M. Doblaré, and J. F. Rodríguez, “Adaptive Macro Finite Elements for the Numerical Solution of Monodomain Equations in Cardiac Electrophysiology,” *Ann. Biomed. Eng.*, vol. 38, no. 7, pp. 2331–2345, Jul. 2010.
- [123] R. LEMERY *et al.*, “Normal Atrial Activation and Voltage During Sinus Rhythm in the Human Heart: An Endocardial and Epicardial Mapping Study in Patients with a History of Atrial Fibrillation,” *J. Cardiovasc. Electrophysiol.*, vol. 18, no. 4, pp. 402–408, Apr. 2007.
- [124] L. Martinez-Mateu *et al.*, “Factors affecting basket catheter detection of real and phantom rotors in the atria: A computational study,” 2018.
- [125] D. U. J. Keller, F. M. Weber, G. Seemann, and O. Dössel, “Ranking the Influence of Tissue Conductivities on Forward-Calculated ECGs,” *IEEE Trans. Biomed. Eng.*, vol. 57, no. 7, pp. 1568–1576, Jul. 2010.
- [126] C. P. Bradley, A. J. Pullan, and P. J. Hunter, “Effects of Material Properties and Geometry on Electrocardiographic Forward Simulations,” *Ann. Biomed. Eng.*, vol. 28, no. 7, pp. 721–741, Jul. 2000.
- [127] D. Miklavčič, N. Pavšelj, and F. X. Hart, “Electric Properties of Tissues,” in *Wiley Encyclopedia of Biomedical Engineering*, Hoboken, NJ, USA: John Wiley & Sons, Inc., 2006.
- [128] S. Gabriel, R. W. Lau, and C. Gabriel, “The dielectric properties of biological tissues: III. Parametric models for the dielectric spectrum of tissues,” 1996.

-
- [129] R. N. Klepfer, C. R. Johnson, and R. S. Macleod, "The effects of inhomogeneities and anisotropies on electrocardiographic fields: a 3-D finite-element study," *IEEE Trans. Biomed. Eng.*, vol. 44, no. 8, pp. 706–719, 1997.
- [130] L. G. Tereshchenko and M. E. Josephson, "Frequency content and characteristics of ventricular conduction.," *J. Electrocardiol.*, vol. 48, no. 6, pp. 933–7, 2015.
- [131] M. Potse *et al.*, "P-wave complexity in normal subjects and computer models," *J. Electrocardiol.*, vol. 49, no. 4, pp. 545–553, Jul. 2016.
- [132] P. Kligfield and P. M. Okin, "Prevalence and Clinical Implications of Improper Filter Settings in Routine Electrocardiography," *Am. J. Cardiol.*, vol. 99, no. 5, pp. 711–713, Mar. 2007.
- [133] R. Alcaraz, A. Martínez, and J. J. Rieta, "The P Wave Time-Frequency Variability Reflects Atrial Conduction Defects before Paroxysmal Atrial Fibrillation," *Ann. Noninvasive Electrocardiol.*, vol. 20, no. 5, pp. 433–445, Sep. 2015.
- [134] T. Yamada, M. Fukunami, M. Ohmori, K. Kumagai, A. Sakai, and N. Kondoh, "Characteristics of Frequency Content of Atrial Signal-Averaged Electrocardiograms During Sinus Rhythm in Patients With Paroxysmal Atrial Fibrillation," 1992.
- [135] T. Lin *et al.*, "P-wave morphology and electrical activity of the isolated left atrial appendage on 12-lead ECG in patients with recurrent atrial tachyarrhythmias after pulmonary vein isolation," *J. Interv. Card. Electrophysiol.*, vol. 50, no. 2, pp. 169–178, Nov. 2017.
- [136] É. Irakoze and V. Jacquemet, "Simulated P wave morphology in the presence of endo-epicardial activation delay," *EP Eur.*, vol. 20, no. suppl_3, pp. iii16-iii25, Nov. 2018.
- [137] S. Pezzuto *et al.*, "Beat-to-beat P-wave morphological variability in patients with paroxysmal atrial fibrillation: an *in silico* study," *EP Eur.*, vol. 20, no. suppl_3, pp. iii26-iii35, Nov. 2018.
- [138] Y. Zheng, B. Georgescu, A. Barbu, M. Scheuering, and D. Comaniciu, "Four-chamber heart modeling and automatic segmentation for 3D cardiac CT volumes," *Med. Imaging 2008 Image Process.*, vol. 6914, p. 691416, 2008.
- [139] D. Kang, "Heart chambers and whole heart segmentation techniques: review," *J. Electron. Imaging*, vol. 21, no. 1, p. 010901, 2012.
- [140] D. Grosgeorge, C. Petitjean, J. Caudron, J. Fares, and J. N. Dacher, "Automatic cardiac ventricle segmentation in MR images: A validation study," *Int. J. Comput. Assist. Radiol. Surg.*, vol. 6, no. 5, pp. 573–581, 2011.
- [141] E. E. Özsavag, Z. Telatar, B. Dirican, Ö. Saler, and M. Beyzadeollu, "Automatic Segmentation of Anatomical Structures from CT Scans of Thorax for RTP," *Comput. Math. Methods Med.*, vol. 2014, pp. 1–15, 2014.
- [142] R. Beigel, N. C. Wunderlich, S. Y. Ho, R. Arsanjani, and R. J. Siegel, "The left atrial appendage: Anatomy, function, and noninvasive evaluation," *JACC Cardiovasc. Imaging*, vol. 7, no. 12, pp. 1251–1265, 2014.
- [143] D. Sánchez-Quintana, G. Pizarro, J. R. López-Mínguez, S. Y. Ho, and J. A. Cabrera, "Standardized Review of Atrial Anatomy for Cardiac Electrophysiologists," *J. Cardiovasc. Transl. Res.*, vol. 6, no. 2, pp. 124–144, Apr. 2013.
- [144] M. Varela *et al.*, "Novel MRI Technique Enables Non-Invasive Measurement of Atrial Wall Thickness," *IEEE Trans. Med. Imaging*, vol. 36, no. 8, pp. 1607–1614, Aug. 2017.

- [145] J. M. Hoermann, M. R. Pfaller, L. Avena, C. Bertoglio, and W. A. Wall, "Automatic mapping of atrial fiber orientations for patient-specific modeling of cardiac electromechanics using image registration," *Int. j. numer. method. biomed. eng.*, no. February, pp. 1–18, 2019.
- [146] C. H. Roney *et al.*, "Universal atrial coordinates applied to visualisation, registration and construction of patient specific meshes."
- [147] S. Zahid *et al.*, "Feasibility of using patient-specific models and the 'minimum cut' algorithm to predict optimal ablation targets for left atrial flutter," *Heart Rhythm*, vol. 13, no. 8, pp. 1687–1698, Aug. 2016.



UNIVERSITAT
POLITÈCNICA
DE VALÈNCIA



ESCUELA TÉCNICA
SUPERIOR INGENIEROS
INDUSTRIALES VALENCIA

BUDGET

BUDGET INDEX

1. Staff costs	155
2. Software costs	155
3. Hardware costs	166
4. Total cost of the project.....	166

BUDGET

1. STAFF COSTS

Position	Biomedical engineer
Nº of hours	500 h
Unitary cost	40 €/h
Imputable cost (without a patronal fee)	20,000 €
Patronal fee (37.45%)	7,490 €
Total imputable cost	27,490 €

Table 1. Staff costs

2. SOFTWARE COSTS

Program	License cost	Licence duration	Usage duration	Imputable cost (without IVA)	IVA (21%)	Total imputable cost
Matlab	2000 €	1 year	6 months	790 €	210 €	1,000 €
Seg3D	Free	-	-	-	-	-
Paraview	Free	-	-	-	-	-
Blender	Free	-	-	-	-	-
PuTTY	Free	-	-	-	-	-
WinSCP	Free	-	-	-	-	-
Elvira	Free	-	-	-	-	-
Total without IVA	790 €					
Total with IVA	1,000 €					

Table 2. Software costs

3. HARDWARE COSTS

Device	Device cost	Amortization time	Usage time	Imputable cost (without IVA)	IVA (21%)	Total imputable cost
Laptop	700 €	5 years	6 months	55 €	15 €	70 €
Cluster	20,000 €	5 years	6 months	1,580 €	420 €	2,000 €
Drawing tablet	80 €	6 months	6 months	63 €	17 €	80 €
Total without IVA	1,698 €					
Total with IVA	2,150 €					

Table 3. Hardware costs

4. TOTAL COST OF THE PROJECT

Summary of the budget (with patronal fee and IVA included)	
Staff costs	27,490 €
Software costs	1,000 €
Hardware costs	2,150 €
Total cost	30,640 €

Table 4. Total cost of the project